Cape Peninsula
University of Technology

Fabrication of a gold nanorod metal organic framework sensor for epidermal growth factor; a biomarker for kidney disease

By

Zvikomborero Takunda Gwanzura

(B TECH: Chemistry, CPUT)

Dissertation submitted in fulfilment of the requirements for the degree

Master of Applied Sciences: Chemistry

In the Faculty of Applied Sciences

At the Cape Peninsula University of Technology

Supervisor: Prof. Mangaka C. Matoetoe

Cape Town Campus

August 2018

DECLARATION

I, **Zvikomborero Takunda Gwanzura**, declare that the contents of this dissertation represent my own unaided work, and that the thesis has not previously been submitted for academic examination towards any qualification. Furthermore, it represents my own opinions and not necessarily those of the Cape Peninsula University of Technology.

Signed **Date**

ABSTRACT

Biosensors have been on the forefront to provide clinical diagnosis tools for various diseases. Proper selection of biomarkers as well as chemical electrode modification is key in the fabrication of electrochemical biosensors. Hence, electrode modified with nanomaterials devices to improve electroanalytical applications. These nanomaterials were functionalized to improve conductivity, accelerate signal transduction and amplify biorecognition events. Thus, resulting in novel sensing platforms that are highly sensitive and selective towards the target analyte.

In this study, gold nanorods (Au NRs) capped with CTAB, zeolitic imidazole framework were synthesised using the seed mediated and hydrothermal method respectively. Composites of gold nanorods with cysteine, ZIF-8 or both were also synthesised. All synthesised materials were characterized using ultraviolet–visible (UV-Vis) spectroscopy, Fourier transform infrared spectroscopy (FTIR), scanning electron microscopy (SEM), X-Ray diffraction (XRD) and cyclic voltammetry (CV) techniques. The obtained results confirmed the synthesis of the nanomaterials and composites. Identification of the ideal platform for fabrication of a transducer with the best electrochemical response was determined by studying the combinations of the synthesised nanomaterials and composites. The studied parameters were surface coverage, conductivity, rate of electron transfer constant. Cysteine-Au NRs composites platforms, had exceptional properties hence its synthesis optimisation of was undertaken. The effect of CTAB, reaction time, volume and concentration ratio of Au:Cysteine, temperature and pH on the composite properties were assessed. However, this composite's electrochemical properties decreased when bioconjugated with the antibodies. Hence, the choice of Au NRs CTAB functionalised ZIF-8 (CTABAu/ZIF-8) as the transducer for biosensor applications due to a more favourable biocompatibility. Biosensor fabrication was done by drop coating glassy carbon electrode with the CTABAu/ZIF-8 forming a transducer followed by immobilisation of the antibody (Ab) using a covalent attachment method with glutaraldehyde (GA) as a cross linker. The target analyte, epidermal growth factor (EGF) was interacted with the Ab binding sites via electrostatic forces. All the fabrication steps were optimized for biosensor components, immobilization technique (drop coating and immersion), concentration and incubation time of linker and bioreceptor, as well as the synthesis of the CTABAu-ZIF-8 composites where in situ and ex situ techniques were compared together with the effect of the concentration ratio of Au: ZIF-8. There was also an analysis of optimum pH. Optimum conditions were found to be immersion in 3 % GA and 2 µg/ml Ab, with incubation times of 8, 10 and 5 minutes for GA, Ab and EGF respectively at a

pH of 6. The following electroanalytical techniques: cyclic voltammetry (CV), differential pulse voltammetry (DPV) and square wave voltammetry (SWV) were utilised for EGF detection. The DPV showed better reproducibility, higher currents and better resolution hence; it was the method of choice. The technique's optimisation involved assessments of the effect of step potential, starting potential and pulse amplitude. The optimum response for pulse amplitude, step potential and starting potential were 60 mV, 20 mV and 0.5 V respectively. The biosensor analytical parameters were linear towards EGF in the concentration range from 2 to 100 nM with a detection limit of 0.58 nM. Reproducibility and repeatability tests were acceptable, and the biosensor had a stability over 80 % within 15 days. There was no interference observed in the presence of glucose and creatine. The EGF biosensor was successfully applied in urine and saliva analysis, obtaining 67.5 and 3.12 nM respectively. This biosensor's positive outcome strongly suggests its potential as a diagnosis tool for early detection of kidney disease as it was able to detect EGF concentration within physiological levels of EGF in normal kidney function.

ACKNOWLEDGEMENTS

First and foremost, I would like to thank the Almighty God, my dear Lord and Saviour Jesus Christ, for the wisdom, knowledge and understanding He has bestowed on me in the science field. My thanks to Prof. M.C. Matoetoe who supervised me in this project and ensured that I achieve my optimum potential and express it in my research.

To my parents, Ralph and Spikelele Gwanzura, I thank you for your words of motivation, encouragement and financial support. You made the work much easier and pleasant. To my friend, Miriam de Almeida, would like to thank you for all the support you offered throughout the times.

Also, my heartfelt appreciation to Cape Peninsula University of Technology and University of Western Cape for providing the platform and resources for this project to come to fruition.

God bless you all.

DEDICATION

This is dedicated to my family, the Gwanzura family. We have prevailed in all situations and challenges. This is another trophy for you.

TABLE OF CONTENTS

LIST OF FIGURES

LIST OF TABLES

GLOSSARY

Abbreviation/Acronym	Meaning
Ab	Antibody
AR	Amphiregulin
CKD	Chronic Kidney Disease
CTAB	Cetyltrimethyl-Ammonium Bromide
CV	Cyclic Voltammetry
Cys	Cysteine
DPV	Differential Pulse Voltammetry
EGF	Epidemic Growth Factor
FTIR	Fourier Transform Infrared Spectroscopy
GA	Glutaraldehyde
GCE	Glassy Carbon Electrode
LSPR	Local Surface Plasmon Resonance
MOF	Metal Organic Framework
NP	Nanoparticle
NR	Nanorod
PBS	Phosphate Buffered Saline
SEM	Scanning Electron Microscopy
SWV	Square Wave Voltammetry
TGF-α	Transforming Growth Factor Alpha
UV-Vis	Ultraviolet–Visible spectroscopy,
XRD	X-Ray Diffraction
ZIF	Zeolitic Imidazolate Framework

PREFACE

Thesis overview

This dissertation focuses on the synthesis of a zeolitic imidazolate framework encapsulated with gold nanorods. The study of this composites various platforms electrochemical properties. As well as the use of the best plat in fabrication of a biosensors for analysis of EGF; a kidney disease biomarker. The primary goal was to develop an efficient biosensor, which can be exploited to improve its sensitivity, selectivity and reliability. The outlines of the dissertation chapters are reported herein.

- **Chapter one** covers the background of this research and explains more on the research problem statement, addressing the challenges faced in early identification of kidney disease. The aims and objectives related to the problem are also stated.
- **Chapter two** entails the literature review, which introduces the theoretical background of various biosensors being used and biomarkers of kidney disease including EGF protein. A detailed look at metal organic frameworks and nanoparticles and their applications in biosensor development is also highlighted.
- **Chapter three** involves the synthesis and characterization of the materials and composites utilized in the biosensor fabrication. The techniques, methods and instruments used are also highlighted. Optimization of the cysteine-gold composite was also analysed.
- **Chapter four** focuses on fabrication of the transducer and its electrochemical characterization. Optimization of biosensor fabrication was investigated by looking at various parameters.
- **Chapter five** involves the detection of EGF using the modified electrode and the application of the biosensor in real samples. Studies of the sensitivity and stability of the developed biosensor, together with recovery studies are also highlighted.
- **Chapter six** summarizes the main conclusions and recommendations of this study

CHAPTER ONE

INTRODUCTION

1.1 Statement of research problem

There has been a great clinical need to identify patients most likely to get end stage kidney disease (Rachel, 2010). The main method used to detect kidney disease is kidney biopsy that requires a small kidney tissue sample. The process is expensive, invasive with possible health risks since it has limitations in determining the progression of kidney disease. One of the early indications of wearying kidney function is when the concentration of epidermal growth factor protein begins to decrease in urine or saliva (Ju and Nair, 2015). This protein will be used as a biomarker with a biosensor fabricated from gold nanoparticles incorporated with ZIF-8 conjugated with a specific antibody for EGF detection.

1.2 Background

Biosensors consist of a biological recognition molecule immobilized onto the surface of a signal transducer (Betz et al., 2016). In comparison with other methods, there are more benefits in using biosensors, like fast analysis and time of response, little reagents for calibration, possibility of analysing non-polar molecules and high specificity. Presently they are being extensively utilised for molecular detection of biomarkers related to early diagnosis of cardiovascular, neurodegenerative, cancer and kidney disease (Fitzgerald & Fenniri, 2017). The usual route for early detection is the use of biomarkers. According to the World Health Organisation (WHO), any analyte that shows a link between a biological process and a possible hazard whether physical, chemical or biological is termed a biomarker (Strimbu and Tavel, 2010). The analysed signal can be biochemical, an interaction at a molecular level or physiological. There is a critical role played by biomarkers in comprehending the relationship between biological processes that are quantifiable and clinical results. This is important in reducing the exposure to ineffective experimental treatments (Kok et al., 2014).

Currently, early detection of chronic kidney disease (CKD) is based on assessment of an escalation in urinary albumin excretion or a decline in the estimated glomerular filtration rate (eGFR). Despite the proven clinical importance of these markers, albuminuria in some patients is not predictive of the development of CKD and does not accompany a significant reduction in the eGFR (Ju et al., 2015). Therefore, there is a need to find a biomarker that

can predict the risk of renal failure for the sake of optimizing individual therapeutic interventions to slow disease progression. Late disease detection might lead to end stage kidney disease where an affected individual's kidneys can no longer meet their body's need to remove waste. Progression to kidney failure or other adverse outcomes prevention or delayed through early detection and treatment of CKD is a necessity.

Human epidermal growth factor (hEGF) is present in urine at about 60-80 ng/ml in people with normal kidney function (Chou et al., 1997). People with early-stage chronic kidney disease are likely not to notice any symptoms. Understanding which patients are at risk of severe chronic kidney disease can lead to earlier and more effective treatments, therefore preserving kidney function and helping patients lead longer and healthier lives (Ju and Nair, 2015). A decrease in epidermal growth factor levels in urine is linked to worsening kidney disease (Safirstein et al., 1989). In fact, patients with low urinary epidermal growth factor are four times more likely to worsen than those who retain epidermal growth factor function in their kidneys. This protein (EGF), can indicate whether the patient is at risk of end stage kidney disease or not (Tsau & Chen, 1999). The EGF proteins are involved in several mechanisms such as normal cell growth and differentiation. Their effects are mediated via autocrine, paracrine, or endocrine mechanisms. The EGF-family growth factors are involved in regulation of various epithelial ion channels in the kidney. For instance, EGF stimulates store-operated Ca^{2+} channels in human mesangial cells through an intracellular signalling mechanism involving tyrosine kinase. In addition, EGF induces constriction of both preglomerular and postglomerular arterioles, resulting in acute major reductions in the rates of glomerular filtration and perfusion (Staruschenko et al., 2013). While glomerular lesions can be reversible, tubular injury is closely associated with progression of nephropathies. Therefore, it is more appropriate to use tubular proteins such as EGF as better predictive biomarkers than proteinuria and albuminuria. Epidermal growth factor receptor (EGFR) is expressed throughout the kidney epithelium and interstitium (Klein et al., 2016). Epidermal growth factor has the highest affinity for EGFR. Activation of the receptor by the EGF protein is critical to inhibit the progression of chronic kidney disease. During kidney disease, a shift in either ligand or receptor availability might occur. This shift can tilt the physiological balance and lead to kidney disease. The role of the EGF–EGFR signalling axis in kidney disease depends on a variety of factors such as aetiology and disease stage (Tang et al., 2013). Since EGF is excreted in the urine, it might prove valuable as a prognostic biomarker as EGF production is inversely correlated with disease severity.

A metal organic framework (MOF) is a new class of hybrid material built from metal ions with well-defined coordination geometry and organic bridging ligands (Faolcaro 2014). For the synthesis of MOFs, some common metal ions such as Zn^{2+}, Al^{3+} and Ln^{3+} can be used, as they offer a flexible coordination environment with different geometries (Stock, 2011). The properties of MOFs include ultrahigh porosity, large internal surface area, wide range of thermal and chemical stability, selectivity, feasibility of building a designed crystal structure, exceptionally large specific surface area and non-toxic nature (Qiu and Xue, 2014). The metal organic framework used in this research is zeolitic imidazolate framework (ZIF-8) which belongs to the ZIF family (Shilun, 2014). This framework represents a unique class of MOFs in which the network topology and related properties vary greatly while core chemical connectivity is retained (Zhou, 2014). They have excellent chemical and thermal stability, which makes them good candidates for biosensing (Lee, 2013).

Gold nanoparticles (Au NPs) have been studied for their unique optical features. Due to surface plasmon resonance phenomenon, gold nanoparticles can respond to the refractive index change of the environment near the particles (Bridges et al., 2013). This phenomenon gives gold nanoparticles the potential to be used as biosensors that detect the biological interactions at or near the particles. The physical properties of gold nanoparticles can be exploited for biosensing in many ways (Caihol, 2011). Primarily, with proper conjugated aptamers, gold nanoparticles can aggregate or disaggregate under certain conditions. This will change their absorbance so dramatically that it is observable to naked eyes. The second way is that the localized surface plasmon resonance peak can shift as a response to the analyte behavior, such as protein binding or a deposition of a layer on the nanoparticle (Brust et al., 1994). Antibodies are tethered to gold nanoparticle surfaces using PEG linkers or glutaraldehyde. These linkers provide an easy method of self-assembly of antibodies onto the gold surface since the bonds created by linkers is much stronger than the electrostatic forces that drive protein-gold chemisorption. In addition, they help to lift the antibody from the surface, permitting better conformational freedom of the molecule and therefore improving antibody binding.

1.3 Aim

To fabricate a functionalised MOF of zeolitic imidazolate-Au hybrid conjugated with a specific antibody biosensor for the detection of epidermal growth factor a kidney disease biomarker.

1.4 Objectives

1. To synthesize and functionalise MOF (zeolitic imidazolate and its Au hybrid).
2. Spectroscopic and electrochemical characterization of ZIF-8 and its Au hybrid.
3. Fabrication of the transducer using ZIF-8 encapsulated with Au NRs.
4. Immobilization of the antibody.
5. Fabrication and application of the EGF biosensor.
6. Optimisation of the fabrication of the biosensor.
7. Validation of the fabricated biosensor for the detection of EGF, through interference, reproducibility, stability and recovery studies.

1.5 References

Abbara A, Davidson R. 2011. Etiology and management of genitourinary tuberculosis. *Nat Rev Urol,* 8:678.

Baserga, R. 1981. Tissue growth factors. 2nd ed, USA, pp 82-95.

Betz, B.B., Jenks, S.J., Cronshaw, A.D., Lamont, D.J., Cairns, C., Manning, J.R., Goddard, J., Webb, D.J., Mullins, J.J., Hughes, J., Mclachlan, S., Strachan, M.W.J., Price, J.F. & Conway, B.R. 2016. Urinary peptidomics in a rodent model of diabetic nephropathy highlights epidermal growth factor as a biomarker for renal deterioration in patients with type 2 diabetes. *Kidney International*, 89(5): 1125–1135.

Bohunicky, B. 2011. Biosensors: the new wave in cancer diagnosis. *Nanotechnol Sci Appl,* 4:1–10.

Bridges, C., Dicarmine, P.M., Fokina, A. 2013. Synthesis of gold nanotubes with variable wall thickness. *J. Mater. Chem. A*, 1: 1127-1133.

Brust, M., Walker, M., Bethell, W. 1994. Synthesis of thiol-derivatised gold nanoparticles in a two phase liquid system*. J. Chem. Soc*., 801-802.

Caihol, J. 2011. Prevalence of chronic kidney disease among people living with HIV/AIDS in Burundi. *BMC Nephrol*, 12: 40.

Castro, L., Blazquez, M. 2011. Biosynthesis of gold nanowires using sugar beet pulp. *Process Biochem*., 46 (5): 1076−1082.

Chou, J. S., Reiser, I. W., Porush, J. C. 1997. Aging and urinary excretion of epidermal growth factor. *Annals of Clinical and Laboratory Science* 27(2): 116-122.

Faolcaro, P. 2014. MOF positioning technology and device fabrication. *Chem. Soc. Rev,* 43 (16): 5403-6176.

Gambelunghe, A, Sallsten, G. 2016. Low-level exposure to lead, blood pressure and hypertension in a population based cohort. *Environmental Research*, 149:157–163

Giacoman, S. 2015. Biomarkers in chronic kidney disease, from kidney function to kidney damage. *World J Nephrol*, 4(1): 57–73.

Go A, Chertow G, Fan D, et al. 2004. Chronic kidney disease and the risks of death, cardiovascular events, and hospitalization. *N Engl J,* 351:1296-1305.

Hemmelgarn, B, Manns B, Lloyd A, et al. 2010. Relation between kidney function, proteinuria, and adverse outcomes. *JAMA,* 303:423-429.

Fitzgerald, J. & Fenniri, H. 2017. Cutting Edge Methods for Non-Invasive Disease Diagnosis Using E-Tongue and E-Nose Devices. *Biosensors*, *7*(4): 59.

Jha, V, Garcia, G. 2013. Chronic kidney disease: global dimension and perspectives. *Lancet*, 13:260-272.

Johnston, J. 2010. Screening renal failure patients for tuberculosis. *BMC Nephrol,* 52 (9): 413.

Ju, W, Nair, V, Smith, S. 2015. Tissue transcriptome-driven identification of epidermal growth as a kidney disease biomarker, Science Translational Medicine, 7 (16): 316-324.

Klein, J., Bascands, J.L., Buffin-Meyer, B. & Schanstra, J.P. 2016. Epidermal growth factor and kidney disease: A long-lasting story. *Kidney International*, 89(5): 985–987.

Kok, H.M., Falke, L.L., Goldschmeding, R. & Nguyen, T.Q. 2014. Targeting CTGF, EGF and PDGF pathways to prevent progression of kidney disease. *Nature Reviews Nephrology*, 10(12): 700–711.

Lee, Y. 2013. Synthesis of metal-organic frameworks, *Journal of Chemical Engineering*, 30 (9): 1667-1680.

Qiu, S, Xue, M. 2014. Metal–organic framework membranes: from synthesis to separation application*, Journal of Chemical Society*, 43: 6116-6140.

Rachel, C. 2010.Metal-Organic Frameworks as Potential Drug Carriers. *Chemical Biology,* 14(2): 262–268.

Rosenthal S, Wright, D. Nanobiotechnology protocols vol 2P 107 Humana Press, New Jersey, USA. 2005.

Safirstein, R., Zelent, A.,Price, M. 1989. Reduced renal prepro-epidermal growth factor mRNA and decreased EGF excretion in ARF. *Kidney International.*, 36: 810-815.

Shilun, Q. 2014. Metal–organic framework membranes: from synthesis to separation application. *Chem. Soc. Rev,* 43: 6116-6140.

Staruschenko, A., Palygin, O., Ilatovskaya, D. V. & Pavlov, T.S. 2013. Epidermal growth factors in the kidney and relationship to hypertension. *AJP: Renal Physiology*, 305(1): 12–20.

Stock, N. 2011. Synthesis of Metal-Organic Frameworks (MOFs). *American Chemical Society,* 112:933-969.

Strimbu, K., Tavel, J. A. 2010. What are Biomarkers? Current Opinion in HIV and AIDS, 5 (6): 463–466.

Volberding, P. 2008. Global HIV/AIDS medicine, 2ND ed, CHINA, pp 299.
Zhang, Q. 2008. Prevalence of chronic kidney disease in population-based studies. *BMC Public Health*, 28: 117.

Zhou, H. 2014. Metal–Organic Frameworks. *Chem. Soc. Rev*, 43:5415-5418.

CHAPTER TWO

LITERATURE REVIEW

2.1 Introduction

Biosensors have been positively used in various ways for the improvement in quality of life. Immense global research attention has been directed to biosensor applications in disease diagnostics. Their benefits are a reduced cost, real time detection, quick response, high selectivity and sensitivity, possibility of miniaturization, portability and less reliance on external laboratories (Thevenot et al., 1999). Some of the diseases that have utilised biosensors in their detection are breast cancer, renal diseases, celiac disease and hepatitis B virus (Huang et al., 2017). Even though the growth rate of the biosensor market is increasing, it is still to reach its prime by extending to the wide percentage of people affected by these diseases. Particularly in Sub Saharan Africa where there are limited resources and high cases of HIV related diseases (Fogel & Limson, 2016). The usual macroscopic imaging diagnostic techniques like positron emission tomography (PET), mammography and colonoscopy have enhanced detection of diseases. Nevertheless, their sensitivity to detect diseases at an early stage and managing the patient's therapy response is not satisfactory. Biomarker usage in early detection of diseases is developing as one of medicine's most ingenious strategy (Li et al., 2010). These biomarkers are found in biological fluids like blood, saliva and urine, where small variations in biomarker concentrations or compositions can reveal the patient's physiological stage. Patient survival rates can increase to more than 90 % and an eightfold reduction in healthcare charges can be realised with an early detection and accurate diagnosis of diseases (Hartwell et al., 2006). This reduces the patient's hospital time and improves their welfare as the disease as a result of the timely treatement when it is highly receptive to contemporary therapies (Price, 2001).

2.2 Epidermal growth factor

Epidermal growth factor is a solitary chain polypeptide that shows stimulating growth behaviour both in vitro and in vivo on different epidermal and epithelial tissues. The isoelectric point of EGF protein is pH 4.6 (Campbell et al., 1990). Human EGF is known to

be similar to human urogastrone, which is made by the human duodenum. It is widely used in clinical and cosmetic fields. As shown in Figure 2.1, the polypeptide has 53 residues with a molecular weight of approximately 6400 (Carpenter et al., 1975). The acidic peptide has six half-cystines, which occur in disulfide linkages. The COOH-terminal portion of the molecule exhibits four arginine residues (Freedman et al., 1996).

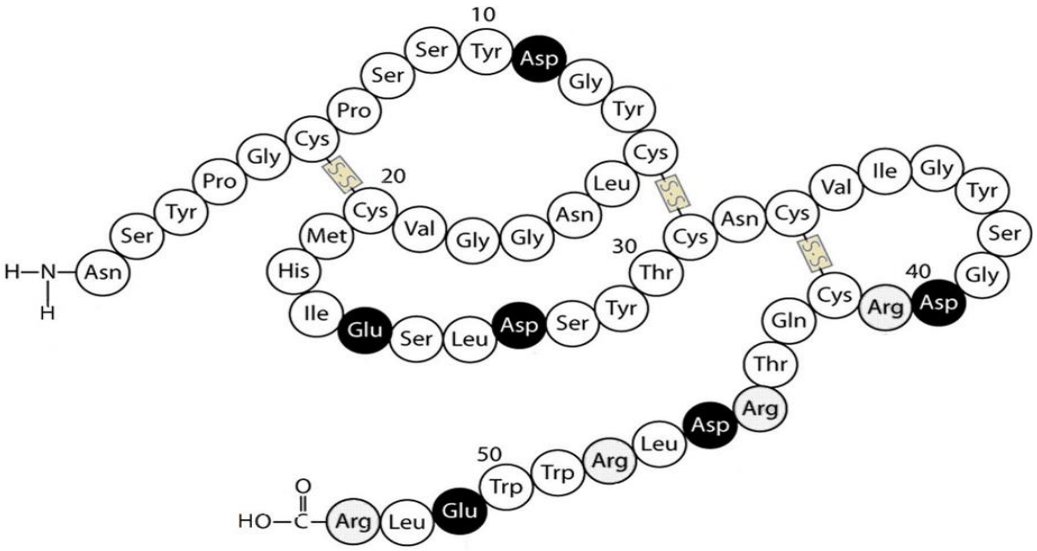

Figure 2.1: Structure of EGF with the 53 amino residues

2.3 EGF as a potential biomarker for kidney disease

Present studies indicate that the kidney is an important site of EGF synthesis, going beyond most other tissues in the human species. Epidermal growth factor is part of a class of growth factors called the EGF Family (Authier et al., 1999). The EGF family are notable for their capacity to invigorate cell development and multiplication. They are key to various developmental processes including differentiation of epithelial cells and mitogenesis stimulation. Some of the members of the EGF family are betacellulin, heparin-binding EGF (HB-EGF), transforming growth factor-alpha (TGF-α) and amphiregulin (AR). A sequence similarity is shared between all these molecules. A minimum of 28 % sequence similarity and 100 % conservation of the six cysteine residues occur within the mature sequence of EGF (Huang et al., 2010). The EGF family members and their receptors act as biomarkers for various diseases. These biomarkers are mainly used in cancer diagnosis (Jazayeri et al., 2016, Uchiyama et al., 2014). Comparing all the EGF family members, epidermal growth factor is specific to the kidney and is produced in response to gastrointestinal tract injury.

The TGF-α has been associated with embryonic advancement and it has minimal expression in normal adult kidney. Other family members are expressed at small concentrations in the kidneys (Carpenter et al., 1975). Great levels of EGF can be identified in urine and concentrations of up to 80 nM have been detected. The messenger ribonucleic acid (mRNA) for EGF can similarly be recognized in the collecting duct and particularly in the intercalated cells of this nephron portion, where EGF is limited to its basolateral surface.

Numerous diabetic patients experience the ill effects of declining renal capacity without creating albuminuria. The EGF protein can be an alternative biomarker because reduced renal levels and urinary discharge of EGF has been seen in different human kidney illnesses. Some of these diseases are lupus nephritis, diabetic nephropathy, acute kidney injury and IgA nephropathy. Also, it upgrades renal tubule cell recovery and repair and quickens the recuperation of renal capacity after damage (Zheleznova et al., 2011). In addition, urinary EGF excretion corresponds to modified intrarenal EGF articulation. The biomarker also decreases early in the development of renin-dependent hypertension and it has been found to predict the CKD progression assessed by the eGFR slope (Isaka, 2016). These outcomes point to the fact that EGF can mirror the pathological changes, which occur in many kidney ailments and address an alternate pathophysiologic component than that identified by albuminuria. The quantification of EGF is mainly done using the enzyme-linked immunosorbent assay (ELISA) and Radioimmunoassay (RIA) methods (Zeng & Harris, 2014). The main drawbacks for these techniques is that they are expensive and time consuming. Hence, this study aims to fabricate an electrochemical EGF biosensor which can be used as a point of care clinical tool.

2.4 Biosensors

A biosensor is an autonomously coordinated receptor transducer device, which is fit for giving specific quantitative or semi-quantitative systematic data by utilizing a biological recognition element. Biosensors started in the 1960s by the pioneers Clark and Lyons. One of the advantages of biosensors is their high sensitivity. This comes about from the high affinity of biomolecules toward their targets, for instance, antibodies catch antigens at a very low dissociation constant and DNA-DNA binding is considerably greater than antigen-antibody (Li et al., 2010). Another advantage is the high selectivity exhibited by biological elements. An illustration is that enzyme and substrate show analogous behavior to lock and key. Selective biosensors are often developed due to this high selectivity. Due to the improvement of the current electronic industry, it has been moderately simple to create

cheaper and integrated biosensor devices. The ability to detect pathogens or to undertake genetic studies is enhanced by biological sensors. Even of more significance is their utilization in point of care investigations and especially in small clinics (Thevenot et al., 1999).

2.4.1 Types of biosensors

Most biosensors that are utilized are piezoelectric, DNA biosensors, immunosensors, enzyme-based and tissue-based biosensors. The earliest biosensors amongst others are enzyme-based biosensors. Enzymes possess capacity to precisely identify their substrates and to offer catalytic conversion (Crespilho, 2013). These distinctive attributes make the enzymes potent tools to make analytical devices. Updike and Hicks developed the first enzyme-based sensor in 1967. They were developed on immobilization methods which utilize covalent bonding, ionic bonding and Van der Waals forces adsorption of enzymes. The regularly used enzymes for this function are oxidoreductases, peroxidases and aminooxidases (Fartas et al., 2017). Immunosensors make use of antibodies and they are the doorway to immune-diagnosis. They were developed on the principle of the high affinity of antibodies towards their antigens. Living cells are the biorecognition element in cell-based sensors and these sensors rely on the capability of living cells to recognize the intracellular and extracellular microenvironment condition (Akyilmaz et al., 2010). Nucleic acid molecules are the biorecogniton elements in DNA biosensors. They can identify and attach to their corresponding strand in a sample. The association comes about from the development of steady hydrogen bonds between the two nucleic acid strands. When it comes to optical biosensors, light is the output transduced signal that is measured. Fabrication of the biosensor can be by electrochemiluminescence or optical diffraction methods. They link the mass or concentration variations to the direct changes in light features. Biosensors that are piezoelectric, have a transducer made of quartz material where the biosensing component on the transducer vibrates at the normal frequency (Rau, 2005). This frequency is regulated by the external electrical signal, which creates a specific amount of current. At the point when the target analyte is open to the detecting material the response will cause the frequency to move, which will create changes in current measurements that can be compared to the mass of the target analyte. Gold NP based sensors use unique properties of gold nanoparticles in correlating the signal transduction with biological recognition occurrences and in modelling biosensing tools that show novel features (Wang et al., 2016).

2.4.2 Biosensor components

The three fundamental components that a biosensor comprise of are a bioreceptor, transducer and a signal relaying system (Figure 2.2). A bioreceptor comprises of an immobilized biocomponent that can identify the target analyte while the transducer functions as a converter (Cammann, 1977). A chemical change is brought about by the response between the analyte and bioreceptor like heat release, generation of a new chemical, electron flow and mass and pH changes. The transducer changes the biochemical signal into an electrical signal. A quantifiable signal is formed, like a digital output or a hard copy (Vidotti et al., 2011).

Figure 2.2 shows the components of a biosensor. Bioreceptors can be divided into three different groups. These are biocatalytic, bioaffinity and microbial based systems. The biocatalytic group makes use of enzymes to moderate a biochemical reaction. Bioaffinity-based biosensors depend on the use of proteins or DNA to recognize and bind to a specific target (Rogers, 2000). The microbial group utilizes microorganisms as the biological recognition element.

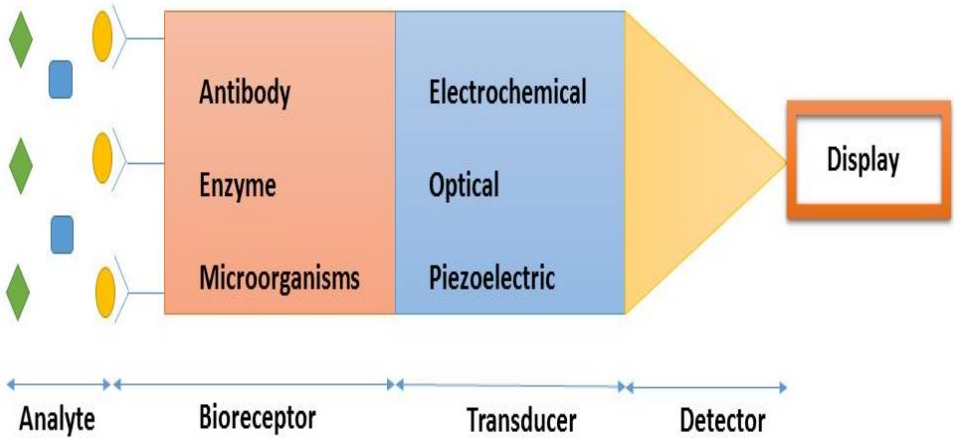

Figure 2.2: Basic components of a biosensor

The principle involves the determination of microbial inhibition or respiration using the target analyte. The type of bioreceptor used in this study was a bioaffinity-based group. This group has been the fastest growing area in biosensors research (Thevenot et al., 2001). The type

of antibodies that can be used can be either monoclonal or polyclonal antibodies. Polyclonal antibodies are made using various immune cells and bind different epitopes on a similar protein whereas antibodies which are monoclonal bind only on a singular epitope. Antibodies of the IgG class are the same in structure, on the other hand, their affinities for antigens may change generally. These distinctions in the binding affinity and specificity of antigens come from the changes in the sequence of amino acids at the binding site of the antigen. The location of the binding sites of the antibody are at the closures of the "Y-structured protein." The base of the "Y" referred to as the Fc unit contains the base of the structure and it is more regular as it possesses species-specific shape, that is mainly utilized as an antigen for making species-specific (anti-IgG) antibodies. The changes in antibody–antigen binding behaviours impact the various detection limits seen for antibody-based biosensors.

The other component of a biosensor is a transducer. Different types of transducers convert the biochemical signal in different ways. Electrochemical transducers produce changes in form of electrical signal that is directly proportional to the concentration of analyte. Optical transducers convert chemical energy into light energy (Mehrotra, 2016). They utilize changes in optical properties such as phase, amplitude and frequency. Piezoelectric transducers have crystals with no centre of symmetry and they produce an electrical signal when stressed mechanically. Classification of the types of biosensors can be by the type of signal transduction or the type of biological signaling tool they use (Lippincott-Schwartz et al, 2003).

2.4.3 Biosensor Applications

Various fields in the medical, food and marine industry have applied biosensors in their processes. This is because they offer improved sensitivity and stability in comparison to the old-fashioned methods. The applications of biosensors are shown in Figure 2.3. In food manufacturing, there is great need of quality, safety and conservation of food products. Conventional methods carrying out chemical testing and spectroscopy are expensive and time consuming. Biosensors are used for the detection of pathogens in food. A bioindicator of faecal contamination in food is the presence of Escherichia coli in vegetables. The bacteria can be measured by detecting changes in pH caused by ammonia using potentiometric biosensing techniques (Mehrotra, 2016).

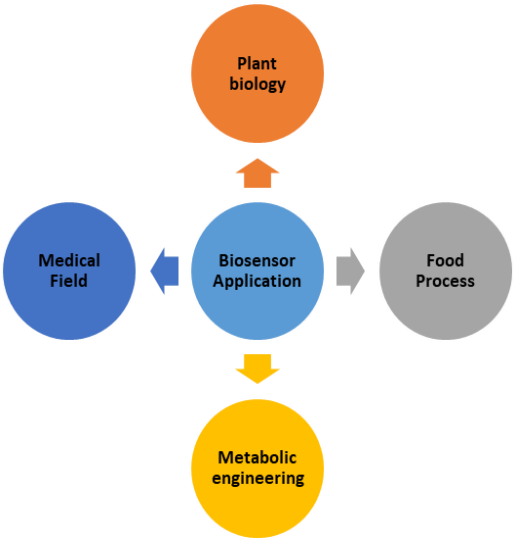

Figure 2.3: Applications of biosensors in various fields

A transition from the conventional techniques of mass spectroscopy for measuring ions and evaluating into cellular localization to biosensor applications has occurred. Biosensors provide ease of access when it comes to information. Metabolic engineers now produce a large amount of fuels, chemicals and from renewable feedstocks by taking advantage of microorganisms instead of depending on petroleum extracting plants (Venugopa, 2002). In vivo checking of cellular metabolism are being utilized by genetically encoded biosensors. The medical field has seen extensive growth in the applications of new biosensors. Nevertheless, the most dominant are glucose biosensors and pregnancy test biosensors. Glucose biosensors are applied in clinics for diabetes mellitus diagnosis, this needs accurate monitoring of blood-glucose levels. Household usage of blood-glucose biosensors contributes to 85% of the global market (Scognamiglio et al., 2014; Leatherbarrow et al., 1999). The introduction of nanoparticles has contributed immensely in biosensor transducer fabrication.

2.5 Metal nanoparticles

The freedom of electrons in matter greatly influence the physical and chemical properties. The electronic movement, thusly, is subject to the sort of material and the space open to its electrons which is the level of confinement (Wang, 2016). When the electrons are defined to the nanometer scale the spatial effects is much more felt. Consequently, when materials are in the range of 1–100 nm, novel features arise. These mesoscopic dimensions are limited in

their electronic motion as this is mainly based on the material shape. If the semiconductor size of the nanocrystals gets to the range of 2–10 nm, the movement of their charge carriers undergo quantum confinement. As a result, distinct fluorescence and absorption properties that rely on the shape and particle size emerge. Metallic materials need more attention to their surface effects especially when the particle size becomes similar to the electron mean free path. This commonly governs the response, yielding features varying from the bulk (Amendola et al., 2014).

2.5.1 Gold nanoparticles

Among the nanoparticles utilized as biosensor components, gold nanoparticles have gotten most noteworthy interests since they have a few sorts of fascinating properties. Those in the range of 1-100 nm, possess high surface to volume ratio to give a steady immobilization of a lot of biomolecules maintaining their bioactivity. In addition, Au NPs have a capacity to allow quick and direct electron exchange between an extensive variety of electroactive species and electrode components. The light disseminating properties and a great degree of improvement of the local electromagnetic field empowers Au NPs to be utilized as signal amplification labels in various biosensors (Wang et al., 2016). There are a few optical detecting methods for Au NPs and the surface plasmon resonance (SPR) has pulled in extensive research. Surface plasmon resonance is an optical occurrence emerging from the association between an electromagnetic wave and the conduction electrons in a metal. It is utilized for testing and determining physicochemical changes of thin films on metal surface. The plasmon resonance is triggered by the electromagnetic radiation producing an oscillation of the surface conduction electrons that is coherent (Rau, 2005). A change in the dielectric constant is propagated by the attachment of target molecules onto the metallic films. This results in the reflection of laser light from a metal-liquid surface to change (Vidotti et al., 2011).

2.5.2 Morphologies of Au NPs

Apart from sizes, gold nanoparticles also exhibit various shapes such as spherical, nanocages, nanoshells and nanorods as shown in Figure 2.4.

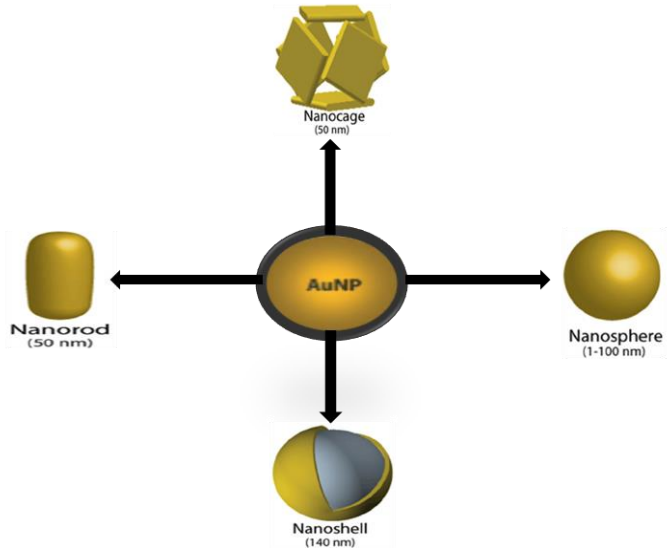

Figure 2.4: Different types of gold nanoparticles commonly used

Synthesis of Au NPs can be done by monitoring the reduction of an aqueous $HAuCl_4$ solution at different conditions and reducing agents. Normally, gold nanospheres show one absorption peak between 510-550 nm (Hiramatsu et al., 2004; Esumi et al., 1998). As the size of the particles increases, there is a shift of the absorption peak to longer wavelengths and there is a correlation between the size distribution range and the width of the absorption spectra (Leff et al., 1996; Weare et al., 2000). Gold NPs can also appear in the form of nanoshells. They are spherical in shape with dimensions of 10-200 nm (Frangioni, 2003; Fricker, 1996). Nanoshells comprise of a dielectric core enclosed by a small gold shell. Since they are unique NPs, they have outstanding chemical, optical and physical features. This makes them perfect materials for improving detection of cancer, treatment of malignancy and medical biosensing (Oldenburg et al., 1998). As an immediate phenomenon of nanoscale resonance, they exhibit great optical absorption, which makes them ideal candidates as contrast agents for imaging (Suzuki, 2005). Their ability to tune facilitates the absorption or scattering of light at specific. They possess an inert gold surface that offers various benefits like noncytotoxicity, biocompatibility and enabling of monoclonal antibodies' conjugation (Radloff, 2005; Caruso, 2001). Nanocage shaped Au consist of a new breed of NPs having hollow interiors and walls that are porous (Chen, 2007). Their synthesis involves a facile method of galvanic replacement reaction. This happens between solutions comprising of metal precursor salts and silver NPs (Chen et al., 2006). In addition, they are utilized in drug delivery systems and monitored drug release where they act as carriers (Chen, 2005; Chen et al., 2007). Gold nanorods (Au NRs) have a cylindrical shape with sizes that range between 1-40 nm in width and the length can span up to hundreds of nanometers. These nanorods are usually determined by their aspect ratio which is the length

divided by the width. Direct chemical synthesis is one way to produce Au NRs. A mixture of ligands allows the shape to be controlled and bond to diverse facets of the nanorod with various strengths (Martin, 1994). This permits various faces of the NR to develop at several rates, creating a lengthened object. In this study Au nanorods were chosen as the type of nanoparticles mainly because they have two plasmonic bands as shown in Figure 2.5 and the stronger longitudinal SPR band makes Au NRs more sensitive to variations in shape, size nano-environment and interparticle distance (Van der Zande et al.,1997).

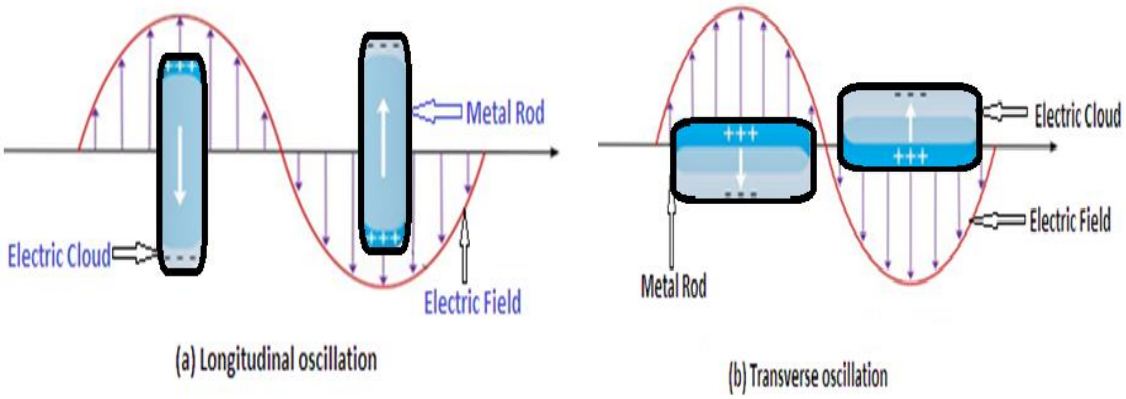

Figure 2.5: Schematic illustration of LSPR excitation for Au NRs

Figure 2.5 shows the local surface plasmon resonance (LSPR) excitation of Au NRs. There is evidence of two absorption bands in its absorbance spectrum. These are the transverse plasmon band (TPB) and the longitudinal plasmon band (LPB), consistent with the electron oscillation along the short and long axes of the Au NRs respectively (Yu, 1997). The short axes of Au NRs are usually insensitive to the variations in the size of the Au NRs and the neighboring refractive index, while the long axes display a red-shift as the Au NRs aspect ratio is increased there is high sensitivity to refractive index changes (Reetz, 1994). The LSPR features depend mainly on the shape, environment of the encompassing medium, refractive index changes and dielectric characteristics of the Au NRs. The electron charge density is affected by these factors on the surface of the particle. In many sensor structures, the indication of the LSPR sensor signal is observed in the variations of the wavelength or absorbance peak in the absorption spectrum of Au NRs.

2.5.3 Optical properties of Au nanoparticles

The fascination of Au NPs since old times, as shown in their deep colour, starts from the essential photophysical reaction that does not exist to non-metallic particles. At the point when a metal molecule is reacted with light, the wavering electromagnetic field of the light instigates oscillation of conduction band electrons in a coherent manner (Garcia et al., 1999; Kim et al., 2002). A charge separation is caused by the electron oscillation around the surface of the particle surface with regards to the ionic lattice. A dipole oscillation is formed in the same direction as the light's electric field. The maximum amplitude of the oscillation is reached at a certain frequency, which is the SPR. Strong absorption bands of the incident light are induced by the SPR and a UV–Vis absorption spectrometer can carry out the measurements. Plasmonic nanoparticles like silver and gold normally show a stronger SPR band compared to other metals. The wavelength and intensity of the SPR band relies on the aspects disturbing the electron charge density on the surface of the particle (Chang et al., 1999).

Conduction band electrons of nanoscale metals have room to oscillate when excited by incident radiation. Nevertheless, there is restriction of the oscillation distance by the NP size. Nanoparticles show some optical properties that are intriguing. Some of the features comprise of improved Rayleigh scattering, intense plasmon absorption and localized electromagnetic field at the NP surface. When the particle size is increased, a red shift of the SPR wavelength and an increase in the intensity occurs (Manna et al., 2001). For mesoscopic particles, there is more occurrence of band broadening because of the strong contributions from electron oscillations of a higher order. The surface plasmon resonance in Au NPs is so intense to the extent that it improves the light electric field locally by high orders of magnitude. In fact, the cross-section of the absorption connected with the surface plasmon resonance excitation is normally one thousand times larger than its geometrical section (Scott et al., 2005). These properties, including the simple modular functionality and great biocompatibility make Au NPs very conspicuous materials for biomedical applications. One of the drawbacks of using Au NPs in biomedicine is the SPR absorption band matching that of the haemoglobin one. This provides an enormous job to optically detect Au NPs in bloodstream. This restraint can be avoided by synthesising non-spherical Au NPs like NRs, where the SPR band separates into two. Therefore, modifying the aspect ratio of the NRs allows a shift of the perpendicular SPR to greater wavelengths of the spectrum where the biological tissues and blood scarcely absorbs. When looking at an ensemble of Au NRs, the LPB shows a red shift centered on the distance between the Au NRs and the ensemble size

and shape. Gold nanospheres are highly sensitive to local refractive index changes. This alteration is seen in the absorbance. Hence, the occurrence of bacteria, chemicals, viruses and cells can be simply and precisely detected by spotting the variations of the UV-Vis spectra. On the other hand, Au nanorods are sensitive to the shape, size and the refractive index. Once Au NRs are ensembled, they display the plasmon coupling phenomenon (Kim et al., 2002). In the case of a formation of a chain-like shape of Au NRs, a red shift in the LPB band is detected. The strength of the effect is proportional to the number of nanorods in the ensemble. As a result, these factors contributed in selecting Au NRs for use in biosensor fabrication.

2.5.4 Surface functionalization of gold nanoparticles

There are three essential strategies to promote functional groups to the surface of Au NPs. The common one is direct synthesis, this is centred on presenting the entire functional ligand in a single phase. There is a reaction between the bifunctional organic component and the gold nanoparticle by binding to the surface at least one of its functional groups. This generates a Au NP enclosed with compact shielding ligand layers with a functionality that is favourable (Manna et al, 2001). The ligand exchange technique is the second method that can be used. Here, the primary ligands are substituted by another ligand with preferred functionality. The final technique utilises conjugation. At this point, there is a reaction between the Au NP and the bifunctional component, at the same time the other group functions as a site for coupling. One of the challenges of the initial strategy occurs when the functional groups become incompatible and these can potentially undergo a reaction with the surface. The solvent and particle size mainly influence the types of stabilizing ligands. In most cases, thiol capping ligands allow different functional groups to be introduced. They create compact layers of ligands which give stability to the particles at the core. The groups that are commonly used for the functionalization of metal NPs are: NH_2, COOH, and OH (Kim et al., 2002). These guarantee that the nanoparticle environment is stable and compatible as they will be utilized as the centre for additional chemical reactions as soon as they bind to the particle surface. Amines are another group that can be used to modify the surface of the. Their bond with amino group and metal surface is not as strong as the thiolate groups, which have an influence on their size (Caruso, 2001).

2.5.5 Applications of gold nanoparticles in biosensors

Current studies show that the application of gold nanoparticles in biosensors provides room for novel and more efficient sensors. Nanoparticles show a few points of interest in analytical sciences when utilized as transducers or as a part of the recognition layer in a large detecting instrument. The natural properties of Au NPs when utilized as transducers improves number of reaction sites, mass transport availability of reaction sites and dispersion of optical signals due to confined SPR (Wang, 1998). When they are used as a component of the recognition layer, the enhancement of the biosensor signal can be accomplished by the increase of the area to volume ratio that ensures the quantity of biocomponents attached is increased in the detecting surface. The activity of target analytes in biological tests become faster, adaptable and more sensitive when nanoscale particles are assembled, with various benefits over conventional strategies. (Zhang et al., 2002). As a result, this study utilized Au NPs to improve sensor performance. Classification of gold NP-based biosensors includes, electrochemical, piezo-electric and optical biosensors. The roles that Au NPs have been utilised in biosensing development and the procedure of Au NPs in improving the overall outcome of results are in highlighted in Table 2.1.

Table 2.1: Analytical performance of Au NPs on various biosensors

Type of transduction	Principle of detection	Bioreceptor	Analyte	References
Optical	Absorption and reflection	Peptide nucleic acid	DNA	(Peng & Miller,2011)
Electrochemical	Current and potential	Glucose oxidase	Glucose	(Zhang et al.,2015)
Optical and Electrochemical	Absorption and current	Cholesterol oxidase	Cholesterol	(Galdino et al.,2017)

Table 2.1 shows the various functions of Au NPs in biosensors. They have been used in optical biosensors for increasing the sensitivity and in electrochemical biosensors for fast electron transfer. This study used a combination of the two types of sensors to make a combination optical and electrochemical biosensor. The biosensor is expected to offer improved sensitivity, selectivity and stability and this will be done by embedding Au NRs to a metal organic framework (MOF). Metal organic frameworks have some unique properties, which can be used to enhance sensitivity and selectivity.

2.6 Metal Organic Frameworks

Metal organic frameworks (MOFs) are made out of a variety of porous components which important building blocks in various fields like optics, gas storage, catalysis, drug delivery and biosensors (Ethiraj et al, 2015). The great interest in the research of MOFs comes from their unique properties that are not found in other porous materials. In comparison with zeolite porous materials, hydrides of metal complexes and activated, MOF properties encompasses all these material and further exceeds them (Doonan et al., 2017). Some of these features are very low densities, thermal stability, distinct well-ordered structures, facile synthesis, greater than 6000 m^2/g internal surface area and a wide range of features appropriate for physical and chemical uses (Butova et al, 2016). Another advantage of MOFs is that they optimize the efficiency of chemical structures by combining organic and inorganic elements (Lu et al., 2012). Metal organic frameworks comprise of two or more secondary building units (SBUs) (Eddaoudi et al., 2002; Tanabe et al., 2011). The SBUs have two categories, which include metal-containing units that range from one single metal atom to infinite groups and polytopic organic linkers that slot in metal atoms (Furukawa et al., 2013; Zhou et al., 2012). The metal-containing SBUs are usually finite units with extension points, which produce a clear geometrical shape like a square or an octahedron (Serre et al., 2004; Bosch et al., 2014). Polytopic linkers into intermittent frameworks combine these shapes. Novel MOF materials can be attained when several factors are considered (Cavka et al., 2008). Although design and synthesis techniques still depend on trial-and-error experimentations and serendipity to discover novel MOFs, numerous methodical and facile synthetic methods have been developed (Cavka et al., 2008).

2.6.1 Classification of MOFs

The MOF abbreviation is commonly associated with a general type of compounds. Nevertheless, when an ordinary number follows, it specifies a distinct MOF. (Guo et al., 2016). Various metal organic frameworks are categorized into groups with similar designation of letters but designation not rendering their structural similarities but the location where they were discovered (Lei et al., 2014). Some of these MOFs include, LIC, MIL, UiO and HKUST. A different family of metal organic frameworks has a topology for zeolites. These have metal ions like copper, iron and zinc encompassed by nitrogen atoms in a tetrahedral shape connected via imidazole rings, that possess various functions. This

family of MOFs are assigned the abbreviation ZIF for zeolite imidazolate framework with a specific number afterwards to identify topology (Schoedel et al., 2016).

2.6.2 Zeolitic imidazolate frameworks (ZIFs)

Zeolitic imidazolate frameworks are a division of metal−organic frameworks which possess three dimensional structures linked by metal centres and organic linkers centred on imidazolate species (Alaimo et al., 2009). Over the past years, the basic synthesis of over 90 ZIF structures has been achieved, together with crystal topologies which are not yet recognized in the synthesis of zeolites (Stephenson et al., 2016; Zhang et al., 2013). The ZIF structures can be intrinsically hydrophobic if the imidazole linkers do not have hydrophilic functional groups (Shamsaei et al., 2016; Chen et al., 2014). Furthermore, ZIF structures are known to be quite flexible to the extent of permitting the passage of molecules larger than their crystallographically derived aperture size (Esken et al., 2010; Karagiaridi et al., 2012; Liu et al., 2016). Different from zeolites with rather rigid structures, there is substantial proof that the aperture of ZIF-8 is extremely flexible, and there happens to be no sharp molecular sieving at its nominal aperture size of 3.4 Å (Tanaka et al., 2012; Nordin et al., 2014). The bulky cages of ZIF-8 have been proven to be reachable to a series of hydrocarbon molecules with kinetic diameters of 4.3−5.85 Å that are way larger than its nominal crystallographic aperture size. This structural flexibility unlocks new possibilities for ZIF-8 as an effective material with unique separation capabilities, at the same time creating an uncertainty regarding the variety of molecules that can be adsorptively or kinetically separated with ZIF-8. The 5-membered imidazole ring controls the scale of the ZIF structure, but the topology is driven mainly by the linker (Coronas, 2010). With careful control particularly of the shape of the linker isoreticular series can be prepared with the topology of the zeolite gmelinite (zeolite framework code GME) and zeolite rho (RHO). Occasionally rogue structures are observed with colossal cages. The one in ZIF-100 is based on a polyhedron with 264 vertices and is made up of 7524 vertices (Wand, 2012).

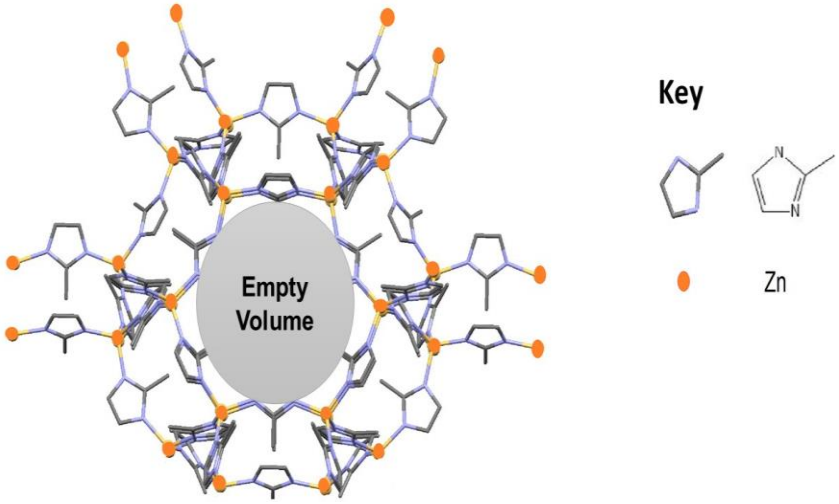

Figure 2.6: Structure of ZIF-8

Figure 2.6 shows the structure of ZIF-8. The framework can have pores with a wide range of functional groups because of the ready availability of substituted imidazoles. The structure has an empty volume where hybridization of metallic nanoparticles (either naked or surfactant-stabilized) can occur. This yields a porous host matrix of nanoparticle-MOFs that offer a wide array of new possibilities. There are many methods to load other metal species into MOFs and they can be classified into chemical vapor infiltration, solution impregnation and encapsulation method (Cole-Hamilton, 2003). This study utilizes ZIF-8 amongst other types of MOFs because it has larger pore size and surface area, which are desirable for depositing small Au NPs.

2.7 References

Akyilmaz, E., Yorganci, E., Asav, E. 2010. Do copper ions activate tyrosinase enzyme? A biosensor model for the solution. *Bioelectrochemistry.*, 78:155–160.

Arruebo, M., Valladares, M. & González-Fernández, Á. 2009. Antibody-conjugated nanoparticles for biomedical applications. *Journal of Nanomaterials*, 2009.

Authier, F., Métioui, M., Bell, A.W. & Mort, J.S. 1999. Negative regulation of epidermal growth factor signaling by selective proteolytic mechanisms in the endosome mediated by cathepsin B. *Journal of Biological Chemistry*, 274(47): 33723–33731.

Bamoulid, J., Courivaud, C., Crepin, T., Carron, C., Gaiffe, E., Roubiou, C., Laheurte, C., Moulin, B., Frimat, L., Rieu, P., Mousson, C., Durrbach, A., Heng, A.E., Rebibou, J.M., Saas, P. & Ducloux, D. 2016. Pretransplant thymic function predicts acute rejection in

antithymocyte globulin-treated renal transplant recipients. *Kidney International*, 89(5): 1136–1143.

Butova, V. V, Soldatov, M.A., Guda, A.A., Lomachenko, K.A. & Lamberti, C. 2016. Metal-organic frameworks: structure, properties, methods of synthesis and characterization. *Russian Chemical Reviews*, 85(3): 280–307.

Byrne, B., Stack, E., Gilmartin, N. & O'Kennedy, R. 2009. Antibody-based sensors: Principles, problems and potential for detection of pathogens and associated toxins. *Sensors (Switzerland)*, 9(6): 4407–4445.

Campbell, I.D., Baron, M., Cooke, R.M., Dudgeon, T.J., Fallon, A., Harvey, T.S. & Tappin, M.J. 1990. Structure-function relationships in epidermal growth factor (egf) and transforming growth factor-alpha (TGF-α). *Biochemical Pharmacology*, 40(1): 35–40.

Carpenter, G., Lembach, K.J., Morrison, M.M. & Cohen, S. 1975. Characterization of the binding of 125-I-labeled epidermal growth factor to human fibroblasts. *The Journal of biological chemistry.*, 250(11): 4297–304.

Carroll, L. 2006. The Stages of Chronic Kidney Disease and the Estimated Glomerular Filtration Rate.*The journal of Lancaster General Hospital.*, 1(2): 64–69.

Caruso, F. 2001. Multilayer assemblies of silica-encapsulated gold nanoparticles on decomposable colloid templates. Adv Mater., 13:1090–4.

Chang, S., Shih, C., Chen, D. 1999. The shape transition of gold nanorods. *Langmuir*., 15: 701–9.

Chen, H. 2007. Methotrexate conjugated to gold nanoparticles inhibits tumor growth in a syngeneic lung tumor model. *Mol Pharm.,* 4:713–22.

Chen, J. 2005. Gold nanocages: bioconjugation and their potential use as optical imaging contrast agents. *Nano Lett*., 5:473–7.

Chen, J., McLellan, M., Siekkinen, A. 2006. Facile synthesis of gold-silver nanocages with controllable pores on the surface. *J Am Chem Soc*., 28:14776–7.

Chen, J., Wang, D., Xi, J. 2007. Immuno gold nanocages with tailored optical properties for targeted photothermal destruction of cancer cells. *Nano Lett.,* 7:1318–22.

Chen, Liyong et al. 2014. Synthesis of Au@ZIF-8 Single- or Multi-Core–shell Structures for Photocatalysis. *Chemical Communications*., 50(63): 8651.

Cole-Hamilton, D. J. 2003. Homogeneous Catalysis- New Approaches to Catalyst Separation, Recovery, and Recycling. *Science*., 299: 1702−1706.

Corma, A. 2004. Attempts to Fill the Gap Between Enzymatic, Homogeneous, and Heterogeneous Catalysis. Catal. *Rev. Sci. Eng*., 46: 369−417.

Coronas, J. 2010. Present and Future Synthesis Challenges for Zeolites. *Chem. Eng. J.,* 156: 236−242.

Crespilho, F.N. 2013. Nanobioelectrochemistry: From implantable biosensors to green power generation. *Nanobioelectrochemistry: From Implantable Biosensors to Green Power Generation*: 1–137.

Di Pasqua, A.J., Mishler, R.E., Ship, Y.L., Dabrowiak, J.C. & Asefa, T. 2009. Preparation of antibody-conjugated gold nanoparticles. *Materials Letters*, 63(21): 1876–1879.

Doonan, C., Riccò, R., Liang, K., Bradshaw, D. & Falcaro, P. 2017. Metal-Organic Frameworks at the Biointerface: Synthetic Strategies and Applications. *Accounts of Chemical Research*, 50(6): 1423–1432.

Erkartal, M., Usta, H., Citir, M. & Sen, U. 2016. Proton conducting poly(vinyl alcohol) (PVA)/ poly(2-acrylamido-2-methylpropane sulfonic acid) (PAMPS)/ zeolitic imidazolate framework (ZIF) ternary composite membrane. *Journal of Membrane Science*, 499: 156–163.

Erkartal, Mustafa, Hakan Usta, Murat Citir, and Unal Sen. 2016. Proton Conducting Poly(vinyl Alcohol) (PVA)/ poly(2-Acrylamido-2-Methylpropane Sulfonic Acid) (PAMPS)/ Zeolitic Imidazolate Framework (ZIF) Ternary Composite Membrane. *Journal of Membrane Science.,* 499: 156–63.

Esken, Daniel et al. 2010. Au@ZIFs: Stabilization and Encapsulation of Cavity-Size Matching Gold Clusters inside Functionalized Zeolite Imidazolate Frameworks, ZIFs. *Chemistry of Materials.,* 22(23): 6393–64010.

Esumi, K., Suzuki, A., Aihara, N. 1998. Preparation of gold colloids with UV irradiation using dendrimers as stabilizer*. Langmuir*., 14: 3157–9.

Ethiraj, J., Bonino, F., Lamberti, C. & Bordiga, S. 2015. H2S interaction with HKUST-1 and ZIF-8 MOFs: A multitechnique study. *Microporous and Mesoporous Materials*.

Fartas, F.M., Abdullah, J., Yusof, N.A., Sulaiman, Y. & Saiman, M.I. 2017. Biosensor based on tyrosinase immobilized on graphene-decorated gold nanoparticle/chitosan for phenolic detection in aqueous. *Sensors (Switzerland)*, 17(5).

Fogel, R. & Limson, J. 2016. Developing Biosensors in Developing Countries : South Africa as a Case Study. *Biosensors*, 6: 5.

Frangioni, V. 2003. In vivo near-infrared fluorescence imaging. *Curr Opin Chem Biol.*, 7:626–34.

Freedman, S.J., Sanford, D.G., Bachovchin, W.W., Furie, B.C., Baleja, J.D. & Furie, B. 1996. Articles Structure and Function of the Epidermal Growth Factor Domain of P-Selectin. *Society*, 2960(96): 13733–13744.

Fricker,S. 1996. Medical uses of gold compounds: Past,Present and Future*. Gold Bulletin,* 29 (2): 53-60.

Galdino, N. M., Brehm, G. S., Bussamara, R., Gonçalves, W.D., Abarca Anjari, G.A., Scholten, J.D. 2017. Sputtering deposition of gold nanoparticles onto graphene oxide functionalized with ionic liquids: biosensor materials for cholesterol detection. *J. Mater. Chem. B*, 1: 1-3.

Garcia, M.E., Baker, L.A., Crooks, R.M. 1999. Preparation and characterization of dendrimer-gold colloid nanocomposites. *Anal Chem*., 71: 256–8.

Grieshaber, D., MacKenzie, R., Vörös, J. & Reimhult, E. 2008. Electrochemical Biosensors - Sensor Principles and Architectures. *Sensors*, 8(3): 1400–1458.

Guo, Z., Florea, A., Jiang, M., Mei, Y., Zhang, W., Zhang, A., Săndulescu, R. & Jaffrezic-Renault, N. 2016. Molecularly Imprinted Polymer/Metal Organic Framework Based Chemical Sensors. *Coatings*, 6(4): 42.

Hartwell, L., Mankoff, D., Paulovich, A., Ramsey, S. & Swisher, E. 2006. Cancer biomarkers: A systems approach. *Nat Biotechnol*, 24: 905 – 908.

He, J., Yap, R.C.C., Yee Wong, S., Zhang, Y., Hu, Y., Chen, C., Zhang, X., Wang, J. & Li, X. 2016. Controlled growth of a metal–organic framework on gold nanoparticles. *CrystEngComm*, 18(28): 5262–5266.

Hill, N.R., Fatoba, S.T., Oke, J.L., Hirst, J.A., Callaghan, A.O., Lasserson, D.S. & Hobbs, F.D.R. 2016. Global Prevalence of Chronic Kidney Disease – A Systematic Review and Meta-Analysis. : 1–18.

Hiramatsu, H., Osterloh, F.E. 2004. A simple large-scale synthesis of nearly monodisperse gold and silver nanoparticles with adjustable sizes and with exchangeable surfactants. *Chem Mater*., 16: 2509–11.

Hu, Y., Kazemian, H., Rohani, S., Huang, Y. & Song, Y. 2011. In situ high pressure study of ZIF-8 by FTIR spectroscopy. *Chemical Communications*, 47(47): 12694.

Huang, H. W., Mohan, S. K. & Yu, C. 2010. The NMR solution structure of human epidermal growth factor (hEGF) at physiological pH and its interactions with suramin. *Biochemical and Biophysical Research Communications*, 402(4): 705–710.

Huang, Y., Xu, J., Liu, J., Wang, X. & Chen, B. 2017. Disease-Related Detection with Electrochemical Biosensors, *Sensors,* 17: 2375.

Hutchings, G. J. 2009. Heterogeneous Catalysts- Discovery and Design. *J. Mater. Chem.,* 19: 1222−1235.

Isaka, Y. 2016. Epidermal growth factor as a prognostic biomarker in chronic kidney diseases. *Annals of translational medicine*, 4(Suppl 1): S62.

Jazayeri, M.H., Amani, H., Pourfatollah, A.A., Pazoki-Toroudi, H. & Sedighimoghaddam, B. 2016. Various methods of gold nanoparticles (GNPs) conjugation to antibodies. *Sensing and Bio-Sensing Research*, 9: 17–22.

Jian, M., Liu, B., Liu, R., Qu, J., Wang, H. & Zhang, X. 2015. Water-based synthesis of zeolitic imidazolate framework-8 with high morphology level at room temperature. *RSC Adv.*, 5(60): 48433–48441.

Karagiaridi, Olga et al. 2012. Opening ZIF-8: A Catalytically Active Zeolitic Imidazolate Framework of Sodalite Topology with Unsubstituted Linkers. *Journal of the American Chemical Society*., 134(45): 18790–96.

Kim, F., Song, H., Yang, P. 2002. Photochemical synthesis of gold nanorods. *J Am Chem Soc.*, 124: 14316–7.

Lee, H.Y., Jung, H.S., Fujikawa, K., Park, J.W., Kim, J.M., Yukimasa, T., Sugihara, H. & Kawai, T. 2005. New antibody immobilization method via functional liposome layer for specific protein assays. *Biosensors and Bioelectronics*, 21(5): 833–838.

Lee, W.C., Chien, H.T., Lo, Y., Chiu, H.C., Wang, T.P. & Kang, D.Y. 2015. Synthesis of Zeolitic Imidazolate Framework Core-Shell Nanosheets Using Zinc-Imidazole Pseudopolymorphs. *ACS Applied Materials and Interfaces*, 7(33): 18353–18361.

Lee, Y., Jeong, J., Lee, G., Moon, J.H. & Lee, M.K. 2016. Covalent and Oriented Surface Immobilization of Antibody Using Photoactivatable Antibody Fc-Binding Protein Expressed in Escherichia coli. *Analytical Chemistry*, 88(19): 9503–9509.

Leff, V., Brandt, L., Heath, J.R. 1996. Synthesis and characterization of hydrophobic, organically soluble gold nanocrystals functionalized with primary amines. *Langmuir*., 12:4723–30.

Lei, J., Qian, R., Ling, P., Cui, L. & Ju, H. 2014. Design and sensing applications of metal – organic framework composites. *Trends in Analytical Chemistry*, 58: 71–73.

Li, Y., Schluesener, H.J. & Xu, S. 2010a. Gold nanoparticle-based biosensors. *Gold Bulletin*, 43(1): 29–41.

Li, Z. & Zeng, H.C. 2013. Surface and bulk integrations of single-layered Au or Ag nanoparticles onto designated crystal planes {110} or {100} of ZIF-8. *Chemistry of Materials*, 25(9): 1761–1768.

Lin, Y., Liu, K., Wang, C., Li, L. & Liu, Y. 2015. Electrochemical Immunosensor for Detection of Epidermal Growth Factor Reaching Lower Detection Limit: Toward Oxidized Glutathione as a More Efficient Blocking Reagent for the Antibody Functionalized Silver Nanoparticles and Antigen Interaction. *Analytical Chemistry*, 87(16): 8047–8051.

Lu, G., Li, S., Guo, Z., Farha, O.K., Hauser, B.G., Qi, X., Wang, Y., Wang, X., Han, S., Liu, X., Duchene, J.S., Zhang, H., Zhang, Q., Chen, X., Ma, J., Loo, S.C.J., Wei, W.D., Yang, Y., Hupp, J.T. & Huo, F. 2012. Imparting functionality to a metal-organic framework material by controlled nanoparticle encapsulation. *Nature Chemistry*, 4(4): 310–316.

Lu, He-Shu et al. 2001. Crystal Structure of Human Epidermal Growth Factor and Its Dimerization. *Journal of Biological Chemistry.,* 276(37): 34913–17.

Majzik, A., Fülöp, L., Csapó, E., Bogár, F., Martinek, T., Penke, B., Bíró, G. & Dékány, I. 2010. Functionalization of gold nanoparticles with amino acid, β-amyloid peptides and fragment. *Colloids and Surfaces B: Biointerfaces*, 81(1): 235–241.

Makaraviciute, A. & Ramanaviciene, A. 2013. Site-directed antibody immobilization techniques for immunosensors. *Biosensors and Bioelectronics*, 50: 460–471.

Manna, A., Imae, T., Aoi, K. 2001. Synthesis of dendrimer-passivated noble metal nanoparticles in a polar medium: comparison of size between silver and gold particles. *Chem Mater*., 13: 1674–81.

Martin, R. 1994. Nanomaterials: a membrane-based synthetic approach. Science., 266: 1961–6.

Mehrotra, P. 2016. Biosensors and their applications - A review. *Journal of Oral Biology and Craniofacial Research*, 6(2): 153–159.

Nguyen, I. 2012. A Zeolite Imidazolate Framework ZIF-8 Catalyst for Friedel-Crafts Acylation. *Chinese Journal of Catalysis*, 33(4–6): 688–696.

Nordin, N. A. H. M. et al. 2014. Aqueous Room Temperature Synthesis of Zeolitic Imidazole Framework 8 (ZIF-8) with Various Concentrations of Triethylamine. *RSC Adv.* 4(63): 33292–300.

Ojo, A. 2014. Addressing the global burden of chronic kidney disease through clinical and translational research. *Transactions of the American Clinical and Climatological Association*, 125(1): 229-43–6.

Oldenburg, J., Averitt, D., Westcott, L. 1998. Nanoengineering of optical resonances. *Chem Phys Lett.,* 288:243–7.

Park, J. & Kim, M. 2015. Strategies in Protein Immobilization on a Gold Surface. , 24(1): 1–8.

Peng, H., Miller, B.L. 2011. Recent advancements in optical DNA biosensors: Exploiting the plasmonic effects of metal nanoparticles. *The Analyst*, 136(3): 436–447.

Price, C. P. 2001. Point of care testing. *BMJ*, 322: 1285 – 1288.

Radloff, C., Vaia A., Brunton, J. 2005. Metal nanoshell assembly on a virus bioscaffold. Nano *Lett*., 5:1187–91.

Rahmani, M., Fard, H.G., Ahmadi, M.T., Habibiyan, H., Rahbarpour, S. & Rahmani, K. 2017. Analytical investigation on the electrooptical properties of graphene nanoscrolls for SPR-based sensor application. *Journal of Computational Electronics*, 16(3): 787–795.

Rechnitz, G.A. 1978. Biochemical electrodes uses tissues slice. *Chem Eng News.* 56:16–21.

Reetz, T., Helbig, W. 1994. Size-selective synthesis of nanostructured transition metal clusters. *J Am Chem Soc*., 116: 7401–2.

Reimers, Jeffrey R. et al. 2016. Gold Surfaces and Nanoparticles Are Protected by Au(0)–thiyl Species and Are Destroyed When Au(I)–thiolates Form. *Proceedings of the National Academy of Sciences*., 113(11): E1424–33.

Rogers, K.R. 2000. Principles of Affinity-Based Biosensors. *Molecular Biotechnology*, 14(2): 109–130.

Rösler, C., Esken, D., Wiktor, C., Kobayashi, H., Yamamoto, T., Matsumura, S., Kitagawa, H. & Fischer, R.A. 2014. Encapsulation of bimetallic nanoparticles into a metal-organic framework: Preparation and microstructure characterization of Pd/Au@ZIF-8. *European Journal of Inorganic Chemistry*, 2014(32): 5514–5521.

Sajid, M., Kawde, A.N. & Daud, M. 2015. Designs, formats and applications of lateral flow assay: A literature review. *Journal of Saudi Chemical Society*, 19(6): 689–705.

Sanders, J. K. M. 1999. Supramolecular Catalysis in Transition. In Supramolecular Science: Springer: Dordrecht, Netherlands, pp 273−286.

Schoedel, A., Li, M., Li, D., O'Keeffe, M. & Yaghi, O.M. 2016. Structures of Metal-Organic Frameworks with Rod Secondary Building Units. *Chemical Reviews*, 116(19): 12466–12535.

Scognamiglio, V., Arduini, F., Palleschi, G., Rea, G. 2014. Biosensing technology for sustainable food safety. *Trends Anal Chem*. 62:1–10.

Scott, J., Wilson, M., Crooks, M. 2005. Synthesis, characterization, and applications of dendrimer-encapsulated nanoparticles. *J Phys Chem B*., 109: 692–704.

Shamsaei, Ezzatollah et al. 2016. Aqueous Phase Synthesis of ZIF-8 Membrane with Controllable Location on an Asymmetrically Porous Polymer Substrate. *ACS Applied Materials and Interfaces*., 8(9): 6236–44.

Snyder, S. & Pendergraph, B. 2005. Detection and evaluation of chronic kidney disease. *American Family Physician*, 72(9): 1723–1740.

Stephenson, C.J., Whitford, C.L., Stair, P.C., Farha, O.K. & Hupp, J.T. 2016. Chemoselective Hydrogenation of Crotonaldehyde Catalyzed by an Au@ZIF-8 Composite. *ChemCatChem*, 8(4): 855–860.

Suzuki, D., Kawaguchi, H. 2005. Gold nanoparticle localization at the core surface by using thermosensitive core-shell particles as a template*. Langmuir*, 21:12016–24.

Tadepalli, S., Yim, J., Cao, S., Wang, Z., Naik, R.R. & Singamaneni, S. 2018. Metal-Organic Framework Encapsulation for the Preservation and Photothermal Enhancement of Enzyme Activity. *Small*, 1702382: 1702382.

Tanaka, Shunsuke et al. 2012. Size-Controlled Synthesis of Zeolitic Imidazolate Framework-8 (ZIF-8) Crystals in an Aqueous System at Room Temperature. *Chemistry Letters.,* 41(10): 1337–39.

Thevenot, D.R., Toth, K., Durst, R.A., Wilson, G.S. 2001. Electrochemical biosensors: recommended definitions and classification. *Biosens Bioelectron*., 16:121–131.

Thevenot, R., Toth, K., Durst, R.A., Wilson, G.S. 1999. Electrochemical biosensors: recommended definitions and classification. *Pure Appl Chem*., 71:2333–2348.

Thobhani, S., Attree, S., Boyd, R., Kumarswami, N., Noble, J., Szymanski, M. & Porter, R.A. 2010. Bioconjugation and characterisation of gold colloid-labelled proteins. *Journal of Immunological Methods*, 356(1–2): 60–69.

Tuninetti, J.S., Rafti, M. & Azzaroni, O. 2015. Early stages of ZIF-8 film growth: the enhancement effect of primers exposing sulfonate groups as surface-confined nucleation agents. *RSC Adv.*, 5(90): 73958–73962.

Van der Zande, I., Boehmer, R., Fokkink, J. 1997. Aqueous gold sols and rod-shaped particles. *J Phys Chem B*., 101: 852–4.

Venugopal, V. 2002. Biosensors in fish production and quality control. *Biosens Bioelectron.*, 17:147–157.

Vidotti, M., Carvalhal, R.F., Mendes, R.K., Ferreira, D.C.M. & Kubota, L.T. 2011. Biosensors

based on gold nanostructures. *Journal of the Brazilian Chemical Society*, 22(1): 3–20.

Wang, J. 1998. DNA biosensors based on peptide nucleic acid (PNA) recognition layers. A review. *Biosens Bioelectron*. 13:757–762.

Wang, J. 2008. Electrochemical glucose biosensors. *Chem Rev*., 108:814–825.

Wang, Y., Wang, L., Chen, H., Hu, X. & Ma, S. 2016. Fabrication of Highly Sensitive and Stable Hydroxylamine Electrochemical Sensor Based on Gold Nanoparticles and Metal-Metalloporphyrin Framework Modified Electrode. *ACS Applied Materials and Interfaces*, 8(28): 18173–18181.

Wang, Z. 2012. Needs and Trends in Rational Synthesis of Zeolitic Materials. *Chem. Soc. Rev*., 41: 1729−1741.

Weare, W., Reed, M., Warner, M.G. 2000. Improved synthesis of small (dCORE ~ 1.5 nm) phosphine-stabilized gold nanoparticles. *J Am Chem Soc*., 122: 12890–1.

Welch, N.G., Scoble, J.A., Muir, B.W. & Pigram, P.J. 2017. Orientation and characterization of immobilized antibodies for improved immunoassays (Review). *Biointerphases*, 12(2): 02D301.

Yim, C., Lee, H., Lee, S. & Jeon, S. 2017. One-step immobilization of antibodies on ZIF-8/Fe_3O_4 hybrid nanoparticles for the immunoassay of Staphylococcus aureus. *RSC Adv.*, 7(3): 1418–1422.

Zhang, J., Burt, D.P., Whitworth, A.L., Mandler, D., Unwin, P.R., Jaafar, M.M., Ciniciato, G.P.M.K., Ibrahim, S.A., Phang, S.M., Yunus, K., Fisher, A.C., Iwamoto, M., Vengadesh, P., Ohnuki, H., Saiki, T., Kusakari, A., Endo, H., Ichihara, M. & Wang, J. 2015. Electrochemical Glucose Biosensors Electrochemical Glucose Biosensors. *Physical Chemistry Chemical Physics*, 11(18): 3490.

Zhang, J., Campbell, R.E., Ting, A.Y., Tsien, R.Y. 2002. Creating new fluorescent probes for cell biology. *Nat Rev Mol Cell Biol.*, 3:906–918.

Zhang, Ke et al. 2013. Exploring the Framework Hydrophobicity and Flexibility of Zif-8: From Biofuel Recovery to Hydrocarbon Separations. *Journal of Physical Chemistry Letters.,* 4(21): 3618–22.

Zheleznova, N.N., Wilson, P.D. & Staruschenko, A. 2011. Epidermal growth factor-mediated proliferation and sodium transport in normal and PKD epithelial cells. *Biochimica et*

Biophysica Acta - Molecular Basis of Disease, 1812(10): 1301–1313.

Zhou, K., Mousavi, B., Luo, Z., Phatanasri, S., Chaemchuen, S. & Verpoort, F. 2017. Characterization and properties of Zn/Co zeolitic imidazolate frameworks vs. ZIF-8 and ZIF-67. *J. Mater. Chem. A*, 5(3): 952–957.

CHAPTER THREE

SYNTHESIS AND CHARACTERIZATION OF NANOMATERIALS AND COMPOSITES

3.1 Introduction

Nanoparticles have been on the focus in the past years due to their attractive physical and chemical characteristics. Compared with the bulk noble metal, metal nanoparticles exhibit distinct photonic and electronic properties coming about because of their shape and size and additionally the dielectric constant of their encompassing environment. Among the noble metals, gold nanoparticles (Au NPs) have a more extensive region of utilization because of the presence of their plasmon resonance in the visible region and their high chemical stability (Stephenson et al., 2016).

Synthesis of nanomaterials

Methods of producing various Au NPs are grouped into two techniques, these are the top down and bottom up technique. Some common techniques for making Au NPs by using the bottom up method are in focus. The Turkevich method was first done in 1951 and is common for producing spherical Au NPs in the 10-20 nm range (Turkevich & Stevenson, 1951; Niidome et al., 2003). The technique's procedure has Au^{3+} being reduced to Au^{0} with amino acids, citrate or ultraviolet light as reducing agents. Capping or stabilizing agents are used to stabilize the size of Au NPs. The Brust method was first discovered in 1994 (Brust et al., 1994; Waters et al., 2003). This procedure for this technique has two stages to produce 1.5 nm - 5.2 nm Au NPs by use of organic solvents. Faraday's two stage method inspired the Brust method. Using this technique, there is a transfer of Au salt from a solution which is aqueous to organic solvents like toluene where a stage transfer agent is utilized (Faraday, 1857). Another modern method is to use plants (Reddy and Torati, 2013). Some of the exceptional candidates for biosynthesizing Au NPs are plants, due to them being bio-friendly (Dauthal and Mukhopadhyay, 2012; Ganesh et al., 2011). Some of the green advantages of synthesizing Au NPs by making use of plants or plant extracts is the use of biocomponents which are nontoxic for capping and reducing AuNPs (Song et al., 2009; Narayanan and

Sakthivel, 2010), restricting formation of waste, no extra purification steps required and ease of availability (Jayaseelan et al., 2013; Kumar et al, 2011). Though the Turkevich and Brust methods can produce spherical Au NPs, Au NPs can also occur in distinct nanostructures such as rods, cages and cubes. The widespread method to generate Au NPs in different shapes is seed mediated growth (Shankar et al., 2005; Bridges et al., 2013). In this method, seed particles are firstly produced by the reduction of Au salts with a reducing agent that is very strong like sodium borohydride (Shao and Susha, 2012). Changing the concentration of reducing agents, seeds and structure directing agents varies the geometry of gold NPs (Faghih and Waks, 2009). The gold nanorods in this study were made using the seed mediated growth method.

The use of organic solvents has been utilized extensively in many ZIFs syntheses. These solvents comprise of methanol, dimethylformamide (DMF) and DMF/methanol. Using organic solvents has a challenge of high costs and there is risk of the environment being polluted alongside issues of human health (Ethiraj *et al.*, 2015**;** Rösler *et al.*, 2014**;** Hu *et al.*, 2011). Synthesizing ZIFs requires modest methods to ensure the production of effective applications. Of late, ZIF-8 synthesis has been reported using aqueous synthesis techniques. In comparison to synthesizing ZIFs with organic solvents, using aqueous synthesis methods has great advantage from operational, financial and environmental areas (Tuninetti et al., 2015**;** Zhang *et al.*, 2018). Nonetheless, higher surface areas are seen in organic techniques for ZIF-8 preparation than in aqueous methods. This implies that there are heavy by-products contained in the product. On top of that, the aqueous synthesis needs a lot of imidazole sources to obtain ZIF-8 (Li and Zeng, 2013**;** Nguyen et al., 2012). In this study, we developed a facile synthesis of ZIF-8 using pure water.

Synthesis of composites

Even though MOFs have many exceptional properties, integration of functional guest species into MOF matrices could convey new properties due to the guest–host synergistic effect. Hence, monitoring the synthesis of multicomponent MOF nanostructures is an important route for increasing MOF applicability. There are two ways in which the composites can be produced, either in situ or ex situ technique. In situ synthesis is a technique that enables one-step fabrication of composites with in situ generated nanoparticles from their precursors. The main benefit of using this method is to avoid particle agglomeration and simultaneously maintain a good spatial distribution in the matrix. The disadvantage is that the unreacted educts can hinder the properties of the final material (He

et al., 2016**;** Jian *et al.*, 2015**;** Lee *et al.*, 2015). Ex situ synthesis on the other hand, disperses pre-made nanoparticles directly into the matrix to form composites. The drawback is that there is higher possibility of aggregation (Zhou *et al.*, 2017**;** Erkartal *et al.*, 2016**;** Lu *et al.*, 2012). The synthesis of a gold-cysteine composite can either yield an interaction of end-to-end assembly, side-by-side assembly formation or aggregation-based formation.

Functionalization of Au NRs

The functionalization of Au NRs is done in two ways, either by non-covalent interaction where functional groups are physically adsorbed on the NRs surface or by covalent interaction, where functional groups chemically bind on the surface of the NRs. The various ways of functionalising Au NRs with MOFs are shown in Figure 3.1. In (A), the particles are distributed in a narrow way which matches the cavities and equally dispersed over the volume of the MOF. In (B), there is even distribution of particles in the entire volume of the MOF matrix and they show a broad size dispersion where the dimensions of the pores are smaller than the average particle size.

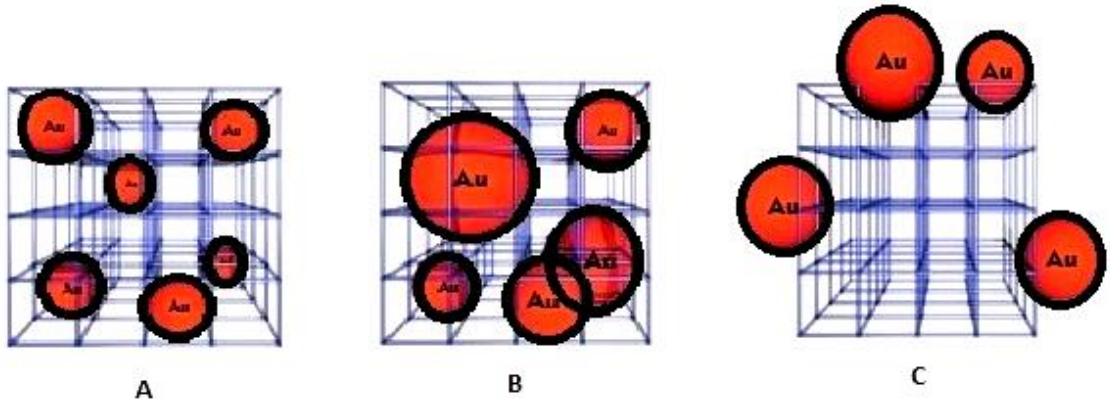

Figure 3.1: Three ways of functionalisation of Au NRs with MOFs via (A) particles homogeneously distributed over the volume of MOF, (B) broad size distribution exceeding pore dimensions and (C) particles anchoring close to the outer surface of the MOF

In (C), the cavity size is smaller than the particles and anchoring is favoured near the MOF outer surface. In this technique the Au NRs accumulate preferentially at the outer surface regions of the MOF which leads to them exceeding the pore sizes of the MOF (Jiang et al., 2013).

Gold nanoparticles can be biofunctionalised with amino acids for their assembly, due to the availability of –SH and $–NH_2$ groups with gold affinity (Love et al., 2005). An amino acid like

L-cysteine is a unique compound for biofunctionalization and self-assembly of gold nanoparticles since it contains both functional groups as shown in Figure 3.2. L-Cysteine is a neutral amino acid with hydrophilic properties. It is reported to bind to gold via its thiol group forming a covalent interaction. Nevertheless, it possesses chemically active terminal groups which $-NH_2$ and –COOH groups.

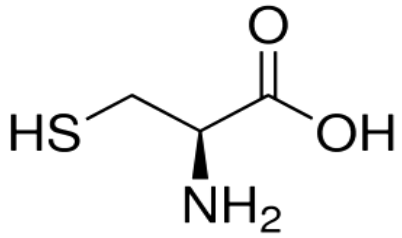

Figure 3.2: Structure of L-cysteine

These groups are influenced by pH and this takes part in monolayer formation and arrangement (Jayabal et al., 2015). For L-cysteine a physisorbed layer forms on top of the chemisorbed monolayer forming a two-layer boundary. It has also been observed that molecules tend to adopt arrangements that permit high levels of van der Waals forces and hydrogen bonding are adopted by molecules, so the free energy of the organic layer is minimised (Park & Kim, 2015). The chemisorption of L-cysteine can occur by both amine and thiol groups. However, that part of L-cysteine originally adsorbed at its amine terminal rearranges to a Au−S bound species which is more stable, as also observed by Kuhnle et al. The strength of the thiolate–gold (RS–Au) bond is close to that of the Au-Au bond, hence it can modify the Au-Au bonding at the gold–sulfur interface (Wang et al., 2016). The Au–S bond in Au-Cys primarily consists of the outermost unpaired electrons in the sulfur $3p_x$ orbital and the Au 6s orbital, which makes it fully filled. As a result, the Au–S bond has the shortest bond length of 2.30 Å (Vidotti et al., 2011).

Characterization of nanomaterials and composites

The morphological, structural composition and electrochemical properties were characterized using spectroscopic, microscopic and electrochemical techniques to confirm the synthesis of nanomaterial and composites. UV-visible spectroscopy measures the light absorption across the ultraviolet and visible light wavelengths. The shape and size of gold

nanorods is mainly influenced by their optical properties. The optical properties strongly depend on how the metal conduction electrons interacts with the electric field part of the incident electromagnetic radiation. The UV-Vis spectra can provide characteristic absorption bands in the visible to infrared part of the spectrum (Yu & Irudayaraj, 2007). A red shift of the bands can be obtained, providing useful information to confirm the degree of functionalization of the gold nanorods with cysteine and the MOF. The red shift occurs when the distance separating the NRs is less than their radii and there is coupling of plasmon oscillations from adjacent particles, making the vibration frequency lower. The red-shift relies on the quantity of particles present and how these particles are oriented within the aggregate (Huang et al., 2009).

FTIR spectroscopy provides accurate identification of compounds by their functional groups. The technique relies on the vibrational excitation of molecular bonds by absorption of infrared light energy (Taha et al., 2013). Determination of these groups is the confirmation of the formation of nanomaterials and composites. It also gives valuable information regarding the type of interaction and bonding transformation in the case of functionalized nanorods. The technique offers high sensitivity and differentiation capacity for characterization of the nanomaterial and composites. Microscopic studies were done using scanning electron microscopy (SEM). The technique can visualize crystal shape, dispersed and agglomerated nanoparticles, surface morphology, particle distribution and surface functionalization (Huseynov et al., 2015). It can specifically examine each particle, including the aggregated particles, which is useful for examining functionalized nanorods. A high-energy electron beam scans across the surface of a specimen and the electron signals emitted are processed, giving rise to a three-dimensional image of the surface topography.

The electrochemical characterizations were done using cyclic voltammetry (CV) technique to determine the physical and electrochemical properties of the nanomaterials and composites. Cyclic voltammetry is the most widely used method for obtaining qualitative information about electrochemical reactions. This technique is used to study the redox behaviour of either solution species or the electrode surface and in this case, oxide deposits on the electrode surfaces can be studied. It offers the rapid identification of redox potentials typical of the electroactive species, offering significant information about the surface coverage, band gaps, kinetics of heterogeneous electron-transfer reactions, conductivity and film thickness (Yu et al., 1997). The electrochemical behavior is dependent on the applied voltammetric scan rate. When various scan rates are used, the diffusion layer thickness immediately changes. When low scan rates are applied, the diffusion layer becomes very thick while at higher scan rates the diffusion layer becomes thinner. Since reversibility or irreversibility shows how the electrode kinetics compete with the mass transport, scan rates

which are quicker promote greater electrochemical irreversibility (Mendoza et al., 2015). The electron transfer kinetics need to be quick enough for reversibility to occur. This allows surface concentrations of oxidation and reduction at the values needed by the Nernst equation to be maintained. Hence, reversibility is depended on the rate of potential change to the scan rate (v) and the standard heterogeneous electron transfer rate constant (k_s) values. When the k_s/v ratio is sufficiently small to an extent that there is no maintenance of Nernstian concentrations, a quasi-reversible process is observed. By reducing the scan rate, a transformation from a quasi-reversible to a reversible process can occur. This allows the surface concentrations to have more time of adjusting to the new values needed by the varying potential. As a result, at low scan rates the value for Ipa/Ipc is closer to one (Neghmouche, 2007).

3.2 Experimental

3.2.1 Reagents and Materials

CTAB capped gold nanorods; CTABAu (Sigma Aldrich), 2-methylimidazole (2-MIM) (99 %, Sigma Aldrich), zinc nitrate hexahydrate; $Zn(NO_2)_3.6H_2O$, L-cysteine (Sigma Aldrich), alumina (Al_2O_3) powder (0.05, 0.3, 1.0 µm) (Buhler), ethanol (99 %, analytical grade) were used. Deionized water was used for aqueous solution preparation.

3.2.2 Preparation of phosphate buffered saline (PBS) (10x = 0.1M) solution

PBS solution was used as a supporting electrolyte and for solution preparation. About 80 g NaCl and 2 g KCl were dissolved into 800 mL distilled water. Approximately 14.4 g $Na_2HPO_4 \cdot 12H_2O$ and 2.4 g KH_2PO_4 were then dissolved into the solution. The pH adjustment to the desired value was done using 1 M HCl or 1 M NaOH solutions followed by dilution to 1 litre with distilled water and stored at room temperature.

3.2.3 Synthesis of nanomaterial and composites

3.2.3.1 Synthesis of ZIF-8

Was prepared by dissolving 0.026 g of (0.12 mmol) zinc nitrate hexahydrate and 0.02 g of 2-MIM (0.24 mmol) into 10 ml of deionized water. The solution was kept still for 4 h at room temperature. Afterwards, the resulting ZIF-8 was taken out, washed with methanol for three times and dried at 60°C overnight.

3.2.3.2 Synthesis of cysteine functionalized Au NRs

Cysteine solution was prepared by dissolution of the corresponding solid in deionized water at a concentration of 1×10^{-3} M. A solution of CTAB capped Au NRs at a concentration of 1 x 10^{-11} M using deionized water. The prepared solutions were mixed at room temperature and left for an hour.

3.2.3.3 Synthesis of CTABAu-ZIF-8 composite

Five milliliters of CTAB capped Au NRs, 0.1 mL of 2-methylimidazole (0.24 mM), and 0.1 mL of $Zn(NO_3)_2 \cdot 6H_2O$ (0.12 mM) were mixed and stirred at 20 °C for 3 h. Next, the mixture solution was set at room temperature without stirring. This allowed ZIF-8 to grow on the gold nanorods surface. After 24 hours, there was centrifugation of the solid products and they were rinsed with methanol three times and dried at 80 °C for 3 h in the oven.

3.2.3.4 Synthesis of cysteine functionalized Au NRs encapsulated with ZIF-8

A cysteine solution of 0.001 M was mixed with CTABAu-ZIF-8 solution at room temperature for 3 hours.

3.2.4 Characterization

3.2.4.1 Spectroscopic characterization

UV-visible absorption studies were performed with Cary 300 dual-beam spectrophotometer using 1 cm quartz cuvette in the wavelength range of 200-900 nm. This was done to determine the nanomaterials and composites formation. FTIR analysis was done by using Perkin Elmer model Spectrum 2 series within 400-4000 cm^{-1}. The samples for FTIR analysis were used directly in powder and aqueous form by placing on the scan plates and recording the spectra. The SEM used was a FEI Nova NanoSEM230, BRUKER AXS (Germany) with the field emission gun. The images were taken at 20 keV. The XRD used was BRUKER AXS (Germany) with LynxEye detector and 2θ range: 5° to 80°.

3.2.4.2 Electrochemical characterization

Electrochemical properties of the synthesized composites and nanomaterials were determined using cyclic voltammetry. Composite suspensions were drop coated on the surface of polished GCE and their CV ran in 0.1 M PBS pH 6.0 as a supporting electrolyte. Scanning the potential from 100 mV to 1450 mV at 50 mV/s was done for conductivity studies. Mass transport and electron transfer kinetics were studied from the effect of scan rate on peak current using Randles-Sevcik plots using Randles-Sevcik equation, scan rates of 20 to 100 mV/s were used.

3.2.4.3 Electrode cleaning procedure

The working electrode was polished with 1.0, 0.3 and 0.05 µm alumina slurries on a wetted polishing micro-cloth pad. The electrode was moved in a circular motion across the surface of the polishing pad followed by rinsing with distilled water. Further rinsing was done by sonication in ethanol and distilled water for 5 minutes.

3.2.4.4 Equipment and apparatus

Computer interfaced with AUTOLAB potentiostat 101 with Nova software was used for all electrochemical measurements. A three-compartment electrochemical cell with GC working electrode (WE) (diameter = 3.0 mm), Pt wire auxiliary electrode (AE) and silver/silver chloride (Ag/AgCl, 3 M KCl) reference electrode (RE) were used for all electrochemical determinations. Ultrasonic cleaner was used for cleaning the WEs.

3.2.5 Optimization of cysteine-gold composites

3.2.5.1 Effect of CTAB

Removal of CTAB from a suspension of gold nanorods was done by careful centrifugation at 12 000 rpm for 10 min. After, the nanorods were redispersed in water via sonication. Gold nanorods without CTAB were prepared and analysed.

3.2.5.2 Effect of reaction time

CTAB capped Au NRs were prepared at a concentration of 1 x 10^{-11} M. Reaction with cysteine at a concentration of 0.001 M was varied from 0-60 mins.

3.2.5.3 Effect of Au NRs and cysteine concentration

The effect of Au NRs concentration was observed in various ratios of Au:Cys for 1.0^{8}:1, 1.5^{7}:1, 1.0^{7}:1 and 2.5^{6}:1. The concetration for L-cysteine was fixed at 0.001 M and a 1 hr reaction time was kept for CTABAu-Cys. The effect of cysteine concentration was also observed in various ratios of Cys:Au for 1.0^{7}:1, 1.0^{8}:1, 1.0^{9}:1 and 1.0^{10}:1. The concetration for Au NRs was fixed at 1 x 10^{-11} M and a 1 hr reaction time was maintained.

3.2.5.4 Effect of volume ratio

A concentration of 1 x 10^{-11} M was maintained for CTABAu in CTABAu-Cys while the volume ratio of CTABAu: Cys was varied from 1:1, 1:3 and 1:5 at a constant cysteine concentration of 0.001 M for 1 hr.

3.2.5.5 Effect of pH

CTAB capped Au NRs and cysteine were prepared at a concentration of 1 x 10^{-11} M and 0.001 M respectively. Various pHs for CTABAu-Cys were prepared from pH of 3, 6 and 9.

3.2.5.6 Effect of temperature

CTAB capped Au NRs and cysteine were prepared at a concentration of 1 x 10^{-11} M and 0.001 M respectively at a pH of 6. The CTABAu-Cys mixture was analysed at various temperatures of 15 °C, 20 °C, 25 °C and 30 °C.

3.3 Results and discussion

The synthesised nanomaterial and composites were characterized using spectroscopic and electrochemical techniques. Successful functionalisation of gold nanorods with cysteine and ZIF-8 was accomplished and results corresponded with other literature values.

3.3.1 Spectroscopic characterization

3.3.1.1 UV-Vis characterization

The UV-Vis spectroscopy technique studies how electromagnetic radiation in the wavelength range of 200 – 800 nm interacts with atoms and molecules. When an atom absorbs energy from a photon, there are changes in electronic energy levels within the atom as electrons are transferred to a higher energy level. The transitions that occur from a lower to a higher energy level are distinct for each element. Therefore, a specific element can be identified based on its absorption spectra.

The UV-Vis absorption spectra of CTAB capped Au NRs (aspect ratio 3.7) is depicted in Figure 3.3. The two characteristic plasmon bands for Au NRs are observed in the absorption spectra confirming the synthesis of Au NRs. The wavelength of the transverse band and longitudinal band was like other Au NRs with the same aspect ratio as found in literature (Boksebeld et al., 2017).

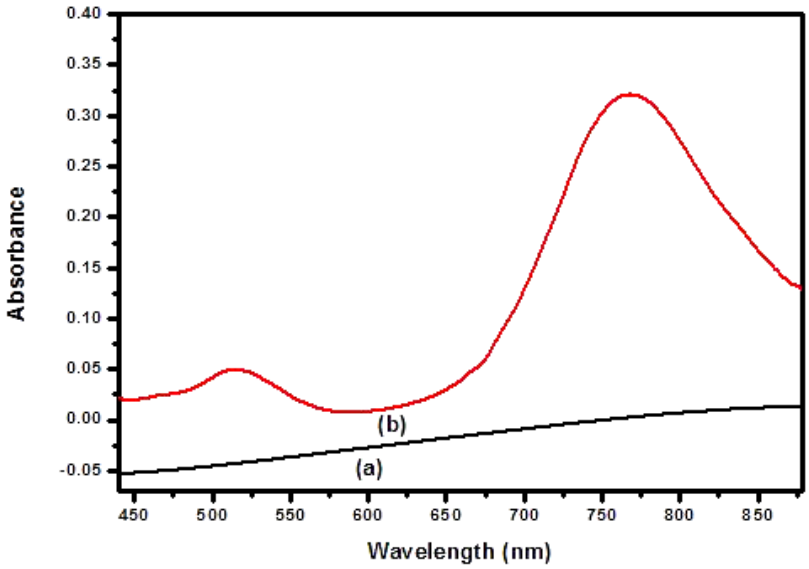

Figure 3.3: UV-Vis absorption spectra of (a) blank and (b) CTABAu

The longitudinal band was due to the oscillation of free electrons along the long axis of the rod and the transverse plasmon band was due to the oscillation of the electrons perpendicular to the major axis of the nanorods. The absorption spectra for other Au nanoparticles of different morphology only produce one absorption band which makes Au NRs with two plasmon bands more sensitive than other nanoparticles (Abdallah et al., 2008).

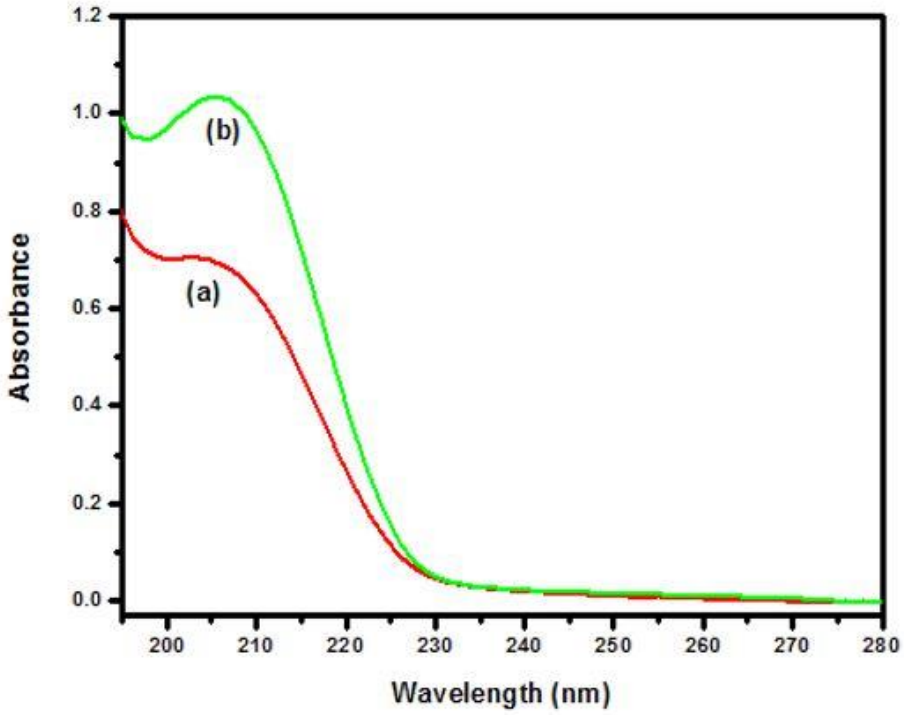

Figure 3.4: UV-Vis absorption spectra of (a) ZIF-8 and (b) zinc nitrate hexahydrate

The UV-Vis absorption spectrum of ZIF-8 is shown in Figure 3.4a. There is a red shift of the peak and broadening compared to that of the precursor, zinc nitrate hexahydrate (Figure 3.4b). This shows that the zinc was changed into the ZIF-8 structure according to the equation:

$$Zn(NO_3)_2.6H_2O + \text{2-MIM} \rightarrow \text{ZIF-8} \qquad (3.1)$$

The absorption due to the electron excitation from the valence band to conduction band corresponds to a specific wavelength, which was used to calculate the band gap according to the equation:

$$E = \frac{hc}{\lambda} \qquad (3.2)$$

Where h = plancks constant, c = speed of light, λ = wavelength, E = band gap energy and 1 eV = 1.6 X 10-19 Joules

The optical band gap was found to be 5.37 eV, this was near other literature values of 5.20 eV (Thanh et al., 2018). The absorption peak at 205 nm for ZIF-8 involved π to π* transitions in the imidazole ring.

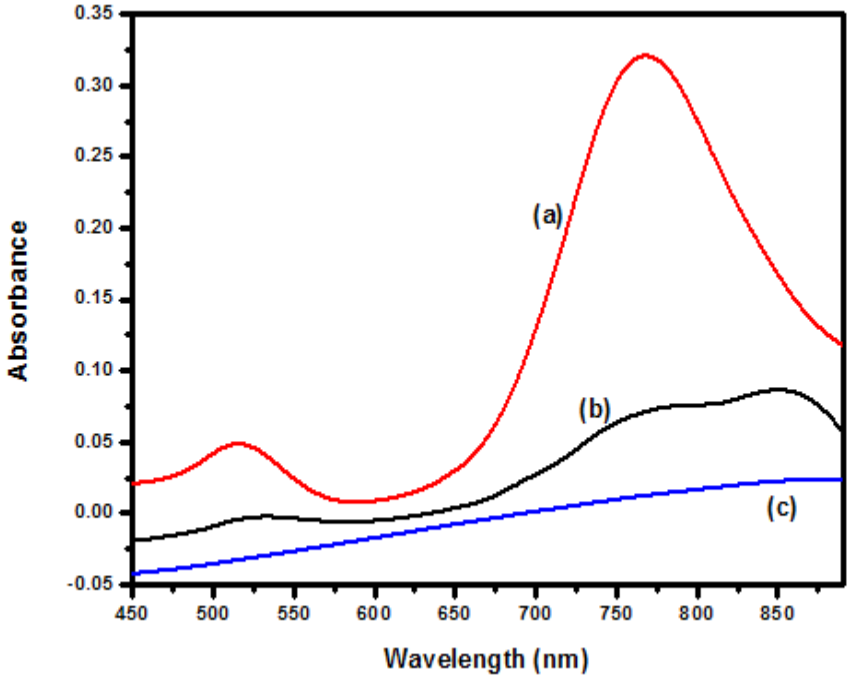

Figure 3.5: UV-Vis absorption spectra of (a) CTABAu, (b) CTABAu-Cys and (c) blank

Figure 3.5 shows the effect of cysteine on the absorption spectra of Au NRs. In this case, after L-Cysteine solution was mixed with gold nanorods (Fig.3.5b), the longitudinal and transverse band became wider and weaker than that of Au nanorods alone. A red shift (2 nm) was observed in the transverse band and longitudinal band (5 nm). The transverse band did not show a significant shift after mixing L-cysteine with Au NRs. This was because the dipoles of the transverse plasmon are separate even when the rods are together. This prohibits interaction significantly. The interaction of the cysteine molecule with the Au NRs surface changed the dielectric constant of the surrounding material, which causes variations in the resonant frequency since the electron density on the surface of the NRs was changed. This caused a considerable red shift observed in the longitudinal LSPR absorption band of the Au NRs confirming their end to end assembly. The aggregation of the Au NRs produced a decrease in the interparticle distance of the NRs, which caused a change in the plasmon coupling and led to a colour change. This intense red-shift, peak location and broadening agree with literature values for gold nanorods functionalised with cysteine (Kesarkar et al., 2015; Wang et al., 2018). Since the Au NRs resulted from a growing and stabilizing technique assisted by CTAB, the CTAB was probably attached only onto the lateral surfaces of the nanorods. Hence, keeping the end of the rods free for bio-conjugation. A hydrophobic microenvironment is created by CTAB molecules close to the NRs surface. In water, a positively charged surface is seen on the nanorods due to CTA^+ ions strongly absorbed at the side surfaces. This results in electrostatic repulsion between nanorods, which contributes

to the stability of the nanorods in solution. This new band in the spectra around 860 nm suggests the formation of aggregates of gold nanorods due to the formation of the Au-S. The aggregation is also confirmed in the wavelength difference between the two observed bands (775 nm for CTABAu and 860 nm for CTABAu-Cys) of 85 nm, which suggests that the nanorods are arranged in chains by the effect of the cysteine molecules with a decrease in the population of Au NRs and an increase in the population of functionalized Au NRs with L-cysteine.

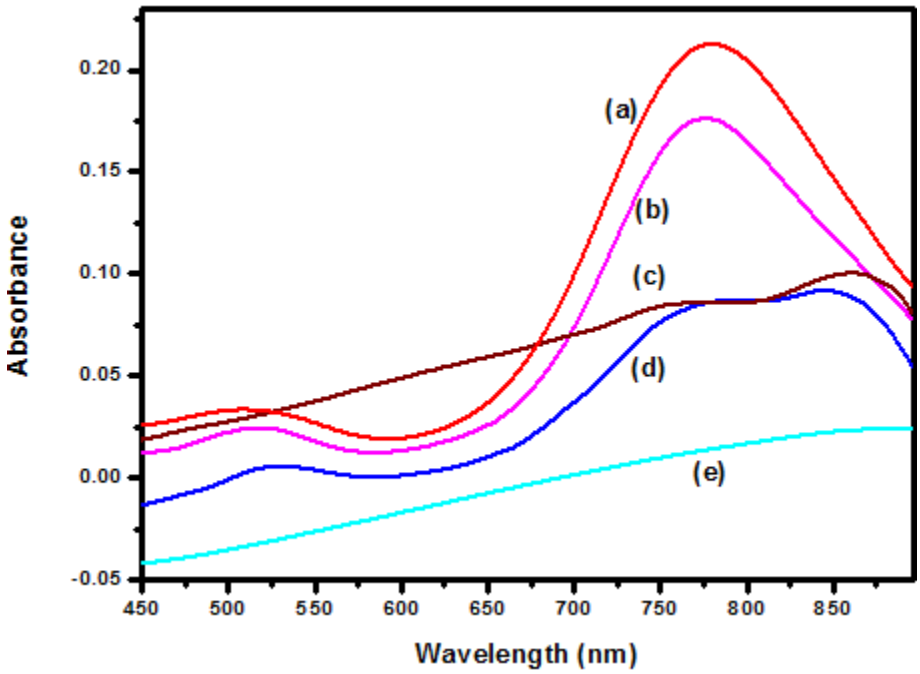

Figure 3.6: UV-Vis absorption spectra of (a) CTABAu-ZIF-8, (b) CTABAu, (c) CTABAu-Cys-ZIF-8, (d) CTABAu-Cys and (e) blank

UV-Vis absorption spectra were recorded to study the effect of Au NRs embedded in ZIF-8. Figure 3.6 (a and b) compares the absorption spectra of CTABAu-ZIF-8 and CTABAu respectively. After addition of ZIF-8, the longitudinal peak moved to a higher wavelength (785 nm). This was due to the altered local environment that change the dielectric constant of Au NRs. This suggested that Au NRs embedded in MOF crystals, maintained surface plasmon effect. The higher refractive index of ZIF-8 is where the red shift was expected to originate from as compared to water. The higher absorbance of CTABAu-ZIF-8 was because of the increased scattering of light originating from the particles of greater size in the dispersion (Au NRs encapsulated in ZIF-8). When cysteine was added to the CTABAu-ZIF-8 composite, the characteristic peak of cysteine functionalized gold and the longitudinal band for Au NRs were clearly visible. This showed that the surface plasmon effect was maintained

due to the high affinity of the thiol moiety for gold in the composite. Accordingly, the MOF precursor of Zn^{2+} ions fully adsorb on Au NR surface via electrostatic interaction, giving full encapsulation of ZIF-8 on Au NP. The MOF showed flexibility due to the swing of the imidazolate linkers, which accommodate cysteine to fit through the narrow pores. This type of post synthetic functionalization produces MOFs with a more viable functionality as the framework remains intact after modification. This causes a framework with Au NRs with a narrow size dispersion fitting with the cavities and evenly spread over the volume of ZIF-8 structure. If the distribution is not homogenous and the particle sizes are larger than the pore dimensions, damage of the ZIF-8 matrix might occur.

3.3.1.2 FTIR characterization

To identify functional groups and confirm the formation of synthesised nanomaterial and composites, FTIR spectroscopy was used. The information obtained from this technique is very specific and it provides high sensitivity to analyse the nature of the bonds. The FTIR spectra for L-cysteine and CTAB capped Au NRs with L-cysteine is shown in Figure 3.7. The band at 3,250 cm^{-1} was assigned to the amine ($–NH_2$) functional group of L-Cysteine. The characteristic band in the wavenumber range of 3100- 2600 cm^{-1} was due to the $v(NH_3^+)$ vibration at L-cysteine and it became weak in the cysteine functionalised Au NRs. This was likely due to a change in their dipole moment when cysteine was bound on a metal surface with high electron density.

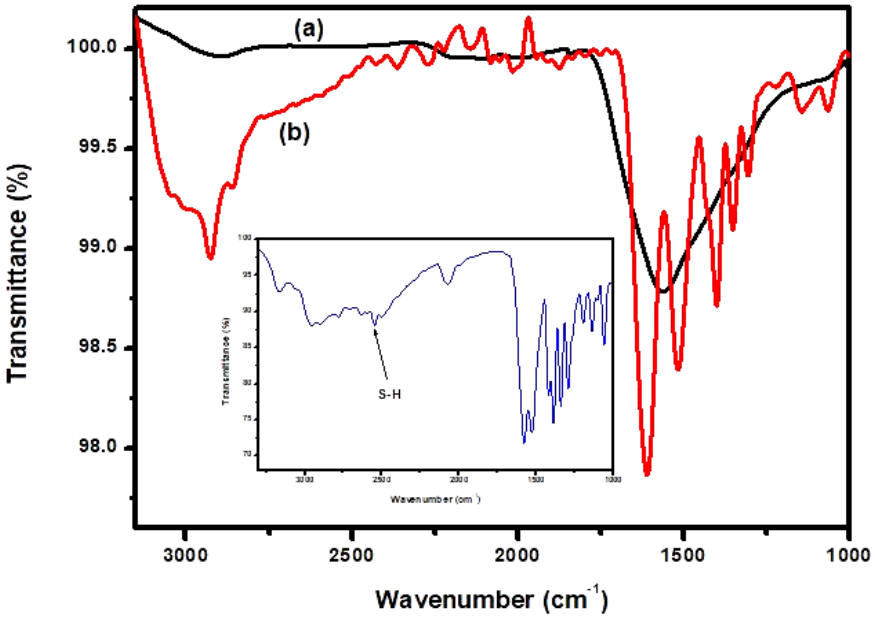

Figure 3.7: FTIR spectra of (a) CTABAu, (b) CTABAu-Cys and inset: L-cysteine

Characteristic peaks at 1,585 cm^{-1}, 1,450 cm^{-1}, 1,430 cm^{-1} and 1,100 cm^{-1} were assigned to v_{asym}(COO), δ(NH) bending, v_{sym}(COO) and v(C–N) of L-Cysteine respectively. Some bands were expanded because of combining bands and over tones which are seen at 2000 cm^{-1}. The peak at 2,550 cm^{-1} represents the δ(S–H) stretching vibration of L-Cysteine. This characteristic peak of S–H was not observed for CTABAu-Cys, which indicated that the S–H bond was cleaved and a new Au–S bond was formed between the L-Cysteine and Au NRs confirming aggregation.

The FTIR spectrum of 2-methylimidazole is shown in Figure 3.8 inset. The N-H stretching was seen at 3012 cm^{-1} and the bands at 3138 and 2930 cm^{-1} were attributed to the aromatic and the aliphatic C–H stretch of the imidazole, respectively. The N-H bending was observed at 1595 cm^{-1}. The C-H deformation bends were assigned to the peaks at 1305 cm^{-1}. Figure 3.8c shows the FTIR spectrum of ZIF-8.

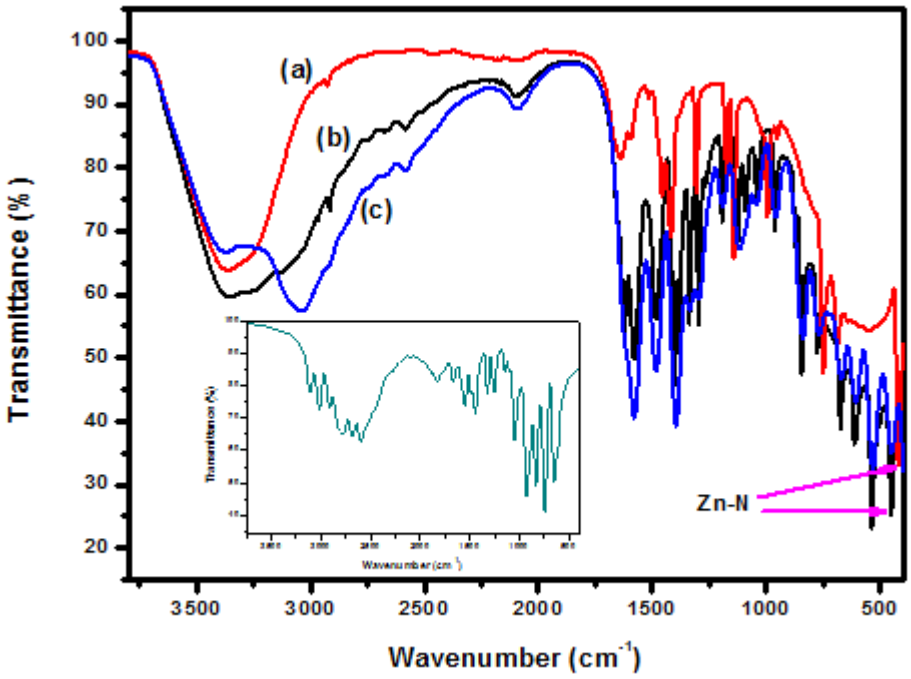

Figure 3.8: FTIR spectra of (a) CTABAu-ZIF-8-Cys, (b) CTABAu-ZIF-8, (c) ZIF-8 and inset: 2-methylimidazole

The absorption bands are mainly linked to the imidazole unit vibrations, therefore can be defined centred on the origin of the bonds. A broad band was observed in the range of 3100 to 3550 cm^{-1} and this was attributed to the v(O–H) stretching of hydrogen bonded water in the sample. The peak at 1590 cm^{-1} was attributed to the C = N stretch mode, whilst the strong and convoluted bands at 1370–1490 cm^{-1} were connected to the whole stretching of

the ring. The bands observed in the range of 900–1370 cm^{-1} were due to the in-plane bending of the ring whereas those under 800 cm^{-1} were due to out-of-plane bending. The absorption band at 422 cm^{-1} was observed for the Zn-N stretching mode for the CTABAu-ZIF-8 composite in Figure 3.8b. The FTIR exhibits the peaks for CTAB which shows symmetric (2850 cm^{-1}) and asymmetric (2920 cm^{-1}) stretching vibrations of the methylene chains. The Zn-N stretching mode was seen at 424 cm^{-1} which shows that the ZIF-8 matrix was not damaged. When cysteine was introduced to the composite (Figure 3.8a), the δ(S–H) stretching vibration of L-cysteine at 2550 cm^{-1} was not observed and the Zn-N stretching mode was seen at 420 cm^{-1}. This confirmed that the post synthetic functionalization method was viable in agreement with the UV-Vis results.

3.3.2 Electrochemical characterization of gold and its composites

3.3.2.1 Cyclic voltammetry

Various platforms of gold nanorods composites were electrochemically studied and their voltammograms are depicted in Figure 3.9. From Figure 3.9, all platforms depict typical characteristic peaks for Au NRs. Most of the voltammograms have one anodic peak and one cathodic peak except for cysteine containing composites that have an additional cathodic peak.

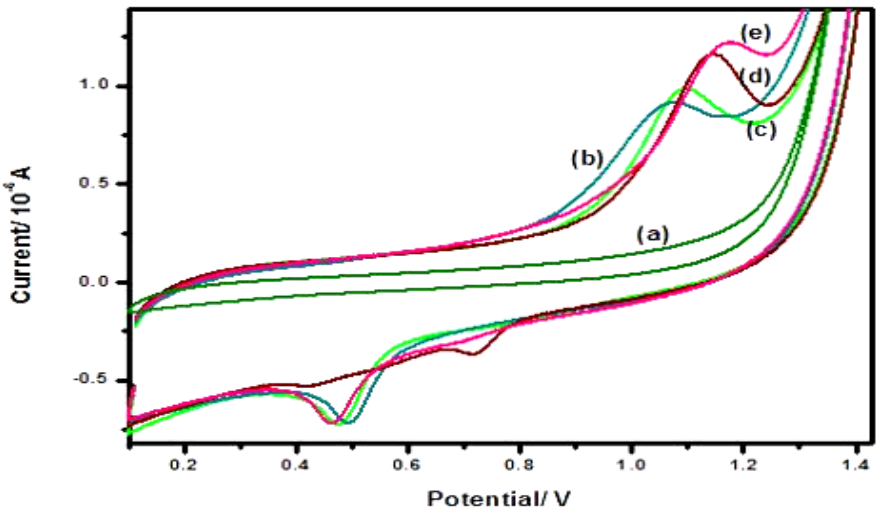

Figure 3.9: CV of (a) GCE, (b) CTABAu/ZIF-8, (c) CTABAu, (d) CTABAu/Cys and (e) CTABAu/ZIF-8/Cys at a scan rate of 50 mV/s in 0.1 M PBS

The anodic peaks observed in the voltammograms were due to monolayer oxide formation at the electrode surface according to equation 3.3. This process occurs at a lower potential than the standard E^{O} value because the standard values were calculated for stable bulk

metal atoms and the presence of CTAB also lowered the potential for monolayer formation. The reaction taking place in cysteine containing composites is according to the equations 3.4-3.5. The second cathodic peak was attributed to the formation of a new gold-cysteine complex which was irreversible (equation 3.5). This was due to a decrease in the gold nanorods accompanied by an increase in the functionalised Au NRs with cysteine as seen in the UV-Vis spectra results (Figure 3.5). The high current density profile of cysteine was due to the deprotonation of sulfhydryl groups leading to more formation of thiyl radicals. The reaction taking place in ZIF-8 containing composites was according to equation 3.6. The ZIF-8 structure with a lot of delocalized electrons of π bonds, due to the 2-methylimidazole, acts as an electron donor to Au NRs in the structure of the ZIF-8 Au hybrid.

The following reactions took place at the electrode surface. Gold was oxidized to the trivalent state according to the equation (Barke and Nugeus, 1997):

$$Au + 3H_20 \leftrightarrow Au(OH)_3 + 3H^+ + 3e \qquad E^o = 1.46\ V \qquad (3.3)$$

Reaction mechanism for cysteine functionalised Au NRs (Barus et al., 2007):

$$R\text{-}SH + Au \leftrightarrow RS\text{-}Au + H^+ + e \qquad E^0 = 1.18\ V \qquad (3.4)$$

$$R\text{-}S\text{-}Au \rightarrow R\text{-}S\bullet + Au \qquad E^0 = 0.45\ V \qquad (3.5)$$

The forward electron transfer from ZIF-8 to Au is described by the equation:

$$ZIF\text{-}8\ (e) + Au \rightarrow ZIF\text{-}8 + Au^{\delta-} \qquad (3.6)$$

Table 3.1 summarizes the electrochemical properties of the platforms obtained from the voltammograms in Figure 3.9. From these it is observed that the presence of cysteine contributed to a positive shift of the anodic peak to higher potentials with an increase in current. While the presence ZIF-8 shifted the anodic peak to less positive potentials with a decrease in current. The cathodic peak for ZIF-8 slightly shifted to more positive potentials whilst after the addition of cysteine the peaks significantly shifted by over 200 mV with the emergence of a new peak at lower positive potentials. Anodic peak broadening was observed for ZIF-8 containing composites. The broadening was due to the bulk ZIF-8 attached to the electrode surface. A sharp anodic peak was observed for CTABAu/Cys showing fast electron transport occurring in the platform. Peak separation greater than 59/n mV were obtained, suggesting quasi-reversible behaviour (Wang, 2000). The CTABAu/Cys platform was more reversible compared to others, exhibiting a lower ΔEp.

Table 3.1: The electrochemical parameters of modified electrodes

GC Modified Electrode	Ipa (μA)	Ipc1 (μA)	Ipc2 (μA)	Epa (V)	Epc1 (V)	ΔEp^0 (V)
CTABAu	0.810	-0.747		1.091	0.465	0.626
CTABAu/Cys	1.220	-0.330	-0.740	1.155	0.720	0.435
CTABAu/ZIF-8	0.780	-0.745		1.073	0.493	0.580
CTABAu/ZIF-8/Cys	1.250	-0.310	-0.620	1.181	0.700	0.481

Hysteresis was seen in the monolayer oxide formation/reduction as the product of the positive sweep electrochemical reaction went through a change after the electron transfer step such that the species and potential range involved in going in one direction varied from the reverse process. Hysteresis was caused by repulsions of dipolar ($Au^{\sigma+}.OH^{\sigma-}$) species during the monolayer growth process. These repulsions increased the energy needed to produce additional dipoles. Some surface dipoles rotated in a place exchange process and this discharged a lot of the repulsion in the surface layer, producing more stable surface deposits.

Another interpretation of the CV voltammograms in Figure 3.9 was to calculate electrochemical bandgaps. Importance of band gaps in fabrication of the transducer is to identify the components that give the most conductivity to the platforms. The electrochemical bandgaps of the synthesized nanomaterial and composites were analyzed. The removal of an electron from the HOMO energy level resembles the oxidation process and the electron addition to the LUMO energy level resembles the reduction process. The transfer of electrons between the energy levels of the electrode and the energy levels of the materials gives rise to the current. The ionization potential (*Ip*) corresponds to the onset potential of oxidation and the electron affinity (*Ea*) corresponds to the onset of reduction as suggested by Bredas *et al.,* 1983 based on experimental electrochemical measurements. The correlation can be expressed by the equations:

$$I_p = -[E_{ox}^{onset} + 4.4]Ev \qquad E_a=-[E_{red}^{onset}+4.4]Ev \tag{3.7}$$

$$E_g = (I_p - E_a)Ev \tag{3.8}$$

Where $[E_{red}^{onset}]$ is the onset reduction and $[E_{ox}^{onset}]$ is the onset oxidation potential vs the Ag/AgCl reference electrode. The values for the onset values were calculated by measuring the intersection point between the baseline and the tangent line drawn to the increasing portion of the current. The difference between HOMO and LUMO energy levels yielded the band gaps (equation 3.8). Band gaps of the platforms studied are tabulated in Table 3.2

Table 3.2: Electrochemical band gap data of the modified electrodes (according to equations 3.7-3.8)

Material	E_{ox}^{onset}	E_{red}^{onset}	E(LUMO)	E(HOMO)	Eg^{CV} (eV)
CTABAu	0.97	0.58	3.43	4.98	1.55
CTABAu/Cys	0.99	0.79	3.41	5.19	1.78
CTABAu/ZIF-8	0.89	0.57	3.51	4.97	1.46
CTABAu/ZIF-8/Cys	0.99	0.78	3.43	5.18	1.75

Cysteine containing composites had the widest band gaps and that with ZIF-8 contributed to lower band gaps. The variations of the band gap in the systems were due to the orientation and size of the materials on the electrode surface influencing the quantum confinement (Haram et al., 2001). Cysteine had a wider band gap due to its orientation on the electrode surface (Fig. 3.10A) and ZIF-8 reduced the band gap due to its bulk structure (Fig. 3.10B), showing less kinetic limitations of charge transfer between the redox centres within the film. The relatively large surface area of ZIF-8 offered more electroactive site, therefore improving the electrochemical response (Nie et al., 2017).

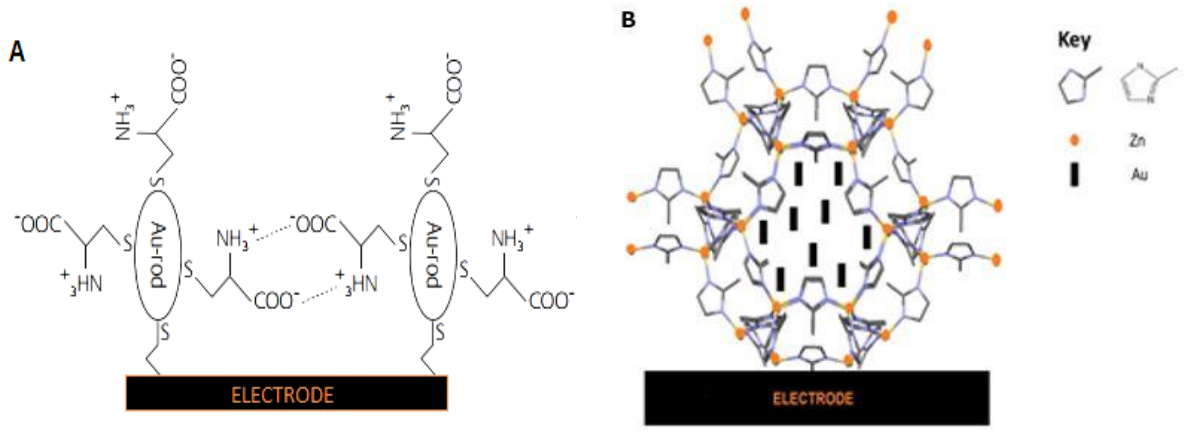

Figure 3.10: Scheme of (A) cysteine binding to gold nanorods and (B) CTABAu/ZIF-8 binding on the electrode surface

3.3.3 Scanning electron microscopy

Scanning electron microscopy studies the interaction of a sample with the kinetic energy from the accelerated electrons. The signals obtained from the electron to sample interactions reveals the sample's morphology, crystalline structure, chemical components and

orientation. The images of the sample can also be scanned in different magnifications. The SEM micrographs of the platforms are displayed in

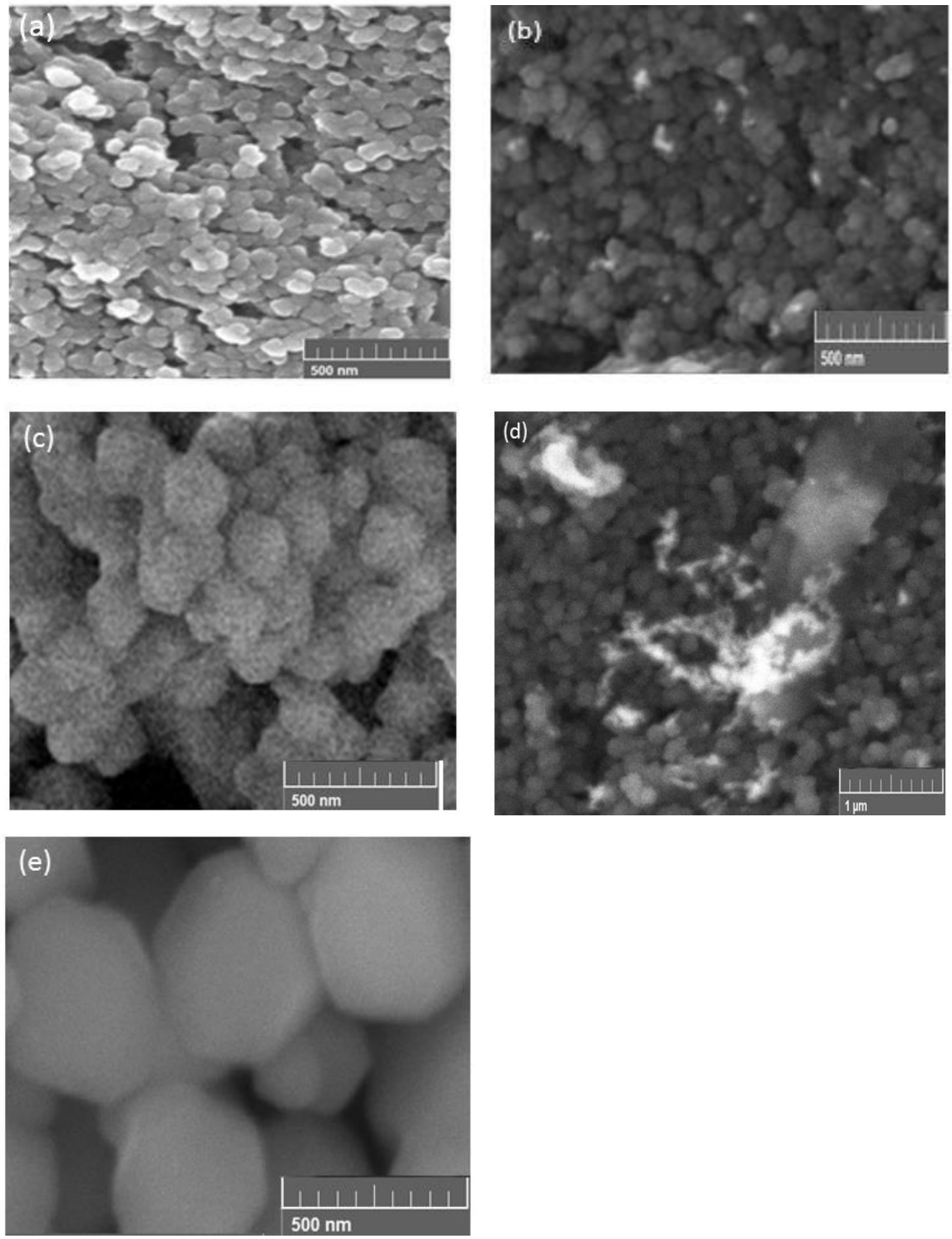

Figure 3:11: SEM micrographs at 104 kx of (a) carbon, (b) CTABAu, (c) ZIF-8 (d) and (d) CTABAu-ZIF\8.

Figure 3.11 shows SEM micrographs at a magnification of 104 kx. The carbon electrode used to analyse the composites is shown in Figure 3.11(a). The analysis of CTABAu showed that the orientation and positional order of individual NRs is the same (Fig.3.11(b). There is high separation between the adjacent NRs, which resembles a bilayer of the cationic surfactant cetyltrimethyl-ammonium bromide (CTAB). Figure 3.11(d) shows the image for cysteine functionalised Au NRs. From the image, the dispersion of the functionalised nanorods is less than that in the individual nanorods. This confirms that cysteine formed the Au-S bond with gold, producing a self-assembled monolayer. The growth of ZIF-8 crystals progresses with time from cubes exposing 6 {100} faces to intermediate shapes and ultimately to rhombic dodecahedral exposing 12 {110} faces. The dodecahedral shape is the stable equilibrium morphology of ZIF-8. Figure 3.11(c) shows the rhombic dodecahedral shape of the ZIF-8 which has the {110} facets expressed. The crystals did not show any holes meaning there was no Ostwald ripening taking place. The images also show that the particles had good uniformity and well-defined facets. Figure 3.11(e) shows the rhombic dodecahedral structure of ZIF-8 and the encapsulated gold nanorods. Compared to that of ZIF-8 alone, the size of the ZIF-8 became larger and the incorporation of Au NRs did not hinder the shape evolution of the ZIF-8.

3.3.4 X-Ray diffraction studies

X-ray diffraction studies were used to analyse the structure of the synthesised nanomaterials and composites. The XRD patterns of CTABAu nanorods (Fig.3.12 (A)(a)) were analysed in the 2θ range of 35° to 70°. The XRD pattern shows 3 peaks to identify the crystalline gold at 2θ = 37.5, 44.6, 64.7 which represent the crystal planes of (111), (200) and (220) respectively. A face-centered cubic close packing arrangement of the gold nanorods was evident from X-ray diffraction. The peak positions are consistent with metallic gold (Nguyen et al., 2010). Sharp peaks for gold are observed, which indicate the crystalline nature of the product. The lattice constant of the cubic structure was determined from the XRD pattern to be at = 4.079 Å in good agreement with the value of 4.079 Å of the standard diffraction pattern of cubic gold metal (Nguyen et al., 2010). Crystallite size was calculated according to the Debye Scherrer equation with sizes of 219 nm, 82 nm and 98 nm for (111), (200) and (220) planes respectively. Figure 3.12 A(b) shows the XRD patterns of CTABAu-Cys. All the 3 peaks found in CTABAu spectra were observed in CTABAu-Cys but at low intensities. The degree of crystallinity is seen by the intensity of the peaks and the broadening of the peaks

shows a smaller crystallite size. Figure 3.12 B shows the XRD patterns of ZIF-8 in the 2θ range of 5° to 35°.

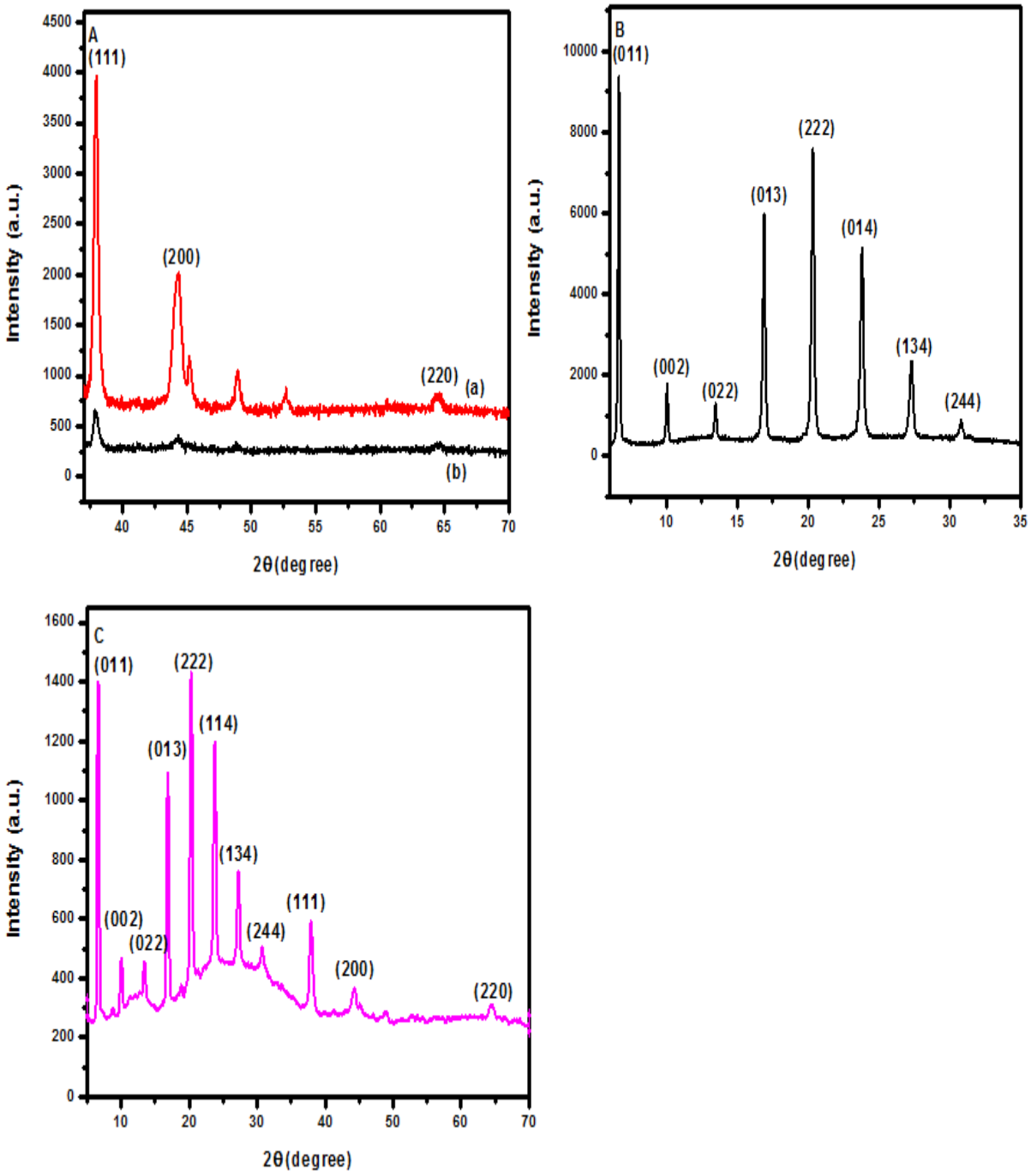

Figure 3.12: (A) XRD spectra of (a) CTABAu and (b) CTABAu-Cys; (B) ZIF-8 and (C) CTABAu-ZIF-8

The peaks at 6.7°, 10.9°, 14.2°, 16.5°,20.1°, 24.4°, 27.7° and 31.6° are represented by (011), (002), (022), (013), (222), (114), (134) and (244) crystal planes respectively. These were consistent with the diffraction patterns observed in literature, confirming ZIF-8

synthesis (Schejn et al., 2015). At the (011) diffraction plane, there was a sharp peak of high intensity showing the high crystallinity of ZIF-8. The diffraction peaks of ZIF-8 crystals and CTABAu were both observed for the CTABAu-ZIF-8 composite in the 2θ range of 5° to 70° in Figure 3.12 C.

Debye Scherrer equation for calculating crystal size:

$$D = \frac{0.94\lambda}{\beta \cos\theta} \quad (3.9)$$

Where D is the average crystallite size, β is the full width at half maximum and θ is the Bragg angle.

The use of cysteine in functionalising Au NRs showed remarkable properties like high fast electron transport, conductivity and surface coverage. As a result, further studies of the thiol to gold interactions were done to analyse the nature of the bonding and to optimise reaction conditions.

3.4 Optimum conditions for thiol to gold interactions

The Au-S bond is highly sensitive to changes in pH, concentration, capping agents and reaction time. Optimum conditions were determined by looking at each parameter and characterization was done using spectroscopic and electrochemical studies.

3.4.1 Effect of CTAB

The effect of the presence of CTAB on the functionalization of Au NRs was shown in Figure 3.13A. The plasmon bands for gold nanorods were previously observed in Figure 3.3. The spectrum for gold nanorods after removal of CTAB (inset (b)) showed a lower intensity longitudinal band.

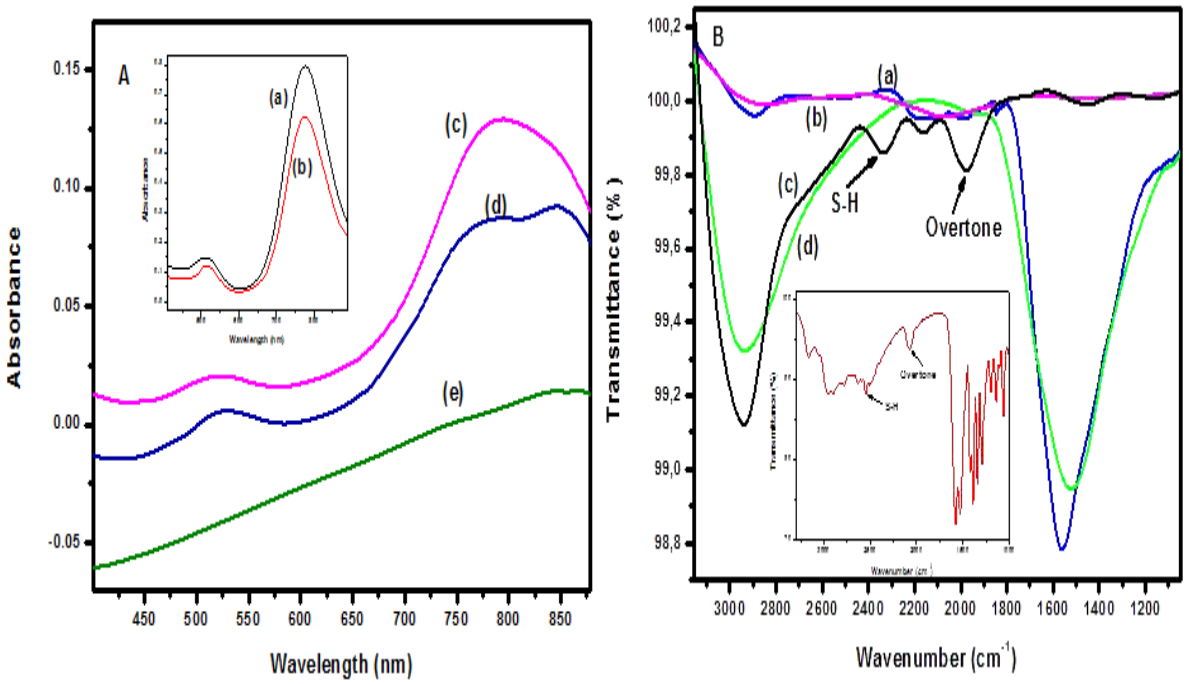

Figure 3.13: (A) UV-Vis absorption spectra of inset: (a) CTABAu, (b) Au; (c) Au-Cys and (d) CTABAu/Cys and (B) FTIR spectra of (a) CTABAu, (b) Au, (c) Au-Cys, (d) CTABAu-Cys and inset: L-cysteine

The addition of L-cysteine to Au NRs without CTAB did not show two distinct bands at higher wavelengths compared to that with Au NRs with CTAB. The CTAB molecules create a hydrophobic microenvironment near the surface of the NRs. In water, the Au NRs have a positively charged surface due to CTA^+ ions strongly absorbed at the side surfaces. This results in electrostatic repulsion between nanorods, which contributes to the stability of the nanorods in solution. FTIR spectroscopy was used to show the effect of CTAB in the composites (Fig 3.13B). The peaks for Au NRs containing CTAB and that for L-cysteine were similarly observed in Figure 3.7. A low intensity peak representing δ(S–H) stretching vibration was observed in Au/Cys with overtones around 1800 cm^{-1} due to the absence of CTAB. This showed that CTAB had a positive effect in assisting with functionalization of Au NRs with cysteine.

3.4.2 Effect of reaction time

The effect of reaction time was seen in Figure 3.14. As the time progressed, the peak at higher wavelengths started developing. The longitudinal band with the lowest intensity and highest intensity of the new plasmon band was seen after 60 minutes.

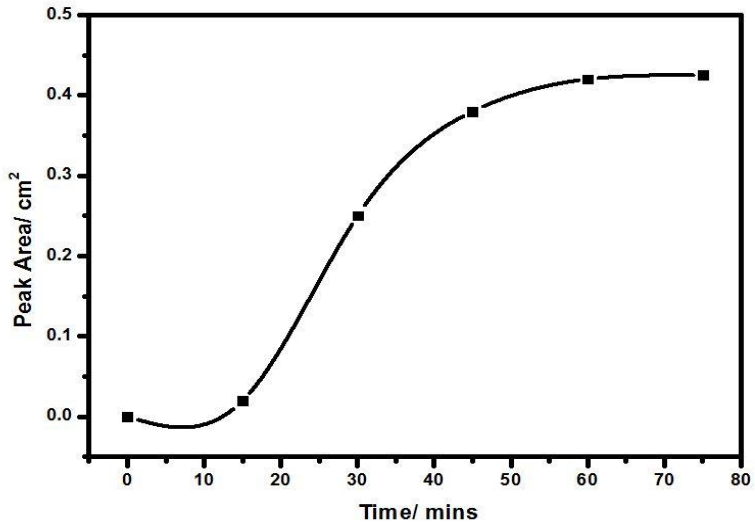

Figure 3.14: Effect of reaction time for CTABAu-Cys at a concentration of 1 x 10^{-11} M and 0.001 M for Au NRs and L-cysteine respectively

Currently, there was more formation of long chains of nanorods. This implies that the addition of L-Cysteine leads to plasmon coupling of longitudinal oscillations due to the end-to-end linking of gold nanorods. The cysteine molecules were bound to the surface of gold nanorods via their thiol groups and at the same time electrostatic interaction between the protonated amino groups and deprotonated carboxylic moiety was also happening.

3.4.3 Effect of the concentration of gold nanorods and L-cysteine

UV-Vis absorption spectra of varying concentration ratios of gold nanorods and L-cysteine were analysed. The gold nanorods to cysteine concentration ratio of 1.0^{8}:1 showed a higher population of end to end linked Au NRs with L-cysteine. The interparticle distance significantly decreased in the aggregates to less than the average rod diameter. Cysteine is a very bulky compound, so when it was adsorbed on the surface, not all the cysteine atoms could interact with surface atoms at the same time and because of high steric hindrances at high concentrations, aggregation was inhibited. At higher ratios, the degree of aggregation was limited.

3.4.4 Effect of volume ratio

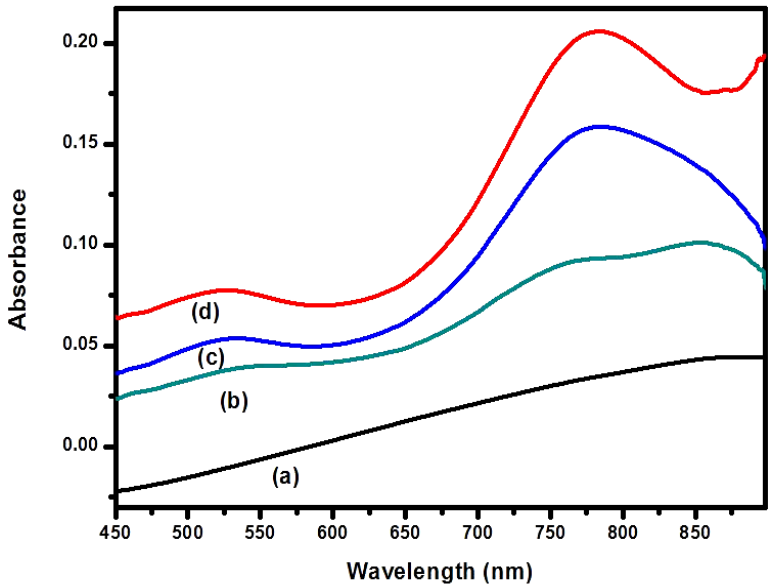

Figure 3.15: UV-Vis absorption spectra of (a) blank, (b) 1:1 (c) 1:3 and (d) 1:5 CTABAu:Cys volume ratios at a 1 hr reaction time and a fixed concentration of 0.001 M and 1 x 10^{-11} M for L-cysteine and Au NRs respectively

The UV-Vis absorption spectra showing varying volume ratios of CTABAu:Cys for CTABAu-Cys composite is shown in Figure 3.15. Broadening of the longitudinal plasmon peak was observed in all peaks. Higher volume ratios did not induce much aggregation due to clumping of particles. As a result, the formation of Au-S complex at higher wavelengths was inhibited. At a 1:1 volume ratio a well-defined plasmon band appeared. The intensity of the longitudinal band is lower than that exhibited by the Au-S complex, indicating a higher population of functionalized gold nanorods.

3.4.5 Effect of pH and temperature

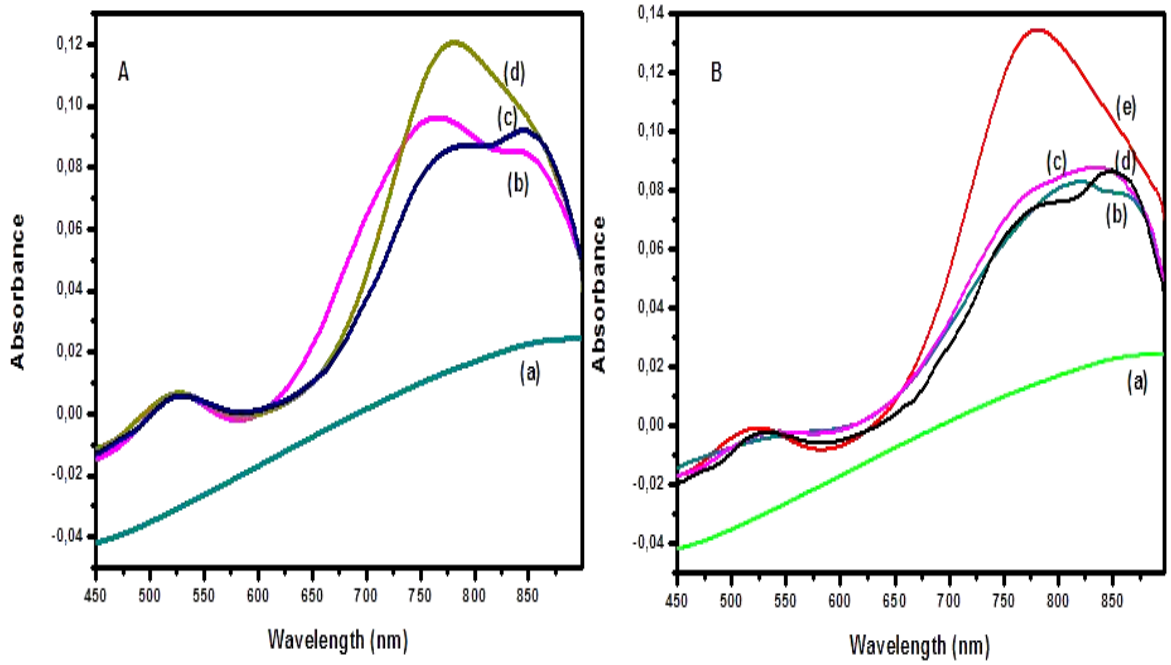

Figure 3.16: UV-Vis absorption spectra (A) showing varying pH with (a) blank, (b) pH 3, (c) pH 6 and (d) pH 9 and (B) depicting changes with temperatures of (a) blank, (b) 15 °C, (c) 20 °C, (d) 25 °C and (e) 30 °C for a 1:1 volume ratio of CTABAu-Cys, 1 hr reaction time, pH 6 and a fixed concentration of 0.001 M and 1 x 10^{-11} M for L-cysteine and Au NRs respectively

The UV-Vis absorption spectra showing the effects of varying pH on the CTABAu-Cys is depicted in Figure 3.16A. All the spectra have the characteristics two peaks for Au nanorods as discussed earlier. The longitudinal band is the most affected, it is broader and wider indicative of more than one compound present. The absorption intensities also vary, pH 6 being the smallest. The acidic solutions; pH's 4 and 6 exhibiting well-defined new plasmon band at 860 nm. The intensity of these plasmon increased for pH 6. Cysteine's structure is affected by changes in hydrogen concentration (Wang & Huang, 2012).The isoelectronic point (pI) for cysteine is 5.07 and the pKa values are 1.96 for the carboxyl group and 8.18 for the ammonium ion. At the isoelectric point, the pH has no net charge. When the pH > pI, the cysteine has a net negative charge. At a close to neutral pH, the aggregation is more pronounced as the net negatively charged cysteine molecule has more stability. Therefore in the acidic medium cysteine carboxylic group's hydrogen are labile thus increasing the interaction with the Au nanorods. In Figure 3.16B, the effect of temperature on CTABAu-Cys is shown. The peak at 25 °C had the highest degree of aggregation with a well-defined new plasmon band at 865 nm. This might have been because of the higher kinetic energy at high temperatures causing more Au NRs to interact with cysteine. At lower and higher temperatures of 15 °C and 30 °C respectively, the molecular assembly of cysteine on gold

surface was distorted. This caused an instability and less Au-S bond formation (Lim et al., 2009).

3.5 Electrochemical characterization

The voltammograms in Figure 3.17 show the effect of pH on a CTABAu/Cys modified electrode. All voltamograms had the characteristic Au nanorods anodic and cathodic peaks except for the pH 6 voltamogramm that had an additional cathodic peak at 0.7 V. The anodic current decrease in the following order pH6>pH9>pH3. The pH's above 6 causes the carboxylic acid groups to deprotonate as there is an increase in the electrostatic repulsive forces which result in an increase in current response.

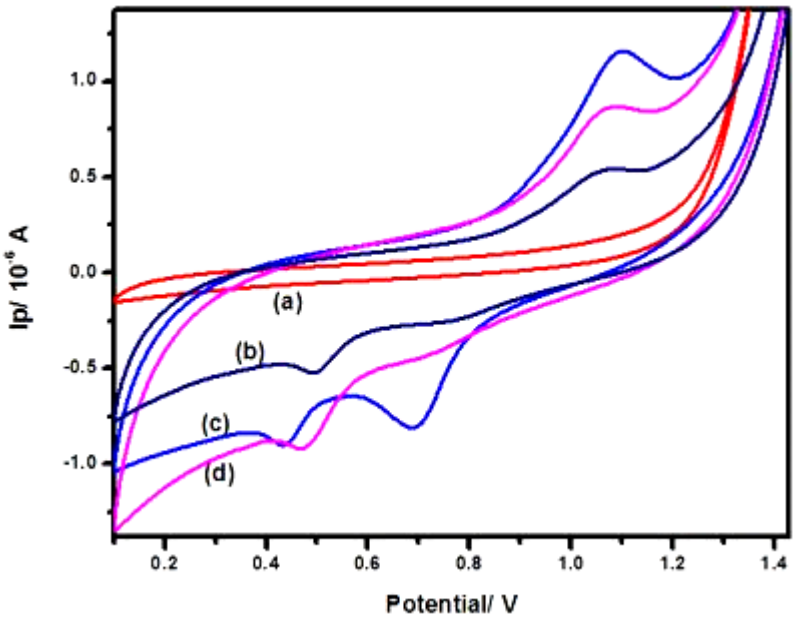

Figure 3.17: CVs for CTABAu/Cys modified electrode showing varying pH with (a) blank, (b) pH 3, (c) pH 6 and (d) pH 9 at a scan rate of 50 mV/s

At a pH of 9, the carboxyl groups in the SAM are fully dissociated. The current response at the electrode will be minimised as the repulsive forces in the SAM are maximised. There is inhibition of the charge transfer when the monolayer is negatively charged. As a result, the extent of inhibition increases as the charge on the SAM carboxyl group increases. Also, the R-SH concentration decreases because of the total deprotonation of the thiol group. This causes minimum support between the bimolecular reaction of $RS^{\bullet}$ and R-SH (Academy &

Prestes, 2017). Ultimately, there is a change in the CV shape as there is a decrease in peak current. At very low pH values the same effect is seen in the instability of the SAM due to the positive repulsive forces of the protonated amino groups.

Alternatively, the two cathodic peaks may result from a mixture of cysteine-Au(0) and cysteine-Au(I). For cysteine functionalised Au NRs, the oxidation states that exist for Au are oxidation states I and 0. The bond between gold and cysteine can either produce a thiol self-assembled monolayer or a Au-S thin film. For a SAM, the thiol is oxidized to a thiyl adsorbed radical, and the metal remains at 0 oxidation state (Au(0)-S•) as the Au d orbitals offers a higher contribution to the Au-S formation. For a Au-S thin film formation, the (Au(I)-S-) bond has a more ionic nature in which the oxidized component is the Au atom. In this case, the Au s orbital is the one with a higher contribution to the Au-S system. The covalent bond Au(0)-thiyl is only seen when there is SAM formation with a stable adsorbed film. The stability of the film comes from the hydrogen bond network created by L-cysteine. This contributes positively to the Au(0)-thyil system as it protects and keeps the surface stable. On the other hand, the Au(I)-thiolate system is exposed as it causes the dissolution of the surface. During the bonding of cysteine, the energetic pathway for a SAM formation is more favorable since the S-H bond of the thiol group is first broken before the formation of the S-Au bond. For ZIF-8 containing composites, the MOF acts as an electron donor to gold nanorods.

3.6 Conclusion

Synthesis of ZIF-8, Au and their composites as well as the cysteine were successfully achieved. The formation of these materials was confirmed by spectra of UV-Vis, FTIR, SEM, XRD and CV voltammograms. The band gaps were studied to analyse conductivity of the platforms, they were in the order CTABAu/Cys > CTABAu/ZIF-8/Cys > CTABAu > CTABAu/ZIF-8. The SEM morphology studies of the synthesised nanomaterial and composites showed the formation of nanorods and rhombic dodecahedral structures for Au and ZIF-8 respectively. Formation of the gold-cysteine composite showed aggregation of particles and that for ZIF-8 showed larger particle size. The suitability for transduction requires the materials to have high conductivity and fast electron transport. This was observed in both cysteine and ZIF-8 containing composites. Further studies of optimising reaction conditions for the synthesis of gold-cysteine composites were undertaken. The optimum reaction conditions for reaction time, volume ratio, temperature and pH were 1 hr, 1:1, 25 °C and pH of 6 respectively.

3.7 References

Abdallah, T., Mohamed, M.B., Abdallah, S., Easawi, K. & Negm, S. 2008. Shape and size dependence of the surface plasmon resonance of gold nanoparticles studied by Photoacoustic technique. *Eur. Phys. J. Special Topics*, 364: 361–364.

Afrasiabi, M., Kianipour, S., Babaei, A., Nasimi, A.A. & Shabanian, M. 2016. ORIGINAL ARTICLE A new sensor based on glassy carbon electrode modified with nanocomposite for simultaneous determination of acetaminophen, ascorbic acid and uric acid. *Journal of Saudi Chemical Society*, 20: S480–S487.

Alaimo, P. J., Bean, J. C., Langenhan, J. M., Nichols, L. 2009. Eliminating Lab Reports: A Rhetorical Approach for Teaching the Scientific Paper in Sophomore Organic Chemistry. *Writing Across Curric. J.*, 20: 17− 32.

Amo-Ochoa, P., Givaja, G. 2007. Microwave assisted hydrothermal synthesis of a novel CuI-sulfate-pyrazineMOF, *Inorganic Chemistry Communications*., 10 (8): 921–927.

Bard, A.J. 1983. Chemical Modification of Electrodes. *J. Chem. Education*, 13(1980): 302–304.

Barke, L.D., Nugeus, P.F. 1997. The Electrochemistry of Gold: I The Redox Behaviour ofthe Metal in Aqueous Media, *Gold Bulletin*, 30 (2): 43-54.

Barus, C., Gros, P., Contat, M. 2007. Electrochemical behaviour of N-acetyl-L-cysteine on gold electrode-A tentative reaction mechanism, *Electrochemica Acta*, 52: 7978-7985.

Batten, S. R., Champness, N. R., Chen, X., Garcia-Martinez, J. 2013. Terminology of metal-organic frameworks and coordination polymers. *Pure Appl. Chem.*, 85 (8): 1715−1724.

Batten, S. R., Champness, N. R.; Chen, X., Kitagawa, S., Ohrstrom, L. 2012. Coordination polymers, metal-organic frameworks and the need for terminology guidelines. *CrystEngComm*.,14 (9):3001− 3004.

Boksebeld, M., Blanchard, N.P., Jaffal, A., Chevolot, Y. & Monnier, V. 2017. Shape-selective purification of gold nanorods with low aspect ratio using a simple centrifugation method. *Gold Bulletin*.

Bonanni, A. & Miyahara, Y. 2011. behavior : an electrochemical impedance spectroscopic and voltammetric study, *Phys. Chem. Chem. Phys.*, 13: 4980–4986.

Bosch, M., Zhang, M., Zhou, H. 2014. Increasing the Stability of Metal−Organic Frameworks. *Adv. Chem*., 182327.

Bredas, J.L., Silbey, R., Boudreux, D.S. and Chance, R.R. 1983. Chain-length dependence of electronic and electrochemical properties of conjugated systems: polyacetylene, polyphenylene, polythiophene, and polypyrrole. *J. Am. Chem. Soc.,* 105 (22): 6555-6559.

Bridges, C., Dicarmine, P.M., Fokina, A. 2013. Synthesis of gold nanotubes with variable wall thickness. *J. Mater. Chem. A*, 1: 1127-1133.

Brust, M., Walker, M., Bethell, W. 1994. Synthesis of thiol-derivatised gold nanoparticles in a two phase liquid system. *J. Chem. Soc*., 801-802.

Castro, L., Blazquez, M. 2011. Biosynthesis of gold nanowires using sugar beet pulp. *Process Biochem*., 46 (5): 1076−1082.

Cavka, J. H., Jakobsen, S., Olsbye, U., Guillou, N., Lamberti, C., Bordiga, S.. Lillerud, K. P. 2008. A New Zirconium Inorganic Building Brick Forming Metal Organic Frameworks with Exceptional Stability. *J. Am. Chem. Soc*., 130: 13850−13851.

Chillawar, R.R., Tadi, K.K. & Motghare, R. V. 2015. Voltammetric Techniques at Chemically Modified Electrodes, *Journal of Analytical Chemistry,* 70 (4): 399-418.

Chow, M., Zukoski, C. 1994. Gold sol formation mechanisms- role for colloidal stability. *J Colloid Interface Sci*., 165: 97.

Cook, T. R., Zheng, Y., Stang, P. J. 2013. Metal-organic Frameworks and Self-assembled Supramolecular Coordination Complexes: Comparing and Contrasting the Design, Synthesis, and Functionality of Metal-Organic Materials. *Chem. Rev*., 113 (1): 734−777.

Das, K., Gogoi, A., Bora, U. 2011. Green synthesis of gold nanoparticles using Nyctanthes arbortristis flower extract. *Bioprocess Biosyst. Eng*., 34 (5): 615−619.

Dauthal, P., Mukhopadhyay, M. 2012. Prunus domesticafruit extract- mediated synthesis of gold nanoparticles and its catalytic activity for 4-nitrophenol reduction. *Ind. Eng. Chem. Res.,* 51 (40): 13014-13020.

Dourado, A.H., Pastrian, F. C., Torresi, S.I. 2018. The long and successful journey of electrochemically active amino acids . From fundamental adsorption studies to potential surface engineering tools. *An. Acad. Bras. Cienc, 12-24.*

Eddaoudi, M., Kim, J., Rosi, N., Vodak, D., Wachter, J., O'Keeffe, M., Yaghi, O. 2002. Systematic design of pore size and functionality in isoreticular MOFs and their application in methane storage. *Science*., 295: 469−472.

Enustun, B., Turkevich, J. 1963. Coagulation of colloidal gold. *J. Am. Chem. Soc*., 85: 3317-3328.

Etesami, M. & Mohamed, N. 2011. Catalytic Application of Gold Nanoparticles Electrodeposited by Fast Scan Cyclic Voltammetry to Glycerol Electrooxidation in Alkaline Electrolyte. *Electrochem. Sci* , 6: 4676–4689.

Faghih, A., Waks, E. 2009. Gold nanowires: Their synthesis and surface plasma resonances*. Am.J. Undergrad. Res*., 8: 25-28.

Faraday, M. 1857. The Bakerian Lecture: Experimentalrelations of gold to light. *Philos. Trans. R. Soc. Lond.*, 147:145-181.

Frens, G. 1973. Controlled nucleation for the regulation of particle size in monodisperse gold suspensions. *Nature: Phys. Sci*., 241: 20-22.

Furukawa, H., Cordova, K. E., O'Keeffe, M., Yaghi, O. M. 2013. The Chemistry and Applications of Metal-Organic Frameworks*. Science*., 341: 1230444.

Ganesh, V., Kumar, S., Gokavarapu, S., Barathy, A. 2011. Facile green synthesis of gold nanoparticles using leaf extract of antidiabetic potent Cassia auriculata*. Colloids Surf. B: Biointerfaces*, 87 (1): 159-163.

Gascon, F. 2010. Synthesis of highly stable UiO-66-NH_2 membranes with high ions rejection for seawater desalination, *Angew. Chem. Int. Ed*., 49: 1530–1532.

Ghule, K. 2006. Microscale size triangular gold prisms synthesized using Bengal gram beans (Cicer arietinum L.) extract and HAuCl4.3.H2O: A green biogenic approach*. J. Nanosci. Nanotechnol*., 6 (12): 3746−3751.

Giersig, M., Mulvaney, P. 1993. Preparation of orderedmonolayers by electrophoretic deposition. *Langmuir*, 9: 3408-3413.

Haram, S.K., Quinn, B.M. & Bard, A.J. 2001. Electrochemistry of CdS Nanoparticles : A Correlation between Optical and Electrochemical Band Gaps. : 8860–8861.

Jana, N., Gearheart, L., Murph, C. 2001. Seed mediated growth approach for shape controlled synthesis of spheroidal and rod like gold nanoparticles using a surfactant template. *Chem. Mater*., 12: 1389- 1392.

Jayaseelan, C., Ramkumar, R., Rahuman, A. 2013. Green synthesis of gold nanoparticles using seed aqueous extract of Abelmoschus esculentus and its antifungal activity. *Ind. Crops Prod*., 45: 423-429.

Jayabal, S., Pandikumar, A., Lim, H.N., Ramaraj, R., Sun, T. & Huang, N.M. 2015. A gold nanorod-based localized surface plasmon resonance platform for the detection of environmentally toxic metal ions. *The Analyst*, 140(8): 2540–2555.

Kang, X.H., Wang, J., Wu, H., Aksay, A.I., Liu, J., Lin, Y.H. 2009. Glucose oxidasegraphene-chitosan modified electrode for direct electrochemistry and glucose sensing. *Biosens. Bioelectron*., 25: 901-905.

Kesarkar, R.N., Sharon, M. & Chowdhary, A. 2015. Simplistic Approach Towards Synthesis of Highly Stable and Biocompatible L-Cysteine Capped Gold Nanosphere Intermediate for Drug Conjugation. *International Journal of Pharmaceutical Sciences Review and Research*, 31(1): 143 - 146.

Kumar, K.V., Paul, W. 2011. Sharma: Green synthesis of gold nanoparticles with Zingiber officinale extract: Characterization and blood compatibility. *Process Biochem.,* 46 (10): 2007-2013.

Laviron, E. 1979. General expression of the linear potential sweep voltammogram in the case of diffusionless electrochemical systems. *J. Electroanal. Chem*., 101: 19-28.

Lim, I.I.S., Mott, D., Engelhard, M.H., Pan, Y., Kamodia, S., Luo, J., Njoki, P.N., Zhou, S., Wang, L. & Zhong, C.J. 2009. Interparticle chiral recognition of enantiomers: A nanoparticle-based regulation strategy. *Analytical Chemistry*, 81(2): 689–698.

Love, J.C., Estroff, L.A., Kriebel, J.K., Nuzzo, R.G. & Whitesides, G.M. 2005. Self-assembled monolayers of thiolates on metals as a form of nanotechnology. *Chemical Reviews*, 105 (4): 1103-1169.

Mendoza, S., Bustos, E., Manríquez, J. & Godínez, L.A. 2015. Voltammetric Techniques. *Agricultural and Food Electroanalysis*: 21–48.

Millner, P.A., Hays, H.C.W., Vakurov, A., Pchelintsev, N.A., Billah, M.M. & Rodgers, M.A. 2009. Seminars in Cell & Developmental Biology Nanostructured transducer surfaces for

electrochemical biosensor construction — Interfacing the sensing component with the electrode. , 20: 34–40.

Murphy, C. 2002. Controlling the aspect ratio of inorganic nanoroods and nanowires. *Adv. Mater*.,14: 80-82.

Narayanan, K., Sakthivel, N. 2010. Phytosynthesis of gold nanoparticles using leaf extract of coleus amboinicus Lour. *Materials Characterization*, 61 (11): 1232-1238.

Neghmouche, N.S. 2007. Analytical Electrochemistry: The Basic Concepts. *Analytical Electrochemistry*, 2: 2–4.

Nguyen, Thien., Tuan, T., Nguyen, N., Van Long, Le. 2010. Synthesis of gold nanoparticles from bulk metallic gold by a sonoelectrochemical method. *Advanced Materials Science and Nanotechnology*, 9:12.

Ni, Z.,Masel, I. 2006. Rapid production of metal −organic frameworks via microwave-assisted solvothermal synthesis, *The Journal of the American Chemical Society*., 128 (38): 12394–12395.

Nie, M., Lu, S., Lei, D., Yang, C. & Zhao, Z. 2017. Rapid Synthesis of ZIF-8 Nanocrystals for Electrochemical Detection of Dopamine. , 164(13): 952–957.

Niidome, Y., Nishioka, K., Kawasaki, H. 2003. Rapid synthesis of gold nanorods by the combination of chemical reduction and photoradiation processes; morphological changes depending on the growing processes. *Chem. Commun*., 2376-2377.

Noruzi, M., Zare, D., Khoshnevisan, D., Davoodi, D. 2011. Rapid green synthesis of gold nanoparticles using Rosa hybrida petal extract at room temperature. *Spectrochim. Actat A: Mol. Biomol. Spectrosc*., 79 (5): 1461-1465.

Park, J. & Kim, M. 2015. Strategies in Protein Immobilization on a Gold Surface., *Applied Science and Conversion Technology, 24(1): 1–8.*

Peeters, K., Wael, K. De, Vincze, L. & Adriaens, A. 2005. Comparison of Different Surface Modification Techniques for Electrodes by Means of Electrochemistry and Micro Synchrotron Radiation X-ray Fluorescence . Dimerization of Cobalt (II) Tetrasulfonated Phthalocyanine and Its Influence on the Electrodeposition on Gold Surfaces. , 77(17): 10725–10732.

Pileni, M.P. 2003. The role of soft colloidal templates in controlling the size and shape of inorganic nanocrystals. *Nat. Mater*., 2:145-150.

Qiu, L., Z. 2008. Facile synthesis of nanocrystals of a microporous metalorganic framework by an ultrasonic method and selective sensing of organoamines*, Chemical Communications*., 31: 3642–3644.

Reddy, V., Torati, R.S. 2013. Biosynthesis of gold nanoparticles assisted by sapindusmukorossi Gaertn. Fruit pericarp and their catalytic application for the reduction of p-nitroaniline. *Ind. Eng.Chem*. *Res*., 52 (2): 556-564.

Rhieu, S.Y. 2015. Tuning the Size of Gold Nanoparticles with Repetitive Oxidation-reduction Cycles. *American Journal of Nanomaterials*,3(1): 15-21.

Schejn, A., Aboulaich, A., Balan, L. 2015. Cu2+-doped zeolitic imidazolate frameworks (ZIF-8): efficient and stable catalysts for cycloadditions and condensation reactions. *Catal. Sci. Technol*,5**:** 1829-1839.

Serre, C., Millange, F., Surblé, S., Férey, G. A. 2004. Route to the Synthesis of Trivalent Transition-Metal Porous Carboxylates with Trimeric Secondary Building Units. *Angew. Chem., Int. Ed.,* 43: 6285−6289.

Shankar, S., Bhargava, S., Sastry, M. 2005. Synthesis ofgold nanospheres and nanotriangles by the turkevich approach. *J. Nanosci. Nanotechnol*., 5 (10): 1721-1727.

Shao, L., Susha, A. 2012. Plasmonic properties of single multispiked gold nanostars: correlating modeling with experiments. *Langmuir.,* 28 (24), 8979-8984.

Shao, Y., Jin, Y. 2004. Dong: Synthesis of gold nanoplates by aspartate reduction of gold chloride. *Chem Commun*., 1104-1105.

Sivaraman, S., Kumar, S., Santhanam, V. 2011. Monodisperse sub-10 nm gold nanoparticles by reversing the order of addition in turkevich method- The role of chloroauric acid. *J. Colloid Interface Sci*., 361 (2): 543-547.

Song, J., Jang, H.K., Kim, S. 2009. Biological synthesis of gold nanoparticles using Magnolia kobus and Diopyros kaki leaf extracts. *Process Biochem*., 44: 1133- 1138.

Tanabe, K. K., Cohen, S. M. 2011. Postsynthetic modification of metalorganic frameworks-a progress report. *Chem. Soc. Rev.*, 40: 498− 519.

Thanh, M.T., Vinh, T., Pham, T., Du, D. & Phi, N. 2018. Iron doped zeolitic imidazolate framework (Fe-ZIF-8): synthesis and photocatalytic degradation of RDB dye in Fe-ZIF-8. *Journal of Porous Materials*, 25(3): 857–869.

Thobhani, S., Attree, S., Boyd, R., Kumarswami, N., Noble, J., Szymanski, M. & Porter, R.A. 2010. Bioconjugation and characterisation of gold colloid-labelled proteins. *Journal of Immunological Methods*, 356(1–2): 60–69.

Turkevich, J., Stevenson, P. 1951. Hillier: A study of the nucleation and growth process in the synthesis of colloidal gold. *Discuss. Faraday Soc*., 11: 55-75.

Vidotti, M., Carvalhal, R.F., Mendes, R.K., Ferreira, D.C.M. & Kubota, L.T. 2011. Biosensors based on gold nanostructures. *Journal of the Brazilian Chemical Society*, 22(1): 3–20.

Wang, J. 2000. Analytical Electrochemistry. 2nd ed., Wiley-VCH, New York.

Wang, L.H. & Huang, W.S. 2012. Electrochemical oxidation of cysteine at a film gold modified carbon fiber microelectrode its application in a flow-through voltammetric sensor. *Sensors*, 12(3): 3562–3577.

Wang, Y., Wang, L., Chen, H., Hu, X. & Ma, S. 2016. Fabrication of Highly Sensitive and Stable Hydroxylamine Electrochemical Sensor Based on Gold Nanoparticles and Metal-Metalloporphyrin Framework Modified Electrode. *ACS Applied Materials and Interfaces*, 8(28): 18173–18181.

Wang, Y., Zhou, X., Xu, C., Jin, Y. & Li, B. 2018. Gold Nanorods as Visual Sensing Platform for Chiral Recognition with Naked Eyes. *Scientific Reports*, 8: 1–9.

Waters, C., Mills, A.J, Johnson, K. 2003. Purification of dodecanethiol derivatized goldnanoparticles. *Chem. Commun*., 540-541.

Watson, K., Zhu, J., Nguyen, S. 1999. Hybrid nanoparticles with block copolymer shell structures. *J. Am. Chem. Soc*., 121: 462-463.

Yonezawa, T., Kunitake, T. 1999. Practical preparation of anionic mercapto ligand stabilized gold nanoparticles and their immobilization. *Colloids Surf. A: Physicochem. Eng. Asp*.,149: 193-199.

Zhou, H. C., Long, J. R., Yaghi, O. M. 2012. Introduction to MetalOrganic Frameworks. *Chem. Rev*., 112: 673−674.

CHAPTER 4

FABRICATION OF THE ELECTROCHEMICAL BIOSENSOR

4.1 Introduction

Electrochemical biosensors offer an effective means to evaluate the components of a biological sample because of the direct conversion of a biological change to an electronic signal (D'Orazio, 2003). Electrochemical biosensors have a challenge regarding lack of surface architectures that permit high enough sensitivity and distinctive identification of the response with the anticipated biochemical change. Factors like pH, temperature, concentration and time affect the response of biosensors such as immunosensors. To fabricate electrochemical biosensors that are efficient, the biomolecular receptor needs to be interfaced with the primary transducer. The definite method used relies on the transducer's tethering layer (Bard, 1983). Dipping the carbon or platinum electrode in a solution results in a layer of water molecules covering its. In some cases, there is an attachment of elements in the solution that are added intentionally or occurring as impurities. The presence of adsorbed species modifies the electrode and may cause a decrease in the current for the electrochemical system. This happens because the adsorbed species may prohibit entrance to the surface of the electrode. Currently, the idea of deliberate modification of an electrode by coating, adsorbing or attachment of specific molecules to the surface has drawn attention to most electrochemists (Millner et al., 2009). Novel and unique properties can be produced from this purposeful and controlled modification of the electrode surface like electrode protection, the retardation or acceleration of electrochemical reaction rates, electro-optical phenomena and improvement of electroanalytical sensitivity. The knowledge of the nature of charge transport processes and charge transfer in thin films has been improved by the crucial studies made on such modified electrodes (Chillawar et al., 2015). Preparation of modified electrodes can happen in several ways like functionalized, polymer-coated and electrostatically-bound electrodes. In most cases, there is high electroactivity of the coating layer or on the electrode as electrons can be exchanged, reduced or oxidized with the underlying substrate material. The electrochemically reactive material is immensely adsorbed onto the electrode surface in a chemisorption process. Chemical reactions can happen to make bonds between a specific molecule and a substrate in covalent attachment. Since its introduction, covalent immobilization by organosilanes has become the most widely used technique for preparing modified electrodes. Polymer layers are made by dipping the electrode into a solution containing a dissolved polymer and allowing the solvent to

evaporate, one forms a thin (0.1-10pm) film on the surface. Polymer layers can also be produced by electrodeposition or by inducing the polymerization of monomers at the electrode surface by electrochemical means (Peeters et al., 2005). After the surface of an electrode has been modified, various electrochemical characterizations are done to find out about the properties and nature of the layer. Therefore, the CV of a monolayer of material will exhibit a peak with an integrated area corresponding to that quantity of material on the surface of the electrode. The peak location on the potential axis is a direct measure of the redox couple on the surface. When it comes to thick layers, the electrochemical signal will exhibit greater integrated areas, corresponding to larger quantities of material on the electrode surface (Afrasiabi et al., 2016).

Even though there have been extensive efforts in immunosensor design, few of them have progressed to commercialization. The most commonly used immunosensor is the one for pregnancy test for the detection of human chorionic gonadotropin (hCG) (Lee *et al.*, 2005**;** Byrne *et al.*, 2009). This is interesting since immunosensors seem to offer unique techniques with elevated specificity, a non-destructive method to sample, simple set-up, straightforward sample preparation and high sensitivity, especially when diverse signal transducers are brought together to yield low limits of detection (Sajid, Kawde and Daud, 2015**;** Di Pasqua *et al.*, 2009). Nonetheless, to attain these features, there are drawbacks which must be addressed because the stability, sensitivity and longevity of an immunosensor on the greater part is hinged on the quantity of immobilized antibody on the surface, lasting activity after the immobilization process, the conformational stability and the alignment on the sensor surface. Certain antibodies are irregular, and their recognition sites alter positions in space after various immobilization procedures. This interrupts the interactions with the analyte (Thobhani *et al.*, 2010**;**Steinitz, 2014).

Various ways have been used to improve antibody binding at the surface. The easiest technique of immobilizing antibodies is via physical adsorption. Traditional immunoassay solid supports such as polystyrene experience physical adsorption via hydrophobic and electrostatic interactions (Makaraviciute and Ramanaviciene, 2013: Lu *et al*., 2012). Even though this method gives the most basic attachment route, it is hard to control and there is random orientation of antibodies during immobilization or denaturation.

The novel transducer designs have improved the abilities of immunoassays by increasing antibody binding capacity and decreasing denaturation at the surface. This has been achieved via covalent attachment. The antibody's functional groups are attached to chemically concocted substrates. Self-assembled monolayers (SAMs) provide another mode of adjusting surface chemistry to encourage antibody adsorption or to make functional

groups for consequent covalent attachment. SAMs are normally produced by molecules that have active functional head-groups at one or the other end of a hydrocarbon chain (Arruebo, Valladares and González-Fernández, 2009**;** Jazayeri *et al.*, 2016).

Exploitation of the gold–thiol interface has been done by applying alkanethiols to offer a linker that can bind gold substrates via the thiol group. Disulfide-bridged cysteines which occur in the hinge region of antibodies, can also be utilized by reducing agents like 2-mercaptoethylamine (2-MEA) to form reactive thiols. The drawback is that, covalent attachment using this procedure can disturb the conformation of the antibody while steric hindrance may hinder antigen binding because the cysteines are internal to the antibody tertiary structure. Utilization of the Au-S bond makes this immobilization approach valuable for gold substrates and nanoparticles in methods like surface plasmon resonance (Lee *et al.*, 2005**;** Lee *et al.*, 2016). In a perfect procedure, antibodies ought to be immobilized in their natural form, without introducing functional groups, in a standardized orientation which make their antigen binding sites free from steric hindrance and produce an orientation that maximizes binding.

A technique that accurately offers the ideal set-up has yet to be realized. Conversely, new developments in the use of metal organic frameworks in bioanalytical applications, provide more efficient control over antibody immobilization and orientation at the interface (Love *et al.*, 2005**;** Tadepalli *et al.*, 2018). MOFs are three dimensional substrates that yield enhanced surface area for antibody binding and they have the ability to minimize steric hindrances that prevent antigen capture (Ricco, 2016). Various materials have been used to make porous three-dimensional substrates, including several polymers, silicon, metals and gels. Orlov *et al*. applied three-dimensional immunochromatographic nitrocellulose membranes saturated with magnetic nanoparticles for use in a strip sensor immunoassay. This provided a solid phase with a great surface area for antibody immobilization. The limit of detection of the sensor was approximately 740 fM. Feng *et al*. used repeat units of Protein A adjacently immobilized via a nickel matrix substrate. The merged proteins could immobilize five antibodies through their Fc regions. A 64-fold increase in antigen detection sensitivity was seen in this three-dimensional protein construct compared to the standard IgG immobilization. MOFs have well-defined pore size which makes them act as molecular sieves (Giménez-Marqués et al., 2016; Liang et al., 2015; Garai et al., 2013). Their mesoporous characteristic helps to facilitate the diffusion of the substrate and product components which result in a good catalytic efficiency of encapsulation (Lei *et al.*, 2014**;** Park and Kim, 2015; Liang et al., 2016).

The various integrations of MOF biocomposites puts them into three categories which are bioconjugation, infiltration, or encapsulation. The covalent binding or adsorption of a biomacromolecule on the outer surface of MOF matrices is known as bioconjugation (Yaghi et al., 2003; Falcaro et al., 2013). The second type of integration is by infiltration of biomolecules into the pore networks of MOFs via noncovalent interactions. The pore size of the MOF is normally larger than the biomacromolecule which hinders the technique to mesoporous MOFs (Horcajada et al., 2012). The third class is because of the assembly of the MOF under biologically attuned reaction conditions in an environment comprising of biomacromolecules. This leads to their encapsulation within the MOF architecture, at the same time preserving the biomolecules' intrinsic functionality (Welch *et al.*, 2017**;** Doonan *et al.*, 2017; Wilmer et al., 2011). Carboxylic acid and amino groups occuring on some MOFs can act as anchoring points for biomacromolecules. Biomacromolecules were covalently bound to MOFs via a DCC-mediated coupling reaction between protein −NH2 and MOF-based −COOH groups by Huang, Lin, and co. Although the amino moiety of the MOF was not directly taking part in the coupling reaction, it improved immobilization via hydrogen bonding interactions. MOF biocomposites can also be synthesized using a cross linking agent called glutaraldehyde (Yim *et al.*, 2017**;** Grieshaber *et al.*, 2008). Other studies utilized glutaraldehyde to immobilize β-glucosidase onto patterned films of a MOF (Doonan et al., 2017). Even though electrochemical approaches have seldom been reported for MOFs due to the insulating properties of the majority of MOFs, the utilization of ZIF-8 in this study offers a promising immobilization platform with enhanced electrochemical response (Falcaro et al 2016; Furukwa et al., 2013). Many sensing concepts and connected devices have been developed over the past decades (Uslu, B and Ozkan, 2007; Uslu, 2004; Hart, 1990). In this chapter various Au nanorods composites platforms potential as transducers are investigated using common traditional electrochemical methods, like cyclic voltammetry (CV), differential pulse voltammetry (DPV) and square wave voltammetry (SWV), were used along with novel approaches. A summary of various applications of MOFs is seen in Table 4.1.

Table 4.1: Selected examples of MOFs for various applications

MOF Formula	Linkage	Application	References
NH2-MIL88B(Cr)	DCC	Proteomics	(Shih et al., 2012)
NH2-MIL53(Al)	Glutaraldehyde	Biocatalysis	(Doherty et al., 2013)
NH2-UiO66(Zr)	Glutaraldehyde	Biocatalysis	(Cao et al., 2016)
HKUST-1	EDC/NHS	Sensing	(Ling et al., 2015)
CTABAu/ZIF-8	Glutaraldehyde	Sensing	This study

4.2 Experimental

4.2.1 Materials and reagents

The nanomaterials and composites for the fabrication of the transducer were used as mentioned in chapter 3. Glutaraldehyde (25 % v/v), anti-EGF antibody and EGF protein were obtained from Sigma Aldrich.

4.2.2 Phosphate buffered saline (PBS) (10x = 0.1M) solution

PBS solution was used as a supporting electrolyte and for solution preparation. About 80 g NaCl and 2 g KCl were dissolved into 800 mL distilled water. Approximately 14.4 g $Na_2HPO_4 \cdot 12H_2O$ and 2.4 g KH_2PO_4 were then dissolved into the solution. The pH was measured and adjusted to the desired value using 1 M HCl and 1 M NaOH solutions followed by making the solution up to 1 litre with distilled water and stored at room temperature.

4.2.3 Synthesis of CTABAu-ZIF-8 composite (Method A)

The synthesis followed the same procedure highlighted in chapter three methodology.

4.2.4 Synthesis of CTABAu-ZIF-8 composite (Method B)

About 50 µl of CTAB capped Au NRs functionalised was added to methanolic ZIF-8 (0.12 mM) for 24 hours.

4.2.5 Instrumentation

Electrochemical measurements (DPV) were carried out using Autolab and a three-electrode compartment system as stated in the previous chapter. The pH meter (HANNA HI2210) was used for measurements and adjustments of buffer pH. UV-visible absorption studies were performed in a Cary 300 dual-beam spectrophotometer using 1 cm quartz cuvette in the wavelength range of 300-900 nm. FTIR measurements were done using Perkin Elmer Spectrum 2 as mentioned in chapter 3.

4.2.6 Electrode preparation and modification

Modified electrodes were made by drop coating nanomaterial and composites as mentioned in the previous chapter. Components of the transducer were varied to obtain the maximum response. The electrodes were left to dry at room temperature before use. Prior to each modification, the GCE electrode was polished repeatedly with 1, 0.3 and 0.05 µm alumina slurries. After each polishing, electrode cleaning adopted was as follows; successive 5 minutes rinsing with doubly distilled water, ultrasonication in ethanol and finally with another doubly distilled water to remove any adsorbed substances on the electrode surface. Activation of the transducer was done with a glutaraldehyde cross linker. The next step was the immobilization of Ab on the GA activated platform. Under the optimized conditions, the fabricated modified electrode response was checked with the immersion of EGF using DPV technique.

4.3 Results and discussion

Electrochemical properties of the modified electrodes were characterised using cyclic voltammetry to fabricate the transducer. The choice of transducer is crucial in the development of a sensitive and selective biosensor.

4.3.1 Electron-transfer kinetic parameters of the composites

The kinetic parameters of the electron-transfer reactions at the electrode surfaces are important to determining fast and slow reactions. The current recorded comes from the determination of the rate of the electrochemical reaction and by the transport of the reacting components to the interface. Laviron's equation (Laviron, 1979) is used to determine the nature of the kinetic parameters by considering changes in scan rates. Scan rates were studied in 0.1 M PBS at modified GCE surfaces as shown (Figure 4.1). For all platforms studied, both anodic and cathodic peak currents were found to be proportional to the scan rate in the range between 20 and 100 mV s^{-1}. The anodic peak potentials (Epa) became slightly more positive whereas the cathodic peak potentials (Epc) became more negative with increasing scan rates. This indicated that the charge transfer rate slowed and that the reversibility of electrochemical redox reaction of the modified electrodes became poor. This kinetic limitation could have been due to: (i) non- equivalent sites present in the film (ii) chemical interactions between the electrolyte ions and the modifier film, (iii) the lateral

interactions of the redox couples present on the surface or (iv) the dominance of electrostatic factors.

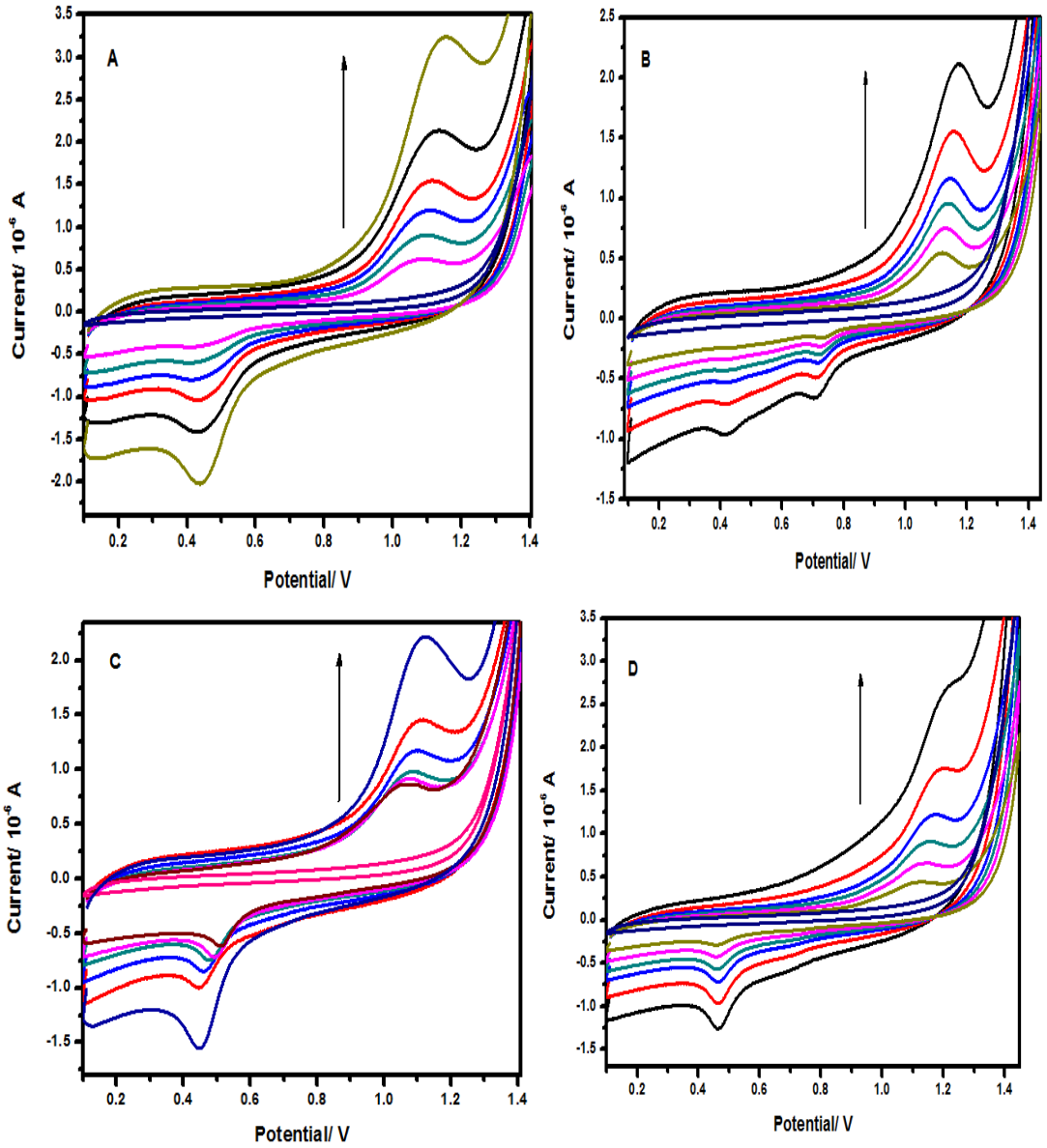

Figure 4.1: CV of varying scan rates of (A) CTABAu, (B) CTABAu/Cys, (C) CTABAu/ZIF-8 and (D) CTABAu/Cys/ZIF-8 at a scan rate of 50 mV/s in 0.1 M PBS

When the potential was scanned at increasing rates from 20 to 100 mV s^{-1} under the same experimental conditions, a linear relationship was observed between the peak current, Ip and both scan rate, v and the square root of v (Figure 4.1 (A) and (B)). After varying the scan rates, the linear relationship between the peak current, Ip and both the scan rate, v and its square root $v^{1/2}$ was analysed. The linear plot analysis shows the type of reaction taking place at the electrode surface. Generally, a linear plot of Ip versus $v^{1/2}$ is obtained when the

electrode process is diffusion controlled, whereas the adsorption-controlled process results in a linear plot of Ip versus v. In this work (Figure 4.1), a mixture of both adsorption and diffusion controlled processes was evident based on the correlation values. However linear plots of Ip versus v gave better correlation coefficient values. This indicated that the surface redox reaction at the modified electrode was an adsorption controlled process.

The relationships of the redox peak potentials with the scan rate were applied to calculate the electrochemical parameters using the following Laviron's equations:

$$Epa = E^0 + \frac{2.3RT}{(1-\alpha)nF} + \log v \quad (4.1)$$

$$Epc = E^0 - \frac{2.3RT}{\alpha nF} + \log v \quad (4.2)$$

$$\log ks = \alpha \log(1-\alpha) + (1-\alpha)\log \alpha - \log\left(\frac{RT}{nF}\right) - (1-\alpha)\,\alpha nF\frac{\Delta Ep}{2.3RT} \quad (4.3)$$

Where Epa and Epc are the anodic and cathodic peak potentials, respectively, α is the electron transfer coefficient, v is the scan rate, R is the universal gas constant (8.314 J mol-1 K-1), T is the absolute temperature (273.15 K), F the Faraday constant (96485 C/mol), E^0 the formal potential, n is the electron transfer number and ks is the standard rate constant of the surface reaction. According to Laviron's equations, the αn value can be calculated from the slope and the E^0 value can be determined from the intercept of Ep vs. v plot. Equation 4.3 for calculating ks is only valid for ΔEp/n > 200 mV and this was the case in the for ΔEp/n values in this study.

Figure 4.2 (C) and (D) shows the linearity of Epa and Epc versus log v respectively. According to equation (4.3), the value of apparent heterogeneous rate constant ks was calculated and found to vary from 0.041 to 0.053 s^{-1}. According to literature, the value for the electron transfer rate constant, ks for bare Au electrode is 0.03 s^{-1} (Cannes et al., 2003). For the modified electrodes, higher ks value were obtained indicating that functionalized gold nanorods provide faster electron transfer at the surface of the electrode. The metal organic framework also showed high reversibility due to its stability on the electrode surface. This shows that the functionalisation of nanoparticles positively influences the surface physicochemistry of the modified electrodes. The CTABAu/Cys modified electrode had the highest ks value showing that cysteine functionalized gold nanorods with CTAB offer faster electron transfer at the surface of the electrode. The electron transfer can happen by tunnelling of electrons through the monolayer, diffusion of the electroactive specie to pinhole or defect sites at the electrode surface or permeation of the redox species into the monolayer. Since the ks values observed were higher than the standard one, the

mechanism was by the tunnelling model. The values of ks in Table 4.2 are within the range of quasi-reversible electron transfer. Table 4.2 shows the results of the electrochemical properties according to equations (4.1-4.6).

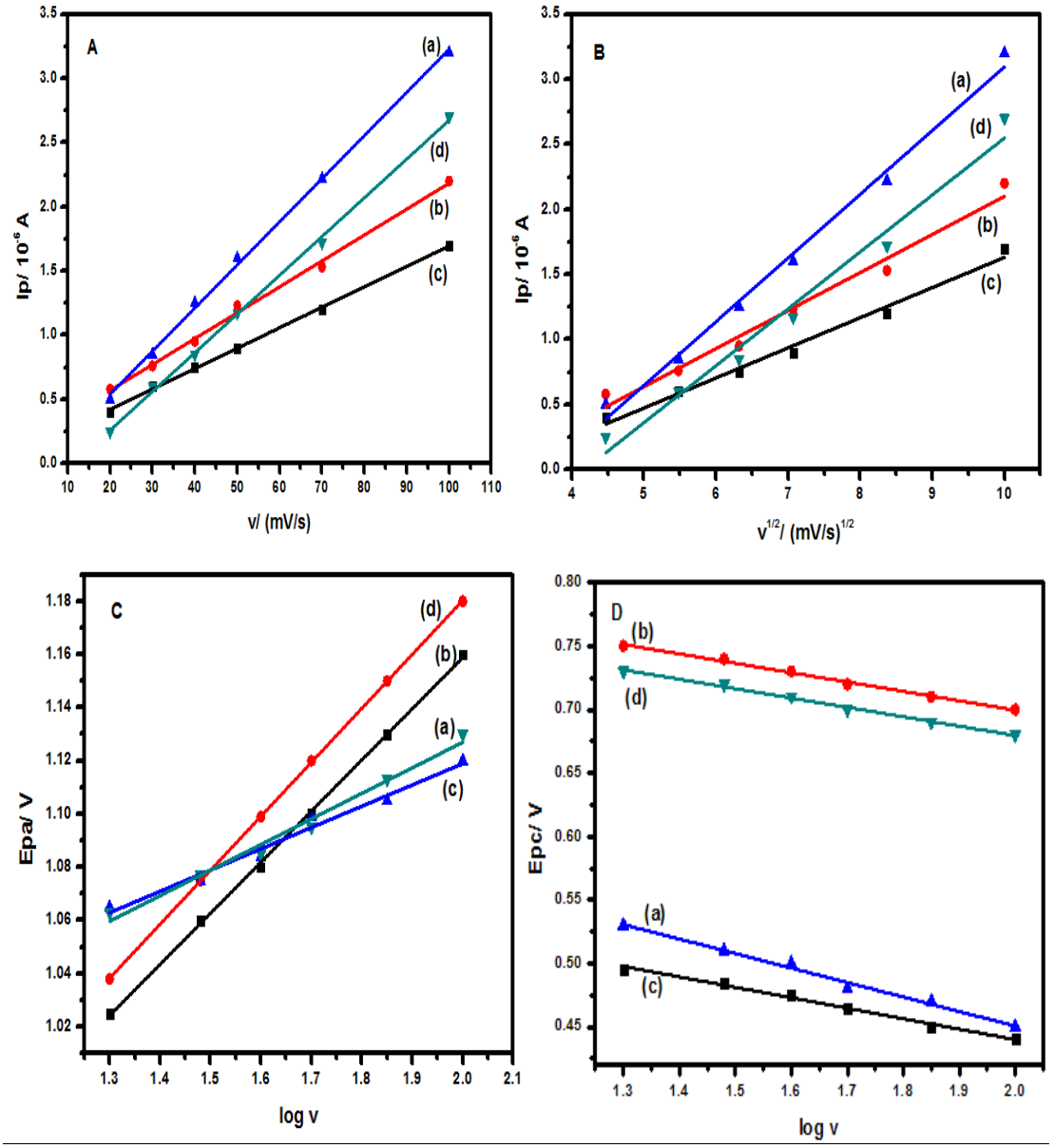

Figure 4.2: The peak current versus (A) scan rate and (B) square root of scan rate and graph of Epa (C) and Epc (D) vs log v for (a) CTABAu, (b) CTABAu/Cys,(c) CTABAu/ZIF-8 and (d) CTABAu/ZIF-8/Cys modified electrodes from a scan rate of 20 to 100 mV/s

Table 4.2 shows the slope of the linear plot of current vs the scan rate and square root of scan rate. The surface coverage of the electrode (Γ) was determined using equation 4.4 in mol/cm^2. Where Q is the charge in coulombs calculated from the integration of the baseline corrected area under the oxidation or reduction peak, F is the Faraday constant (96485

$Cmol^{-1}$), A is the electrode surface area in cm^2 (0.017 cm^2) and n is the number of electrons. The diffusion coefficient (D) was calculated from the slope of the linear plot of Ip vs $v^{1/2}$ according to the Randles-Sevcik equation 4.5.

Table 4.2: Electrochemical properties of modified electrodes based on equations (4.1-4.5)

Parameter	CTABAu	CTABAu/Cys	CTABAu/ZIF-8	CTABAu/ZIF-8/Cys
Γx10^{-7} mol/cm^2	1.020	22.100	0.880	19.400
Q x10^{-6} C	4.000	6.300	3.700	5.900
m Ipa vs. v	0.111	0.043	0.013	0.034
m Ipa vs. $v^{1/2}$	0.233	0.521	0.130	0.394
D x10^{-4} cm^2 s^{-1}	7.170	10.700	5.200	8.600
ks (s^{-1})	0.041	0.060	0.048	0.053
R^2 Ipa vs. v	0.999	0.991	0.992	0.978
R^2 Ipa vs. $v^{1/2}$	0.984	0.983	0.980	0.971

$$\Gamma = \frac{Q}{nFA} \quad (4.4)$$

$$Ip^{quasi} = \pm (2.65\ x\ 10^5) n^{3/2} A C D^{1/2} v^{1/2} \quad (4.5)$$

Where Ip is the peak current, v is the scan rate, C is the concentration (mol/cm^3) and A is the electrode area (cm^2).

In the modified electrode CTABAu/Cys, higher values for surface coverage and charge were found. This increase could have been due to the presence of cysteine facilitating Au-S layer by layer arrangement. As shown in Figure 4.2B, the anodic peak currents were linearly proportional to the square root of scan rate. This gave various values of diffusion coefficient as shown (Table 4.2). The electrochemical properties for cysteine and ZIF-8 containing platforms were better than that for CTABAu modified electrode. Hence, both CTABAu/ZIF-8 and CTABAu/Cys modified electrodes were analysed and the results showed CTABAu/ZIF-8 had the best signal response as highlighted in Figure 4.3.

4.3.2 Optimisation of biosensor fabrication

Figure 4.3 shows the effect of the various fabrication components and techniques used in the development of the biosensor. The composite CTABAu/ZIF-8 in Method A was made using the in-situ synthesis technique and in Method B the ex situ synthesis of CTABAu/ZIF-8 composite was utilised to make the modified electrode CTABAu/ZIF-8/GA/Ab/EGF. The DPV response showed that the CTABAu/ZIF-8 in Method A produced an EGF peak with the modified electrode. This showed that the in-situ synthesis method provided a platform where the Au NRs could be dispersed homogenously in the matrix creating a good spatial distribution for the immobilization of the antibody. For the ex situ synthesis method, there might have been particle agglomeration leading to an irregular structure. The effect of cysteine was observed in the DPV responses of CTABAu/ZIF-8/Cys/GA/Ab/EGF and CTABAu/ZIF-8/GA/Ab/EGF. The peak due to EGF did not appear when cysteine was added to the fabrication. Since cysteine had the NH_2 group also found in the EGF protein, there might have been competition between the NH_2 groups in cysteine and EGF leading to a poor response. The effect of glutaraldehyde was seen on the DPV responses of CTABAu/ZIF-8/GA/Ab/EGF and CTABAu/ZIF-8/Ab/EGF. Glutaraldehyde played a pivotal role in the fabrication process. Firstly, it was used to link the bonding between the antibody and the ZIF-8 providing a stable immobilization platform and secondly this fixative has two reactive aldehyde groups which might attach simultaneously to antibody and EGF thereby binding them firmly together.

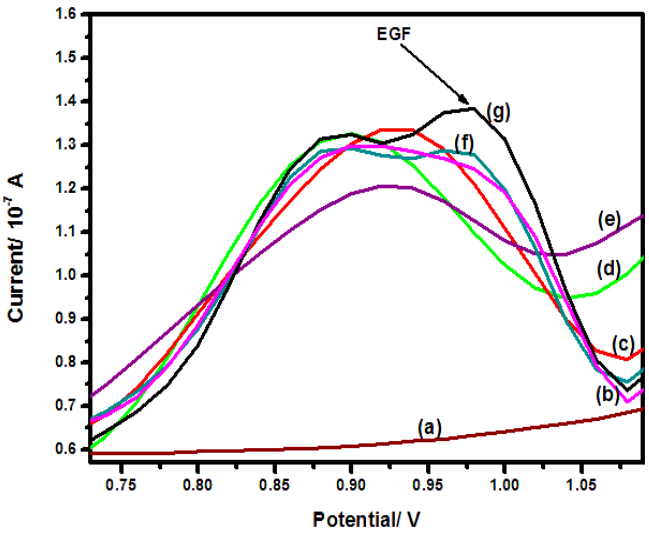

Figure 4.3: DPV responses of (a) blank, (b) CTABAu/ZIF-8/Cys/GA/Ab/EGF, (c) CTABAu/ZIF-8/GA/Ab/EGF, (d) CTABAu/ZIF-8/Ab/EGF, (e) CTABAu/GA/Ab/EGF, (f) Au/ZIF-8/GA/Ab/EGF fabricated using method B and (g) CTABAu/ZIF-8/GA/Ab/EGF (method A) in 0.1 M PBS at a pH of 6

In addition, the antibodies immobilized on the MOF with glutaraldehyde had a more structured orientation. Random orientations might have occurred in the absence of GA which degraded the binding efficiency of the antibodies to analyte. The effect of ZIF-8 in the fabrication process was also observed in the DPV responses of CTABAu/ZIF-8/GA/Ab/EGF and CTABAu/GA/Ab/EGF. The responses show that ZIF-8 was a critical component in the fabrication process as the peak due to EGF was seen. The pores of the MOF increased the contact surface leading to better binding as compared to a flat surface in the absence of ZIF-8. The antibody and MOF coordinated via hydrophobic interactions, provided a sensitive and stable detection mechanism. The effect of CTAB was observed in the DPV responses of CTABAu/ZIF-8/GA/Ab/EGF and Au/ZIF-8/GA/Ab/EGF. Both responses showed a peak due to EGF. However, the one in the presence of CTAB was more resolved. CTAB helped to stabilize the Au NRs during the synthesis technique so that the weak hydrophobic interactions in the framework are not disrupted. The CTAB layer imparts a negative charge onto the colloidal particle surface.

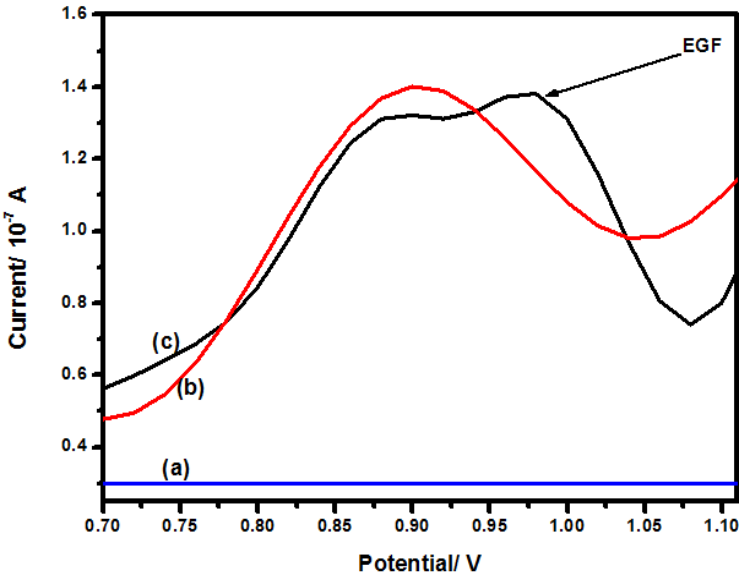

Figure 4.4: The DPV responses for (a) blank and CTABAu/ZIF-8/GA/Ab/EGF prepared using (b) drop coating and (c) immersion techniques

The DPV responses for the two techniques is shown in Figure 4.4. The immersion technique provided a better response compared to the drop coating technique as the peak due to EGF was seen in (b). Binding of EGF to the antibody was more effective when immersed as there was more time for the reaction to take place smoothly. As a result, the immersion method was chosen in the fabrication process.

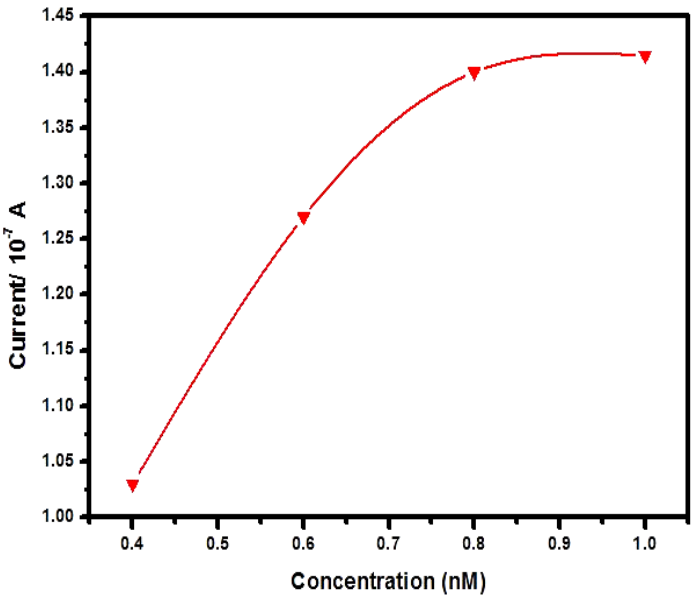

Figure 4.5: Effect of varying concentrations of Au NRs in the CTABAu/ZIF-8 composite

Various concentrations of gold nanorods were analysed against a constant ZIF-8 concentration in Figure 4.5 on the GCE/CTABAu/ZIF-8/GA/Ab/EGF surface. Varying concentrations of 1, 0.8, 0.6 and 0.4 nM for Au NRs were used for the synthesis of the CTABAu-ZIF-8 composite. The graph shows that the current decreased as the concentration of gold nanorods was decreased. The current was optimum at a Au NRs concentration of 1 nM. At lower concentrations, the Au NRs attach on the outer surface of the framework and at higher concentrations gold diffuses into the matrix (Yang, J and Lie, H, 2015).

4.3.3 Effect of GA concentration

The effect of the amount of GA on the performance of biosensor was analysed by using concentrations of 1 and 3 %. The highest peak current was observed at a concentration of 3%. At this concentration the antibody was firmly fixed for effective interaction with EGF.

4.3.4 Effect of Ab concentration

The effect of Ab concentration on the biosensor performance was done using 2 and 5 µg/ml at optimum GA concentration. The highest peak current was observed at a concentration of

2 µg/ml. This might have been due to higher concentrations changing the orientation of the antibody on the ZIF-8 framework and also increasing the steric hindrances. Therefore, a concentration of 2 µg/ml was chosen for the rest of the analysis.

4.3.5 Effect of incubation time

The effect of the incubation time for the various components used was observed in Figure 4.6. The time needed to attach glutaraldehyde on the transducer was optimized using 3 % GA between 0-10 minutes as shown in (Fig.4.6a). The graph shows the increase in peak current until 8 minutes of incubation where it reaches a maximum.

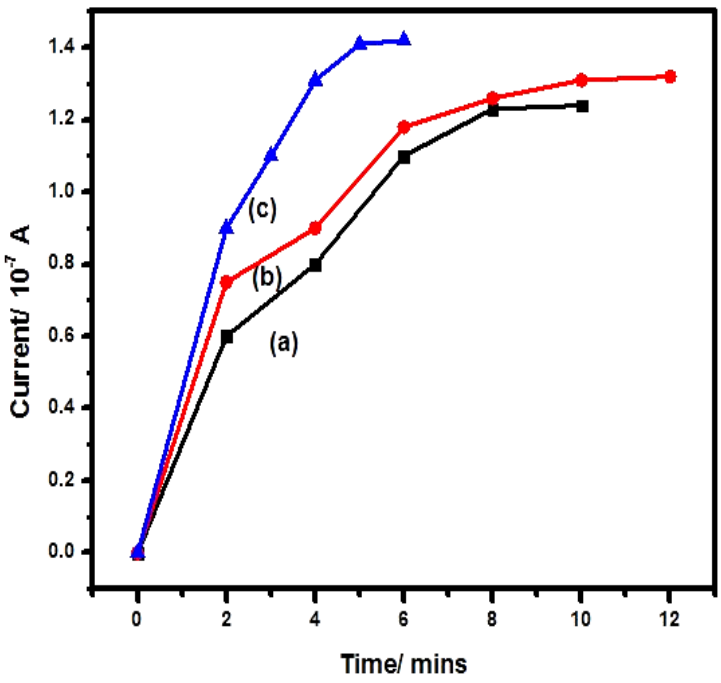

Figure 4.6: Effect of incubation time of (a) GA, (b) Ab and (c) EGF in the development of CTABAu/ZIF/GA/Ab/EGF

At this time, glutaraldehyde was strongly attached to the transducer surface. As a result, 8 minutes incubation time was used for the rest of the analyses. The amount of time required to reach maximum interaction between the antibody and glutaraldehyde was analysed in Figure 6b. The immobilization of Ab on the transducer was achieved under the optimal conditions of glutaraldehyde. The graph shows that as the incubation time increased, the

peak current also increased until a time of 10 minutes after which the current remained constant. Optimum conditions were reached as the aldehyde group of GA fully reacted with the NH_2 group of the antibody, resulting in a firm attachment. The incubation time required for the maximum interaction of EGF with Ab was observed in Figure 4.6c. The peak current increased with an increase in time until 5 minutes, after which the current remained constant. At 5 minutes, the Ab binding sites might have reached saturation with the EGF causing no further increase in current. The biosensor was then developed using the optimum conditions of the individual components.

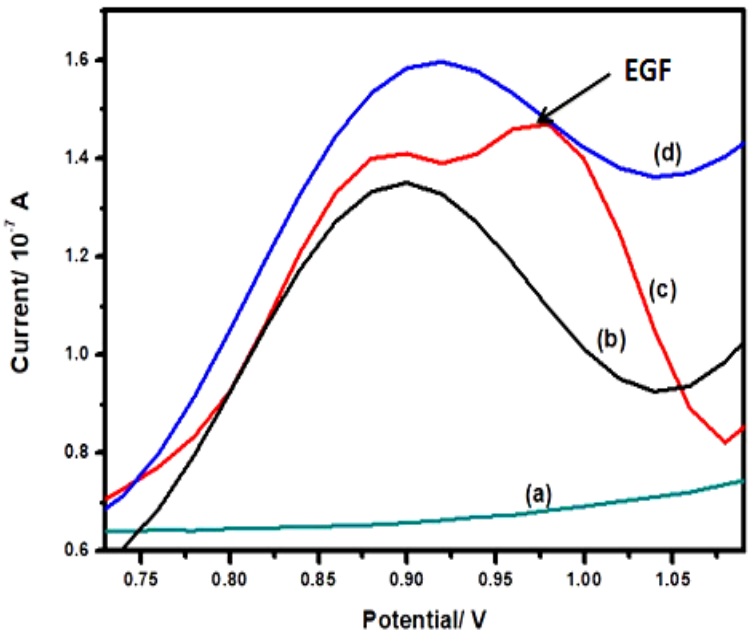

Figure 4.7: The DPV responses for (a) blank, (b) pH 3, (c) pH 6 and (d) pH 9 on the modified electrode with CTABAu/ZIF/GA/Ab/EGF

The effect of pH on the CTABAu/ZIF/GA/Ab/EGF modified electrode was observed in Figure 4.7. Very acidic and alkaline pHs cause the unstable condition of EGF. As a result, a pH of 3 and 9 showed a poor response to EGF. A well-defined peak due to EGF was obtained at a pH of 6. This showed that the degree of protonation of the various side chain groups and the interchain interactions changed with pH. The EGF molecule can be considered as consisting of two domains, an N-terminal domain (l-32) and a C-terminal domain (32-53). There are intimate contacts between these domains, especially between the loop around positions 13-16 and the turnaround positions 40-43. At a pH of 3, the N- terminal strand might have become dissociated from the other strand or a different arrangement of the C-terminal strand

might have occurred. At acidic pHs, the EGF becomes inactive as unfolding, denaturation and aggregation occurs. Since the isoelectric point of EGF is 4.6, at higher pH values of 9, there are large net charges due to increased repulsive forces. This resulted in a pH of 6 exhibiting the best response.

4.3.6 A comprehensive look at the EGF biosensor fabrication process

The biosensor fabrication followed basic fabrication steps, which are summarized in the fabrication process schematics in Figure 4.8A. Cyclic voltammetry was used for monitoring the biosensor fabrication process as shown in Figure 4.8B. This technique allowed for the electronic and analytical analysis of biomaterials deposited on electrode surfaces and the behaviour at the electrode/electrolyte interface. The CVs were recorded at a scan rate of 50 mV/s in PBS at pH 6. The CV of CTABAu/ZIF-8 modified electrode had a sharp oxidation peak with a high Ip of 4.5 µA. Upon addition of glutaraldehyde, the anodic peak became broader with a decrease in peak current. This was due to the presence of the insulating properties of glutaraldehyde on the electrode surface. After immobilization of the antibodies, the modified electrode CTABAu/ZIF-8/GA/Ab clearly showed a different shape with a high decrease in peak current compared to CTABAu/ZIF-8. The insulating nature of large biomolecule antibodies produced a CV curve that was slanted which showed the electrode surface was altered after each step. Human EGF has 11 electrochemically active amino acids like tyrosine, trypthophan, arginine and methionine. The formation of a peak at 1.2 V after addition of the analyte (EGF) indicated the electrochemical signal induced by the specific binding of the antibody to EGF.

The SEM micrograph showing the surface topology of the components used in the fabrication steps is shown in Figure 4.8C. The image shows particles that are closely packed to each other. This showed the successful immobilization of the antibody and the use of the glutaraldehyde cross linker in providing linking sites. In the fabrication mechanism the CTABAu/ZIF-8 composite interacts with glutaraldehyde via hydrogen bonds.

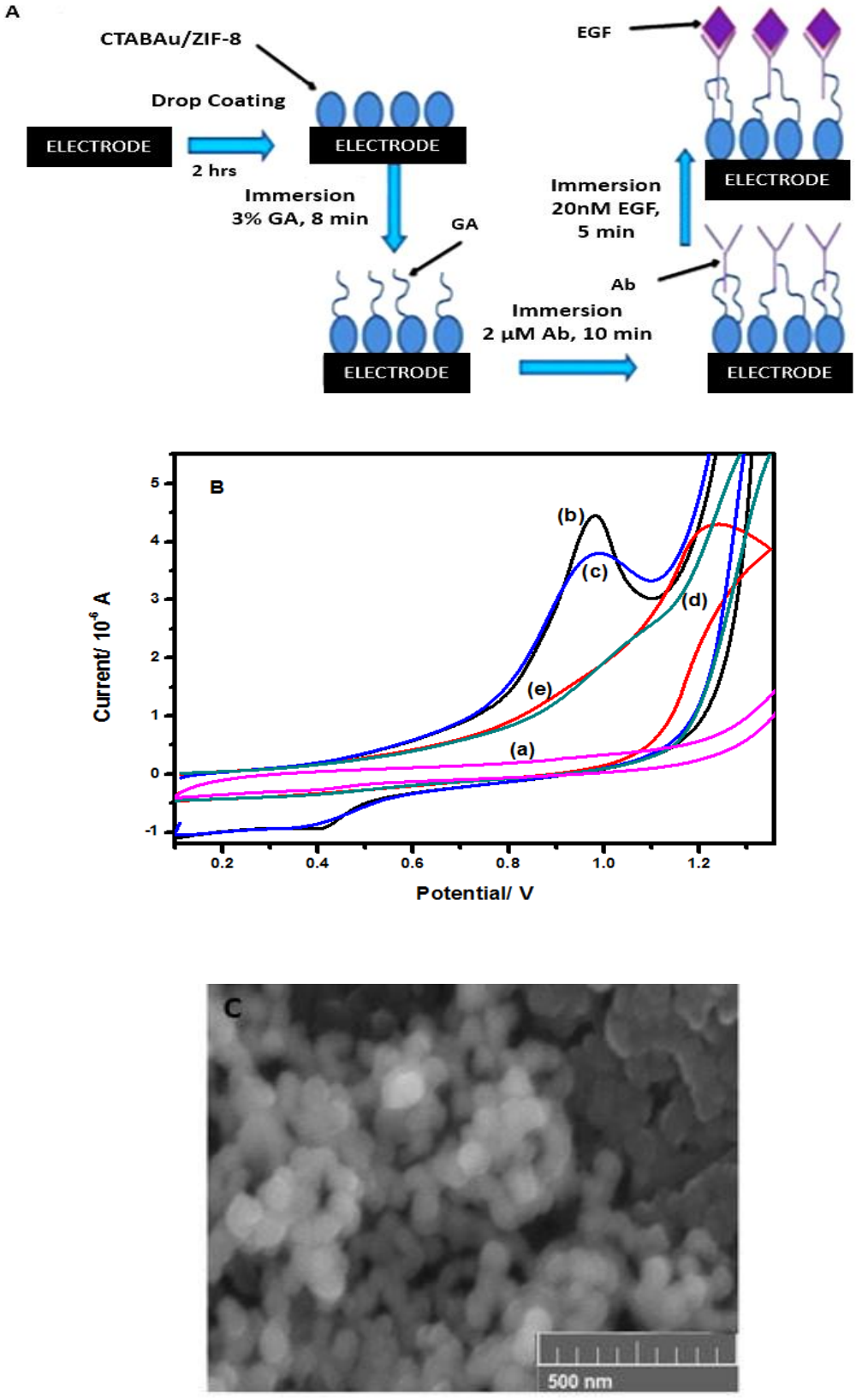

Figure 4.8: (A) mechanism of biosensor fabrication, (B) CVs of (a) blank, (b) CTABAu/ZIF-8, (c) CTABAu/ZIF-8/GA, (d) CTABAu/ZIF-8//GA/Ab and (e) CTABAu/ZIF-8/GA/Ab/EGF in 0.1 M PBS at pH 6 and (C) SEM micrograph of CTABAu/ZIF-8/GA/Ab/EGF on the electrode surface with a magnification of 104 kx

The aldehyde groups interact and form covalent bonds with primary amine groups found in amino acid side chains of the antibody. In this case, the antibody is immobilized and the EGF binds to it producing a signal response.

4.4 Conclusion

Fabrication of the transducer was done by drop coating the nanomaterial and composites on a glassy carbon electrode. Electron transfer kinetic parameters of the platforms was done to assess the surface coverage and electron transfer rate constant. The surface coverage was in the order CTABAu/Cys > CTABAu/ZIF-8/Cys > CTABAu > CTABAu/ZIF-8. The electron transfer rate constant values were in the order CTABAu/Cys > CTABAu/ZIF-8/Cys > CTABAu/ZIF-8 > CTABAu. Higher ks values for the modified electrodes showed the combined effect of cysteine and ZIF-8 offering faster electron transport to the system. The results obtained evidently showed that ZIF-8 and cysteine are critical components for the fabrication of the transducer since they showed properties that can amplify the signal response and boost the sensitivity and selectivity of the biosensor. As a result, both CTABAu/ZIF-8 and CTABAu/Cys platforms were assessed and the results showed CTABAu/ZIF-8 had the best signal response in the biosensor fabrication. The biosensor fabrication steps were first optimised using DPV technique by analysing the fabrication components, coating technique, concentration ratio of CTABAu: ZIF-8, concentration and incubation time of GA, Ab and EGF. The optimum response was obtained using the immersion method at different conditions, GA (3 %; 8 mins), Ab (2 µg/ml; 10 mins) and EGF (5 mins) at a pH of 6. The SEM micrograph of the biosensor fabrication components showed successful immobilization of the antibody as the particles were closely packed.

4.5 References

Bott, A.W. 2001. Electrochemical techniques for the characterization of redox polymers. *Current Separations*., 19(3): 71–75.

Brown, K. & Gray, S. 2010. Cyclic voltammetric studies of electropolymerized films based on ruthenium (II/III) bis (1, 10 phenanthroline) (4-methyl-4'vinyl-2,2'-bipyridine). *International Journal of Chemistry*., 2(2): 3–9.

Brownson, D.A.C. & Banks, C.E. 2014. Interpreting electrochemistry. In Brownson, D.A.C. & Banks, C.E. The Handbook of Graphene Electrochemistry. London: Springer: 23–77.

Cannes, C., Kanoufi, F. & Bard, A.J. 2003. Cyclic voltammetry and scanning electrochemical microscopy of ferrocenemethanol at monolayer and bilayer-modified gold electrodes. *Journal of Electroanalytical Chemistry*, 547(1): 83–91.

Cao, S., Yue, D., Li, X., Li, N., Zong, M. 2016. Novel Nano-/Micro-Biocatalyst: Soybean Epoxide Hydrolase Immobilized on UiO-66-NH 2 MOF for Efficient Biosynthesis of Enantiopure (R)-1, 2-Octanediol in Deep Eutectic Solvents. *ACS Sustainable Chem. Eng*., 4, 3586−3595.

Doherty, C. M., Grenci, G., Riccò, R., Mardel, J. I., Reboul, J. 2013. Combining UV Lithography and an Imprinting Technique for Patterning MetalOrganic Frameworks. *Adv. Mater*., 25, 4701−4705.

D'Orazio P. 2003. Biosensors in clinical chemistry. *Clinica Chimica Acta*., 334(1-2):41–69.

Falcaro, P., Ricco, R., Doherty, C. M., Liang, K., Hill, A. J., Styles, M. J. 2013. MOF Positioning Technology and Device Fabrication, *Chem. Soc. Rev*., 43: 5513– 60.

Falcaro, P.,Ricco, R., Yazdi, A., Imaz, I., Furukawa, S. 2016. Application of Metal and Metal Oxide nanoparticles@MOFs Coord. *Chem. Rev*., 307: 237– 254.

Furukawa, H., Cordova, K. E., O'Keeffe, M., Yaghi, O. M. 2013. The Chemistry and Applications of Metal-Organic Frameworks., *Science*, 341: 1230444.

Garai, A., Shepherd, W., Huo, J., Bradshaw, D. 2013. Biomineral-Inspired Growth of Metal–organic Frameworks in Gelatin Hydrogel Matrices, *J. Mater. Chem. B*., 1: 3678– 3684.

Giménez-Marqués, M., Hidalgo, T., Serre, C., Horcajada, P. 2016. Nanostructured Metal–organic Frameworks and Their Bio-Related Applications Coord. *Chem. Rev*., 307: 342– 360.

Hart, P. 1990. Electroanalysis of Biologically Important Compounds, Ellis Harwood, New York, NY, USA.

Hassan, H.K., Atta, N.F. & Galal, A. 2012. Electropolymerization of aniline over chemically converted graphene-systematic study and effect of dopant. International Journal of Electrochemical Science, 7: 11161–11181.

He, C., Lu, K., Liu, D., Lin, W. 2014. Nanoscale Metal–Organic Frameworks for the Co-Delivery of Cisplatin and Pooled siRNAs to Enhance Therapeutic Efficacy in Drug-Resistant Ovarian Cancer Cells, *J. Am. Chem. Soc.*, 136: 5181– 5184.

He, Y., Wang, Y. 2016. Metal Organic Frameworks Combining CoFe2O4 Magnetic Nanoparticles as Highly Efficient SERS Sensing Platform for Ultrasensitive Detection of N-Terminal Pro-Brain Natriuretic Peptide., *Appl. Mater. Interfaces.*, 8: 7683– 7690.

Horcajada, P., Gref, R., Baati, T., Allan, P. K., Maurin, G., Couvreur, P., Férey, G., Morris, R. E., Serre, C. 2012. Metal–Organic Frameworks in Biomedicine, *Chem. Rev.*, 112: 1232–1268.

Kellner, R. 2004. Analytical Chemistry: A Modern Approach to Analytical Science, Wiley-VCH, Weinheim, Germany, 2nd edition.

Liang, K., Carbonell, C., Styles, M. J., Ricco, R., Cui, J.; Richardson, J. J., Maspoch, D., Caruso, F., Falcaro, P. 2015. Biomimetic Replication of Microscopic Metal–Organic Framework Patterns Using Printed Protein Patterns, *Adv. Mater*., 27: 7293– 7298.

Liang, K., Ricco, R., Doherty, C. M., Styles, M. J., Bell, S., Kirby, N., Mudie, S., Haylock, D., Hill, A. J., Doonan, C. J., Falcaro, P. 2015. Biomimetic Mineralization of Metal-Organic Frameworks as Protective Coatings for Biomacromolecules, *Nat. Commun*., 6: 7240.

Liang, K., Richardson, J. J., Cui, J. 2016. Metal-Organic Framework Coatings as Cytoprotective Exoskeletons for Living Cells, *Adv. Mater*., 28: 7910– 7914.

Ling, P., Lei, J., Zhang, L., Ju, H. 2015. Porphyrin-Encapsulated Metal−Organic Frameworks as Mimetic Catalysts for Electrochemical DNA Sensing via Allosteric Switch of Hairpin DNA. *Anal. Chem*., 87, 3957−3963.

Liu, J., Zhang, Y., Chen, X., Wang, H. 2014. Graphene Oxide–Rare Earth Metal–Organic Framework Composites for the Selective Isolation of Hemoglobin, *Appl. Mater. Interfaces.,* 6: 10196– 10204.

Lyu, F., Zhang, Y., Zare, R. N., Ge, J., Liu, Z. 2014. One-Pot Synthesis of Protein-Embedded Metal–Organic Frameworks with Enhanced Biological Activities, *Nano Lett.*, 14: 5761– 5765.

Monk, P.M. 2001. Fundamentals of electroanalytical chemistry. Chichester, New York: John Wiley & Sons Ltd.

Orlov, A. V., Bragina, V. A., Nikitin, M. P. 2016. Rapid Dry-Reagent Immunomagnetic Biosensing Platform Based On Volumetric Detection of Nanoparticles On 3D Structures . B*iosens bioelectron*., 79: 423–429.

Ricco, R. 2016. Emerging Applications of Metal–organic Frameworks, *Cryst. Eng. Comm*, 18: 6532– 6542.

Schoning M.J., Poghossian A. 2002. Recent advances in biologically sensitive field-effect transistors (biofets), *Analyst*.,127(9):1137–1151.

Shih, Y., Lo, S., Yang, N., Cheng, Y., Wu, C., Huang, H., Lin, C. H. 2012. Trypsin-Immobilized Metal-Organic Framework as a Biocatalyst In Proteomics Analysis*. ChemPlusChem*., 77, 982−986.

Uslu, B. 2004. Anodic voltammetry of abacavir and its determination in pharmaceuticals and biological fluids, *Electrochimica Acta*, 49 (25): 4321–4329.

Uslu, B., Ozkan, S. 2007. Solid electrodes in electroanalytical chemistry: present applications and prospects for high throughput screening of drug compounds, Combinatorial Chemistry and High Throughput Screening, 10 (7): 495–513.

Wang, C., Feng, B. 2015. Research progress on site-oriented and three-dimensional immobilization of protein, *Mol. Biol*., 49 (1): 1-20.

Wilmer, C. E., Leaf, M., Lee, C. Y., Farha, O. K., Hauser, B. G., Hupp, J. T., Snurr, R. Q. 2011. Large-Scale Screening of Hypothetical Metal–organic Frameworks, *Nat. Chem.*, 4: 83– 89.

Yaghi, O. M., O'Keeffe, M., Ockwig, N. W., Chae, H. K., Eddaoudi, M., Kim, J. 2003. Reticular Synthesis and the Design of New Materials. *Nature*, 423: 705– 714.

Ye, T., Liu, Y. 2014. Metal–organic Framework-Based Molecular Beacons for Multiplexed DNA Detection by Synchronous Fluorescence Analysis, *Analyst.*,139: 1721.

CHAPTER FIVE

DETECTION OF EGF

5.1 Introduction

The goal of every analytical method is to produce qualitative and quantitative results with a satisfactory uncertainty level. Detection of analyte is influenced by various factors which includes electroanalytical technique (Moressi et al., 1994; Long et al., 2008; Mabott et al., 1983). Cyclic voltammetry has developed to be a crucial and extensively utilized method in various fields of chemistry for analysing electroanalytical parameters (Li et al, 2014; Lin et al., 2015; Rock et al., 1966). Besides it being used for quantitative purposes, it can be used for showing reaction products stability, evaluating intermediate reactions and analysing redox procedures. (Beiginejad et al., 2013; Van Benschoten et al., 1983). This method is centred on maintaining the current at a specific scan rate whilst the applied potential at the working electrode in both directions is altered (Lim et al., 1972; Kissinger et al., 1983). For a higher speed and sensitivity to be achieved, there have been developments to apply potential modulation of various types rather than the usual staircase ramp. Differential pulse voltammetry is one of the pulse methods that can be applied. The DPV method is analogous to normal pulse voltammetry as the potential is scanned with consecutive pulses. The only difference is that there is a pulse at a specific potential of little amplitude, which is overlaid on a base potential that is changing gradually (Baars, 1994; Bard, 1980). Each pulse measures current at two places. The first place is measured at the time before the pulse is applied and the other when the pulse ends. Decay of non-faradaic current is permitted because of the selected sampling points. The plot consists of the variation between the current readings at every pulse against the base potential (Bersier, 1987; Brett 1993). The other technique, SWV, comprises of a regular square wave pulse with an amplitude E_{sw} that acts as an excitation signal. The staircase waveform with a step height ΔE and the excitation signal are overlaid on each other. (Kounaves, 1987). At this point, the staircase waveform and the square wave pulse going forward overlaps. The discrepancy between the forward and backward currents gives the net current and this is centred on the potential of the redox reaction (O'dea et al., 1981). The height of the peak and the electroactive species concentration are directly proportional and direct detection limits as low as 10^{-8} M are attainable. The benefits of using the SWV technique include high sensitivity (limits of detection as low as 10^{-8} M), speed and background currents are eliminated (Osteryoung, 1985). The speed, together with computer control and signal averaging, gives room for

experiments to be performed repetitively and increases the signal to-noise ratio (Mendoza et al., 2015; Saadati et al., 2013; Nicholson et al., 1964; Rudolph, 1984).

Analytical processes are comprised of various technical operating parameters, like accuracy, precision, bias, percent recovery and dynamic linear range. Another critical parameter is the limit of detection (LOD) (Armbruster, 1994). There has often been various disagreements within the clinical laboratory field regarding the terminology which best suits the description of this parameter. Similarly, there have been different ways of estimating it. The National Committee for Clinical Laboratory Standards (NCCLS) describes the LOD as the smallest concentration or amount of an analyte that can be reliably shown to be present or measured under defined conditions. Below the LOD, the results are not able to meet these criteria as the analysis will not be feasible (Armbruster, 2008). Two methods have been widely used to calculate this parameter, a statistical approach and an empirical one. In the first method, various blank samples are put to test and the mean blank value and the SD are determined. Technique is simple and fast. The LOD will be the mean blank value plus 2 or 3 SDs. Discrepancies of this method use the mean plus 3, 4, or even more SDs to offer a more comprehensive LOD (Carpenter et al., 1975). The justification is that the SD for the blank sample is almost the same as the SD and small concentrations of analyte essentially correspond to the LOD. So if the analyte is existing, it will yield a signal greater than the analytical noise in the absence of analyte (Şengül et al., 2016). The LOD should always be statistically discrete from a blank 95-99% of the time. The disadvantage of this method is that there is no objective evidence to verify that a low concentration of analyte will definitely produce a signal distinct from a blank (zero concentration) sample (Ismail et al., 2014). The second method makes use of analysing samples which contain small but known concentrations of the substance of interest. The benefit of this empirical method is that objective data is used to relate with the analytical response of blank and low concentration samples to decisively conclude what concentration of analyte is needed to differentiate its presence from its absence. The limit of quantitation (LOQ) is usually at a higher concentration than the LOD. When using the statistical method, it is 10 SD above the mean blank value, therefore presenting a greater possibility that a value at the LOQ is real and is not just an unsystematic fluctuation of the blank reading. The LOQ may be the same as the LOD or it could be at a much higher concentration. It cannot be lower than the LOD (Lee et al., 2004).

A specific calibration curve should be plotted using samples containing an analyte in the range of LOD or LOQ. The residual standard deviation of a regression line or the standard error of the *y*-intercept may be used as the standard deviation. In this study, LOD and LOQ

values were calculated by the standard deviation of y-intercepts using the following equations:

$$\text{LOD} = \frac{3\sigma}{m} \quad (5.1)$$

$$\text{LOQ} = \frac{10\sigma}{m} \quad (5.2)$$

Where σ = standard error of y-intercept and *s* = the slope of the calibration curve

Another factor which influences EGF detection is the matrix interferences**.** In contrast to blood which has ways to keep the internal environment homeostatic, urine is more likely to show changes that happen in the body (Armbruster et al., 2008). This is why in most cases of biosensor applications, urine is prospectively a better biomarker source than blood. On the other hand, the inconsistency of urine matrix components such as organic compounds, pH and electrolytes can hinder antibody binding and assay performance. As a result, careful evaluation of these effects is necessary if urinary samples are used for biomarker applications. In this study, we evaluated the effects of two potential matrix interferences which is glucose and creatine. The collective effect of the components of the sample other than the analyte on the measurement can either suppress or enhance the response of analytes. Matrix Interferences can induce false positives in analytical responses by inhibiting analyte activity and antibody to analyte binding. Dilution with solvent is a preferred strategy to reduce or eradicate matrix effects, but this process can also reduce the quantifiable sensitivity. This method works well with immunoassays showing very high sensitivity able tolerate the dilution factors and still maintain the detection limit at permissible requirements (Bienvenu et al., 2017). Nevertheless, a common error which results in an immunoassay is dilution error if the dilution factor is too much. Interferences in the form of solid particles can easily be removed by centrifugation or filtration and many sample preparation procedures have combined one of these procedures to remove the interferences.

The consistency of analytical findings is an issue of paramount importance in clinical toxicology, as it is the backbone of correct interpretation of toxicological findings. It is crucial to apply well-defined and thoroughly validated bioanalytical methods to yield reliable results

that can be adequately interpreted. Some of the methods that are used for EGF detection are summarised in Table 5.1.

Table 5.1: Comparison of major characteristics of other methods for the determination of EGF

Method	Linear range (nM)	LOD (nM)	Reference
Radiolabeled Receptor Assay	1-100	0.5	(Carpenter et al.,2015)
Solid-phase radioimmunoassay	2-300	2	(Vazquez & Freyre, 1990)
HPLC	50-10^4	50	(Lee et al., 2001)

One of these factors that show reliability of an analytical procedure is linearity. Linearity evaluates the ability of the technique to obtain test results that are directly proportional to the concentration of the analyte in the sample. The linear range of the procedure must always be determined regardless of the phase of method development. The International Council for Harmonisation guidelines recommend assessing a minimum of five concentrations to measure linearity. The five concentration levels should cover the upper and lower concentration levels determined during the accuracy study. Another critical factor is the calibration model. The choice of a suitable calibration model is required for a dependable quantification. Hence, the connection between the concentration of analyte in the sample and the accompanying detector response must be examined (Taylor et al., 2012). One of the ways to examine this is by analyzing spiked calibration samples and plotting the resulting responses versus the corresponding concentrations. The resulting standard curves can then be further assessed by graphical or mathematical approaches, the latter also permitting statistical calculation of the response functions. Although there is a universal agreement that calibration samples should be made in blank matrix and that their concentrations must bracket the whole calibration range, references on how many concentration levels required and their replicates per concentration level differ considerably (Tian et al., 2016). Under normal circumstances, at least five to eight concentration levels should be studied for linear relationships and it can be even more for nonlinear relationships (Daksh et al., 2015). The precision under the same operating condition over a short interval of time displays the repeatability. It is also called intra-assay precision. At least six replicate sample preparation homogenous sample is prepared at 100% test concentration. The precision of a method within variations in the laboratory or different days, analysts and equipments is called reproducibility (Chou et al., 1997). Each testing site can make a total of six sample preparations according to the analytical method. Results are assessed to ensure statistical

equivalence among various testing sites. All these parameters were analysed in the detection of EGF in order to produce reliable results.

5.2 Experimental

5.2.1 Materials, reagents and Instrumentation

EGF, Anti-EGF antibody and glutaraldehyde were obtained from Sigma Aldrich as mentioned in the previous chapter. Glucose and creatine were also purchased from Sigma Aldrich. Electrochemical measurements were done using Autolab PGSTAT 101 (Metrohm, SA). A conventional three-electrode system consisting of glassy carbon electrode (GCE) was used as the working electrode (A = 0.071 cm^2). A platinum wire (3 mm diameter) from Metrohm SA and Ag/AgCl (3 M KCl) electrodes from BAS were used as auxiliary and reference electrodes respectively. All measurements were recorded with respect to Ag/AgCl reference electrode. Stock solutions of EGF were prepared in PBS. All the stock solutions were kept in the refrigerator. The working solutions of EGF were freshly diluted from their stocks.

5.2.2 Optimization of the procedures for EGF detection

The preparation and modification of the transducer used in analysis was done as detailed in chapter 4 section 4.2.6. Factors influencing its conductivity were considered, optimised and discussed in Chapter 4 and the optimum conditions used were in situ fabrication for gold-ZIF-8 composite, drop coating technique at a pH of 6.

- *Electrochemical technique, pulse amplitude, step potential and starting potential*

The optimally fabricated transducer and sensor CTABAu/ZIF-8/GA/Ab/EGF performance was optimised by determining the best method as well as optimum conditions for running the techniques. Optimisation was achieved by detecting EGF applying the same variable, concentration and varying only the parameter being optimised. Optimisation involved choice of the method of detection from CV, SWV and DPV. Experimental factors that influences the performance of the DPV technique pulse amplitude, step potential and starting potential were optimised by varying instrument setting for each from 10-100 mV, 10-50 mV and 0.2-0.7 V respectively. All analysis were done at an EGF concentration of 40 nM, with a GC working electrode, Pt wire auxiliary electrode and silver/silver chloride (Ag/AgCl, 3 M KCl) reference electrode for electrochemical determinations at a pH of 6 in 0.1 M PBS.

5.2.3 Reproducibility, repeatability, stability and matrix interferences

The ability of the biosensor to reproduce the same signal on repetitive measurements was evaluated using 40 nM EGF at a pH of 6 in 0.1 M PBS solutions utilising the DPV technique. Repeatability was done using 5 replicate measurements with the same modified electrode. Stability of the biosensor was studied by the measurement of current signal of the modified electrodes at intervals of three days for a period of 15 days (3, 6, 9, 12 and 15 days). Each measurement was done in three replicates. Under optimized conditions, the influence of different interferences on the detection of EGF was investigated within the DPV response using glucose and creatine. Various concentration ratios of inteferent with EGF (1:5; 1:1; 5-1) were prepared and checked for possible interference. The functionality of the biosensor was analysed through spiking and recoveries of the EGF in urine and milk. The samples were spiked with 10 ng/ml and 2 ng/ml of diluted urine and saliva respectively and differential pulse voltammograms were recorded.

5.3 Results and discussion

The biosensor optimization is a critical step to ensure accurate and reproducible performance. It also ensures that the biosensor properties are known and can be controlled to ensure the integrity of the analysis carried out using the method. Therefore, parameters which have a huge influence on the viability of the technique were assessed.

5.3.1 Optimization parameters for EGF detection method

5.3.1.1 Electrochemical technique for the detection of EGF

Figure 5.1 shows the various techniques' voltammetry responses. The response for CV (Fig.5.1A) shows a very low-intensity broad peak which is not well resolved and with irregular current increase. The SWV (Fig.5.1C) response shows a peak which increases in current as concentration increases, however the response from DPV (Fig.5.1B) shows more resolved peaks with higher peak current compared to SWV.

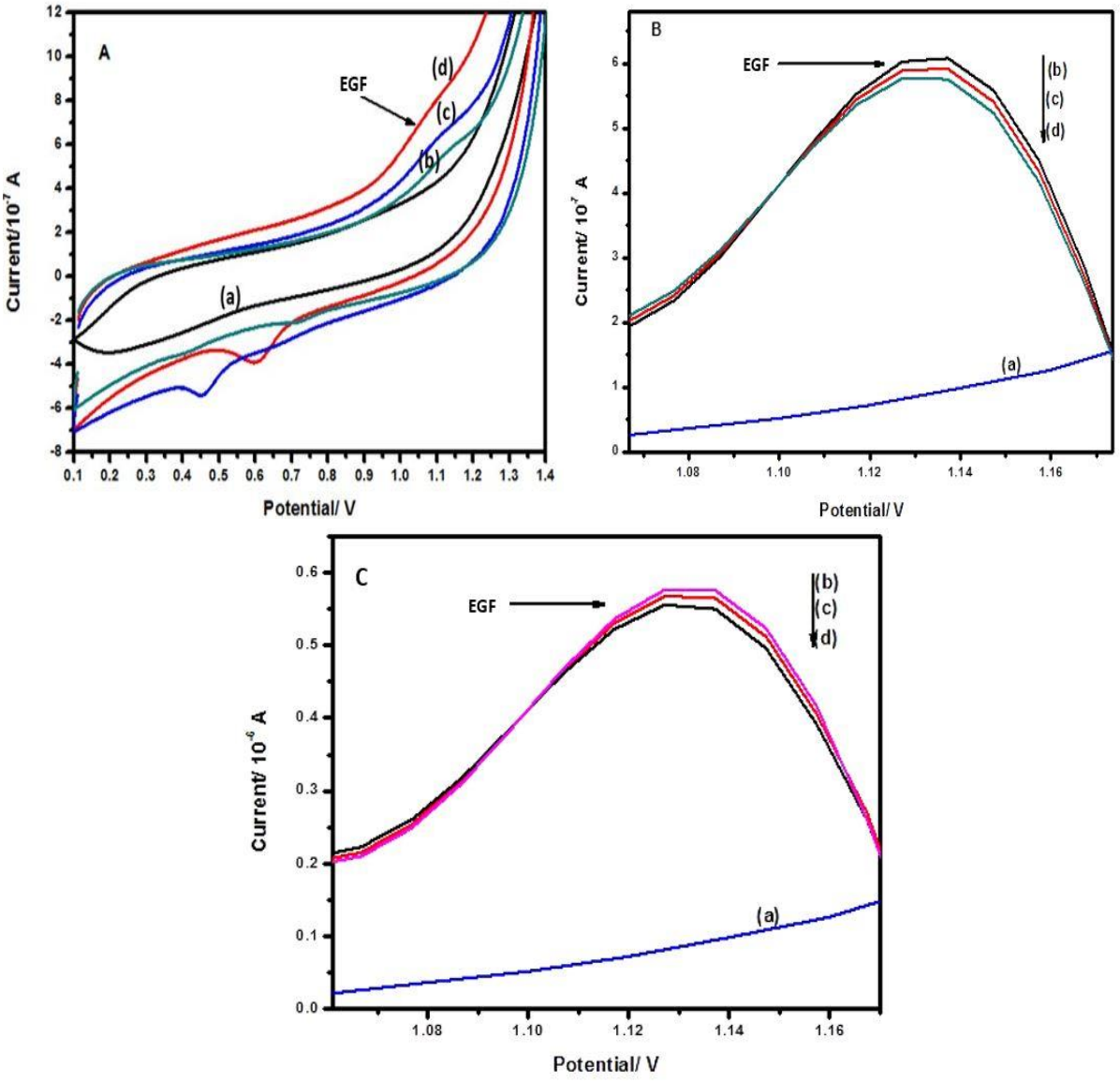

Figure 5.1: Showing electrochemical responses of the modified electrode for (a) blank, (b) 0.7 µM, (c) 0.6 µM and (d) 0.5 µM EGF using (A) CV, (B) DPV, and (C) SWV techniques for the detection of EGF

The DPV technique showed more stability and reliability. Furthermore, the DPV technique exhibits greater sensitivity by removing the non-faradaic currents that are seen in CV. As a result, it was the method of choice for EGF detection.

5.3.1.2 Effect of pulse amplitude, step potential, interval time and starting potential

The impact of varying the DPV parameters on the current intensity was determined. The pulse amplitude, step potential and sweep potential were varied from 10-100 mV, 10-50 mV and 0.2-0.7 V respectively.

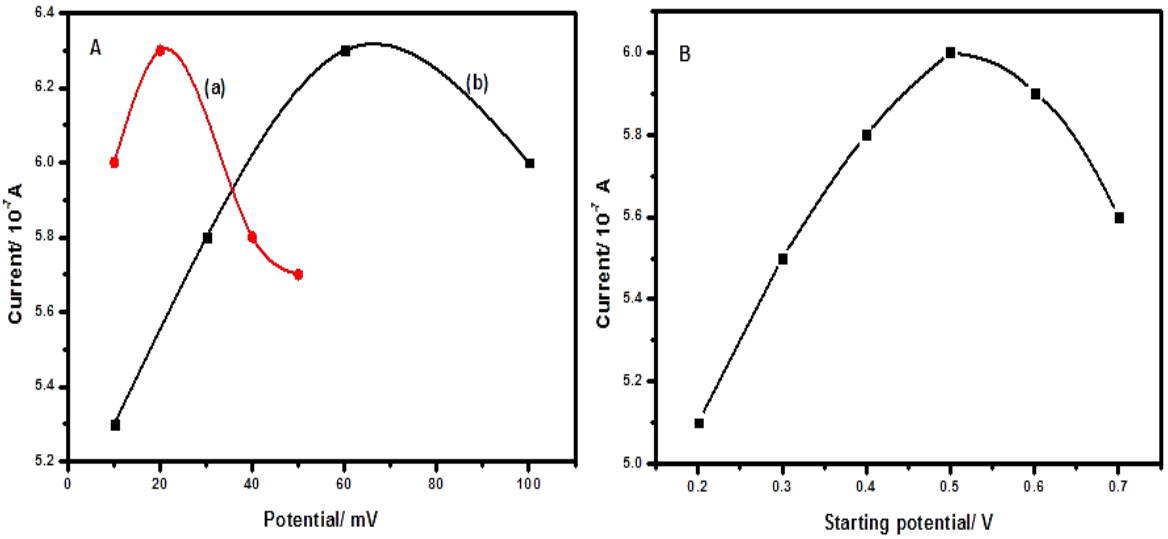

Figure 5.2: (A) Optimisation parameters for (a) step potential, (b) pulse amplitude and (B) starting potential on DPV response

The suitable ranges were chosen based on peak resolution, intensity and stability. The values which yielded the optimum response for pulse amplitude and step potential were 60 mV and 20 mV as shown in Figure 5.2. To obtain maximum peak current with signals which are well resolved, a starting potential of 0.5 V was chosen.

5.3.2 Calibration studies of EGF

EGF standard was diluted to make various concentrations (2-100 nM) and used as a target analyte in 0.1 M PBS solution. Differential pulse voltammetry measurements were carried out at room temperature in the potential range of 500 and 1200 mV. The voltammograms representing the oxidation current versus concentration of EGF are shown in Figure 5.3. The increase in EGF concentration was accompanied by an increase in the peak current. This was evident that the response in current was because of EGF detection by the biosensor. A linear relationship of Ipa versus EGF concentration was established between the oxidation peak current and EGF concentration in the range of 2 nM to 100 nM (inset: Fig 5.3B). The linear regression equation was Y (cm^2) = 0.0331X + 0.126, with a linear correlation coefficient (R^2) of 0.998.

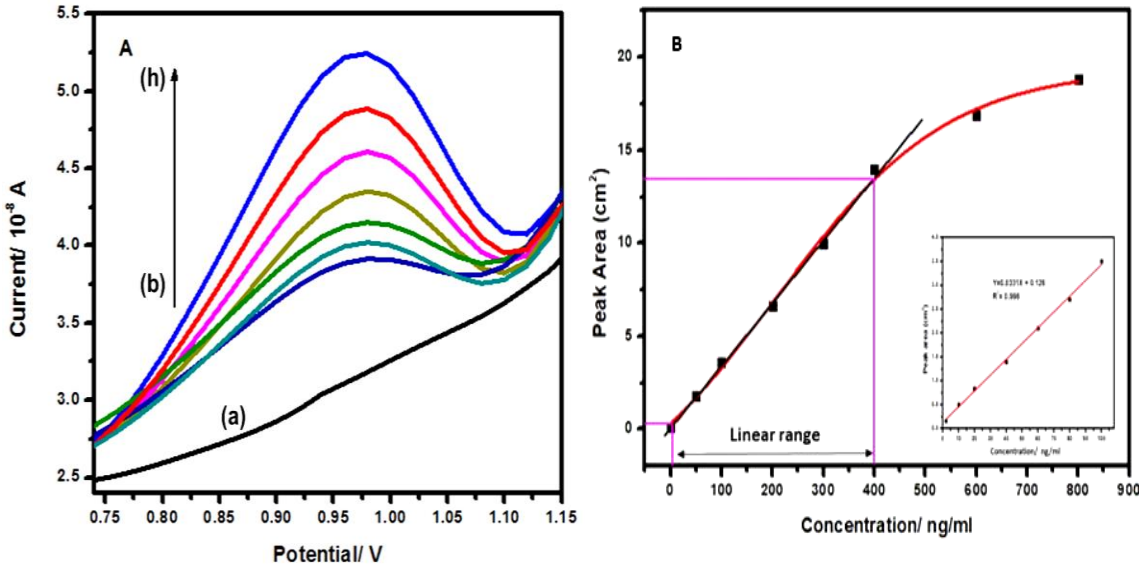

Figure 5.3: (A) The DPV responses of (a) blank, (b) 2 nM, (c) 10 nM, (d) 20 nM, (e) 40 nM, (f) 60 nM, (g) 80 nM and (h) 100 nM EGF concentrations, (B) plot of linear range and inset: calibration plot of EGF

These measurements produced optimum response with high sensitivity and good linearity. The linear range was obtained according to the graph in Figure 5.3B. Under the optimum conditions for EGF concentration range, the limit of detection (LOD) and limit of quantification (LOQ) values were calculated using the equation of LOD = 3σ/m, LOQ = 10σ/ m, where σ is the error of the y intercept and m is the slope of the calibration plot. According to the results from this study, the biosensor gave a low LOD and LOQ as shown in Table 5.2.

Table 5.2: Characteristics of EGF calibration plot using DPV

Parameters	EGF
Regression coefficient (n=7)	0.998
Limit of detection (LOD) (nM)	0.58
Limit of quantification (LOQ) (nM)	1.93
Linear range (nM)	0.5 – 400
Peak potential (mV) vs. Ag/AgCl	975 ± 10

Table 5.3 compares the electrochemical performance of the developed modified electrode in the present study with other electrochemical techniques for the determination of EGF.

Table 5.3: Comparison of major characteristics of various electrochemical methods for the determination of EGF

Method	Sensor	Linear range (pm)	LOD (pm)	References
CV	Ag/PDA/GSSG/Ab/EGF	0.1 - $1x10^4$	0.01	(Lin et al., 2015)
CV	Ag/PDA/BSA/Ab/EGF	1000 to 5 x 10^6	100	(Lin et al., 2015)
DPV	CTAB/Au/ZIF-8/GA/Ab/EGF	500 – 4 x 10^5	580	This work

By comparison, the developed sensor in this study gave a higher linear range than (Lin et al., 2015) using glutathione disulphide (GSSG), lower LOD relative to some of the previous studies mentioned in literature. These results illustrate that the proposed biosensor has improved sensitivity and linearity in the detection of EGF even at a very low concentration. Such a good performance can be attributed to the ZIF-8 matrix providing high antibody loading while not forming steric hindrances to EGF. In people with normal kidney function, concentrations of EGF in urine range from 60 – 80 nM and this decreases when kidney function is impaired.

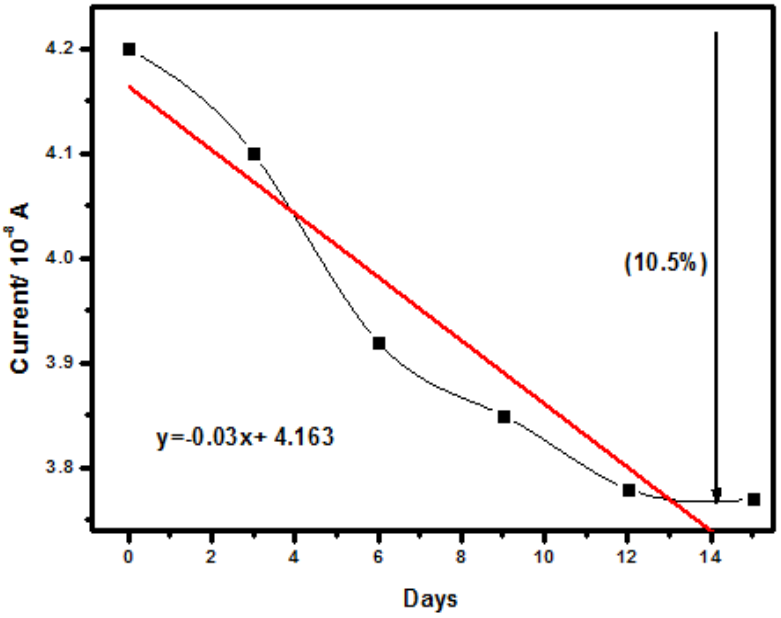

Figure 5.4: Stability studies of biosensor over 15 days

5.3.3 Reproducibility, repeatability and stability studies

In this study, the relative standard deviation (RSD) value of the peak currents of the modified electrode response to 40 nM EGF for six successive measurements on the same electrode was 2.3 %. For repeatability, the RSD was found to be 1.39 %. This indicated acceptable

reproducibility and repeatability values exhibited by the biosensor. The stability of the biosensor was tested over a period of 15 days as shown in Figure 5.4. The oxidation current response to EGF was maintained at 89.5 % after 15 days. This showed that the developed biosensor was relatively stable with a very low gradient.

5.3.4 Interference

Figure 5.5 shows the response of the matrix interferences. Glucose was chosen as an interfering molecule because those who suffer from diabetes excrete a large amount of glucose found in urine and saliva. Creatine was also chosen because those patients with creatine transporter disorder have elevated levels of creatine in urine and saliva. The results showed that the current response of EGF was unaffected even in the presence of 5-fold concentration of glucose and creatine. The % interference calculated in Table 5.4 showed that there was an insignificant effect on the current response of EGF detection. The % interference ranged between 0.4 and 3.6 % with RSD ranges between 2-4 %.

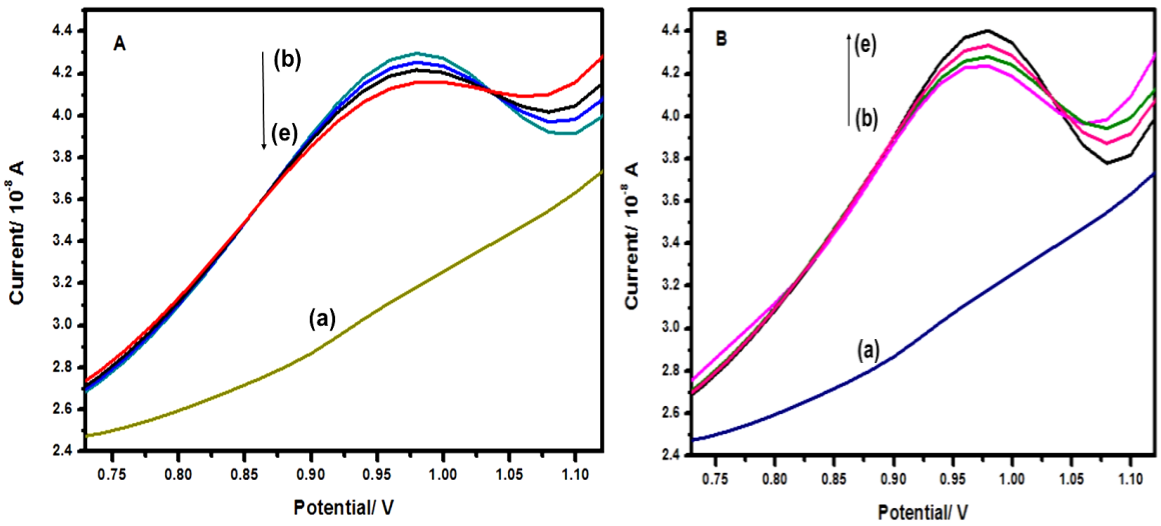

Figure 5.5: The DPV responses for (A) EGF:Creatine showing (a) blank, (b) EGF alone, (c) 1:1, (d) 5:1 and (e) 1:5, (B) EGF:Glucose showing (a) blank, (b) EGF alone, (c) 1:1, (d) 1:5 and (e) 5:1

The increasing peak current order observed above does not show any proportionality or trend with respect to the increase in interfering compound concentration. Additionally, the % interference was below the highest acceptable value (5%). RSD ranges between 1 and 3 %.

Table 5.4: Effect of possible interfering compounds on EGF detection, percent interference is in brackets

Interfering Compound	Mole ratio of EGF: possible Interfering compound				
	EGF Alone (nA)	1:1	1:5	5:1	RSD (n=3)
Glucose	42.3	42.1(0.48)	41.8(1.18)	41.3(2. 60)	2.58
Creatine	42.0	42.3(0.71)	43.5(3.57)	42.8(1.90)	3.87

5.3.5 Real samples

To evaluate the accuracy of the developed procedure, the modified electrode was evaluated in human urine and saliva of a male. The samples were taken from a volunteer with no previous record of kidney disease. The concentration of EGF in males with a normal kidney function ranges from 60 – 70 ng/ml and it gets lower when kidney function is impaired. In saliva, the EGF concentration for a male with normal kidney function ranges between 2 – 3.5 ng/ml. Figure 5.6 shows the results of the modified electrode in urine and saliva. The peak areas were determined and the concentration of EGF in urine and saliva was calculated using the equation of the calibration plot, Y (cm^2) = 0.0331X + 0.126.

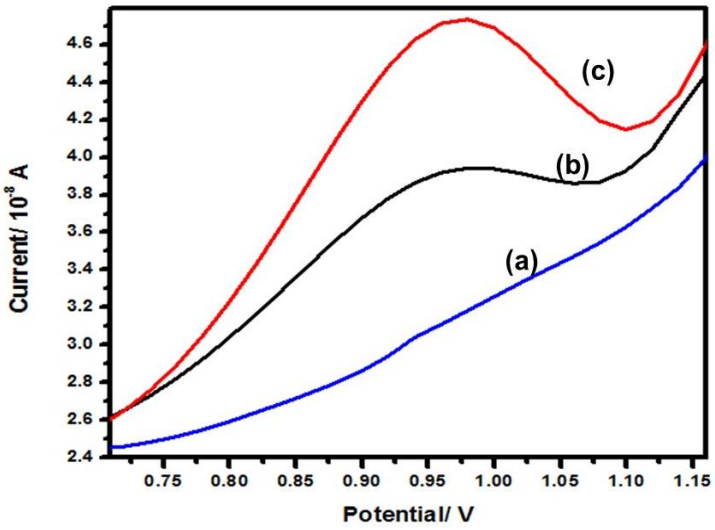

Figure 5.6: The DPV responses of (a) blank, (b) saliva and (c) urine on CTABAu/ZIF-8/GA/Ab modified electrode

The obtained results showed an EGF concentration in urine and saliva of 67.5 ng/ml and 3.12 ng/ml respectively as shown in Table 5.5. The results were within the physiological levels of EGF concentration in males with normal kidney function as compared with literature

values. This showed the applicability of the developed biosensor for measurement and monitoring of EGF.

Table 5.5: Results of the obtained concentration of urine and saliva samples

Sample	Obtained concentration (nM)	Physiological concentration range (nM)	Reference
Urine	67.5	60-80	(Chou et al., 1997)
Saliva	3.12	2-3.3	(Joh et al., 1986)

5.3.6 Validation

The biosensor functionality was analysed through spiking and recoveries of the EGF in urine and milk. The samples were spiked with 10 ng/ml and 2 ng/ml for diluted urine and saliva respectively and differential pulse voltammograms were recorded. The amount of EGF in urine and milk samples was calculated from the calibration plot and the results of the analysis are summarized in Table 5.6. Equation 5.3 shows how the expected concentration from the spiked samples was calculated:

$$Cexp = \frac{(Sample\ \ concentration\ \ \ after\ \ dilution\ \ x\ sample\ \ vol)+(Spike\ concentration\ \ \ x\ spike\ \ vol)}{Volume\ \ of\ \ spike\ +Volume\ \ of\ \ diluted\ \ \ sample}$$

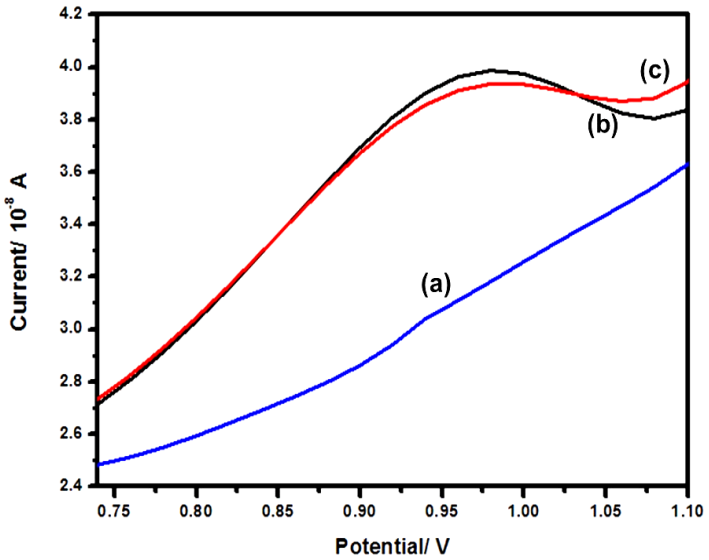

Figure 5.7: The DPV responses for spiking and recoveries for (a) blank, (b) urine and (c) saliva

The percentage recovery of EGF was determined by comparing the corresponding concentration of EGF from the peak area obtained in Figure 5.7 with the expected concentration due to the spiking concentration. The recovered amounts range from 112 to 115 % with acceptable RSD between 2 to 3,5 %. This validates the applicability of the developed biosensor.

Table 5.6: Results of analysis of EGF in spiked human urine and milk samples (n = 3)

Diluted samples	Spike (nM)	Final volume (ml)	Expected (nM)	Determined (nM)	% Recovery	% RSD
Urine	10 nM	1.05	6.90	7.75	112.18±4	3.17
Saliva	2 nM	1.05	2.06	2.34	113.42±3	2.28

5.4 Conclusion

An electrochemical biosensor based on the immobilization of Ab on a metal organic framework embedded with gold nanorods for the detection of EGF was developed. The development procedure exhibited an excellent biocompatibility with the aid of glutaraldehyde acting as a cross linker, ZIF-8 acting as an immobilization platform for the antibody and Au NRs accelerating and amplifying signal transduction. The DPV, CV and SQW techniques were applied for the detection for EGF. Results showed increased current and better resolution using DPV. Optimisation of the DPV parameters showed values for starting potential, pulse amplitude and step potential of 0.5 V, 60 mV and 20 mV respectively. The biosensor linearity towards EGF was in the concentration range from 2-100 nM with a LOD of 0.58 nM. Reproducibility and repeatability tests were acceptable with a RSD of 2.3 % and 1.4 % respectively. The biosensor showed acceptable stability over 15 days with the oxidation current response to EGF maintained at 89.5 %. There was no interference observed in the presence of glucose and creatine. The EGF biosensor showed concentrations of 67.5 and 3.12 nM in urine and saliva respectively. These results indicate that the proposed biosensor can offer vast analytical applications and has potential to be used as a clinical diagnostic.

.

5.5 References

Baars, J. 1994. Application of the Dropping Mercury Microelectrode in Electrode Kinetics, *Journal of Electroanalytical Chemistry*., 364 (1994), 189.

Bard, J., Faulkner, I. 1980. Electrochemical Methods. New York: Wiley.

Beiginejad, H., Nematollahi, D., Farmaghani, F. 2013. Electrochemical oxidation of some aminophenols in various pHs, *J. Electrochem. Soc*., 160, 41-46.

Bersier, B. M. 1987. Do Polarography and Voltammetry Deserve Wider Recognition in Official and Recommended Methods?, *Analytical Proceedings*., 24: 44.

Brett, C., Bret, M. 1993. Electrochemistry: Principles, Methods and Applications. Oxford: Oxford University Press.

Chou, J. S., Reiser, I. W., Porush, J. C. 1997. Aging and urinary excretion of epidermal growth factor. *Annals of Clinical and Laboratory Science* 27(2): 116-122.

Faolcaro, P. 2014. MOF positioning technology and device fabrication. *Chem. Soc. Rev,* 43 (16): 5403-6176.

Joh, T., Itoh, M., Katsumi, K., Yokoyama, Y., Takeuchi, T., Kato, T., Wada, Y. & Tanaka, R. 1986. Physiological concentrations of human epidermal growth factor in biological fluids: use of a sensitive enzyme immunoassay. *Clinica chimica acta; international journal of clinical chemistry*, 158(1): 81–90.

Kissinger, P. T., Heineman, W. R. 1983. Cyclic Voltammetry, J. Chem. Educ., 60, 702-706.

Kounaves, P. 1987. Square Wave Anodic Stripping Voltammetry at the Mercury Film Electrode: Theoretical Treatment*, Analytical Chemistry*, 59: 386.

Lee, K, W., Hwang, K, H., Kim, C, S., Han, K., Chung, Y,B., Park, J, S., Lee, Y, M., Moon, D, C. 2001. Determination of Recombinant human epidermal growth factor (rhEGF) in a pharmaceutical formulation by high performance liquid chromatography with electrochemical detection. *Archives of Pharmacal Research*, 24:355–9.

Lim, H.S, Barclay, D.J., Anson, F.C. 1972. Formal potentials and cyclic voltammetry of some ruthenium-ammine complexes, *Inorg. Chem*.,11, 1460-1466.

Long, S., Silvester, D. S., Barnes, A. S., Rees, N. V., Aldous, L., Hardacre, C., Compton, R. G. 2008. Oxidation of several pphenylenediamines in room temperature ionic liquids: estimation of transport and electrode kinetic parameters, *J. Phys. Chem. C*., 112, 6993-7000.

Mabbott, G. A. 1983. An Introduction to Cyclic Voltammetry, *J. Chem. Educ*., 60, 607-702.

Moressi, M. B., Zon, M. A., Fernandez, H. 1994. The determination of thermodynamic and heterogeneous kinetic parameters of the TMPD/TMPD•+ redox couple in tetrahydrofuran and n-butanol using ultramicroelectrodes. Quasi steady-state voltammetry, *J. Braz. Chem. Soc*., 5, 167-72.

O'dea, J., Osteryoung, J. 1981. Theory of Square Wave Voltammetry for Kinetic Systems, *Analytical Chemistry.*, 53: 695.

Osteryoung, J. 1985. Square Wave Voltammetry, *Analytical Chemistry*, 57: 101.

Rock, P.A. 1966. The Standard Oxidation Potential of the FerrocyanideFerricyanide Electrode at 25°C and the Entropy of Ferrocyanide Ion, *J. Phys. Chem*., 70, 576-580.

Rudolph, J. 1994. A Simulator for Cyclic Voltammetric Response, *Analytical Chemistry.*, 66: 589.

Van Benschoten, J. J., Lewis, Y. T., Heineman, W. R., Roston, D. A., Kissinger, P. T. 1983. Cyclic Voltammetry Experiments, J. Chem. Educ., 60, 772-776.

Vazquez, J., Freyre, M. 1990. Radio and enzyme immunoassays with monoclonal antibody. *Biotechnolgy,* 7 (1): 42-51.

CHAPTER SIX

CONCLUSION AND RECOMMENDATION

6.1 Conclusion

Gold nanorods and ZIF-8 were synthesised using the seed mediated and hydrothermal method respectively. Gold nanorods composites of cysteine, ZIF-8 and both were also successfully synthesised. The optimum conditions for thiol-gold interactions were evaluated by looking at various parameters. The parameters included the effect of reaction time, volume ratio, concentration ratio, pH and temperature of which optimum conditions of 1 hr, 1:1, 1.0^{8}:1 for Au:Cys, pH of 6 and 25 °C were obtained respectively. The presence of CTAB in gold nanorods was also found to be beneficial to facilitate bonding with cysteine. The nanomaterials and composites synthesised were characterized using spectroscopic and electrochemical techniques. Results from UV-Vis spectra showed the formation of two plasmon bands for gold nanorods, one transverse and the other longitudinal. After functionalisation with cysteine, a new peak appeared at higher wavelengths which was attributed to the formation of a new gold-cysteine complex which was also confirmed in the cyclic voltammetry results. In FTIR studies, the Zn-N stretching mode typical for ZIF-8 was seen at 424 cm^{-1} which was consistent with other literature values. The data from SEM analysis confirmed the morphology, with gold showing the nanorods structure and ZIF-8 the rhombic dodecahedral structure. The XRD patterns showed peaks consistent with gold nanorods at 2θ = 37.5°, 44.6°, 64.7° representing the (111), (200), (220) crystal planes respectively and that for ZIF-8 at 6.7°, 10.9°, 14.2°, 16.5°,20.1°, 24.4°, 27.7°, 31.6° representing the (011), (002), (022), (013), (222), (114), (134), (244) crystal planes respectively. The XRD spectra for gold nanorods functionalised with ZIF-8 showed both characteristic peaks for gold nanorods and ZIF-8 indicating that there was no damage to the structures. That for cysteine functionalised gold nanorods showed similar patterns for gold nanorods with lower intensity showing variations in crystallinity. Various platforms comprising of GCE/CTABAu, GCE/CTABAu/Cys, GCE/CTABAu/ZIF-8 and GCE/CTABAu/ZIF-8/Cys were characterised using cyclic voltammetry. All the platforms showed typical characteristic peaks for Au NRs except for cysteine containing composites which had an additional cathodic peak. The results from the electrochemical parameters studied showed that functionalised Au NRs had a lower peak separation owing to better conductivity. Electrochemical band gaps were also studied to analyse conductivity of the platforms, they were in the order CTABAu/Cys > CTABAu/ZIF-8/Cys > CTABAu > CTABAu/ZIF-8. For fabricating the transducer, the nature of the kinetic parameters of the platforms were

determined using Laviron's equation and both diffusion and adsorption controlled processes were observed. On CTABAu/ZIF-8 and CTABAu/ZIF-8/Cys platforms, higher ks value were obtained indicating that functionalized gold nanorods provide faster electron transfer at the surface of the electrode. Both cysteine and ZIF-8 containing platforms were analysed in biosensor applications and ZIF-8 showed a better response with the EGF analyte so the CTABAu/ZIF-8 platform was chosen as the transducer. Optimisation of biosensor fabrication was undertaken by assessing the various components and techniques used in biosensor development. The results showed that glutaraldehyde was crucial as a cross linker and ZIF-8 played a significant role in keeping the antibody immobilized on the framework. The attachment method for the various components was analysed using the drop coating and immersion method. The immersion method gave a better response and it was the method of choice. Various concentrations of gold nanorods were analysed against a constant ZIF-8 concentration and the optimum response was at a Au NR concentration of 1 nM. Optimum conditions were found to be immersion in 3 % GA and 2 µg/ml Ab, with incubation times of 8, 10 and 5 minutes for GA, Ab and EGF respectively at a pH of 6. The biosensors response to EGF was tested using various electroanalytical techniques (differential pulse voltammetry, square wave voltammetry and cyclic voltammetry. Differential pulse voltammetry gave a better reproducibility and higher current therefore it was the technique used for EGF detection. The instrument parameters were optimised and a good response for pulse amplitude, step potential and starting potential were found at 60 mV, 20 mV and 0.5 V respectively. The sensor exhibited strong electroactivity towards the oxidation of EGF at 0.9 V. The biosensor analytical parameters were linear towards EGF in the concentration range from 2 to 100 nM with a detection limit of 0.58 nM. The detection limit was lower than some obtained using other techniques. Repeatability and reproducibility tests showed positive results and the biosensor maintained 89.5 % stability within 15 days. Matrix interference studies showed no interference with glucose and creatine. The EGF biosensor was successfully applied in urine and saliva analysis, obtaining EGF concentrations of 67.5 and 3.12 nM respectively. This work opens a novel approach in the use of EGF as a biomarker for kidney disease.

6.2 Future work and recommendations

To fully realize the potential applications and new opportunities of MOF composites, further fundamental research is required. For example, a precise understanding of how proteins and living cells induce the growth of MOFs and affect their structure and morphology is essential. Such knowledge will facilitate the development of general protocols for encapsulation of

biomacromolecules and for crystallizing MOFs on tissues and living organisms and will underpin exploration of biomedical applications. Also, fabrication of the transducer and immunosensor can be characterized using other techniques which were not available during the analysis.